



**NAVAL
POSTGRADUATE
SCHOOL**

MONTEREY, CALIFORNIA

DISSERTATION

LASER ACCELERATOR

by

Ricardo Vigil

September 2014

Dissertation Supervisor:

William B. Colson

Approved for public release; distribution is unlimited

THIS PAGE INTENTIONALLY LEFT BLANK

REPORT DOCUMENTATION PAGE

Form Approved OMB No. 0704-0188

Public reporting burden for this collection of information is estimated to average 1 hour per response, including the time for reviewing instruction, searching existing data sources, gathering and maintaining the data needed, and completing and reviewing the collection of information. Send comments regarding this burden estimate or any other aspect of this collection of information, including suggestions for reducing this burden to Washington headquarters Services, Directorate for Information Operations and Reports, 1215 Jefferson Davis Highway, Suite 1204, Arlington, VA 22202-4302, and to the Office of Management and Budget, Paperwork Reduction Project (0704-0188) Washington DC 20503.

1. AGENCY USE ONLY (Leave Blank)	2. REPORT DATE 09-26-2014	3. REPORT TYPE AND DATES COVERED Dissertation 12-01-2012 to 09-26-2014	
4. TITLE AND SUBTITLE LASER ACCELERATOR		5. FUNDING NUMBERS	
6. AUTHOR(S) Ricardo Vigil			
7. PERFORMING ORGANIZATION NAME(S) AND ADDRESS(ES) Naval Postgraduate School Monterey, CA 93943		8. PERFORMING ORGANIZATION REPORT NUMBER	
9. SPONSORING / MONITORING AGENCY NAME(S) AND ADDRESS(ES) N/A		10. SPONSORING / MONITORING AGENCY REPORT NUMBER	
11. SUPPLEMENTARY NOTES The views expressed in this document are those of the author and do not reflect the official policy or position of the Department of Defense or the U.S. Government. IRB Protocol Number: N/A.			
12a. DISTRIBUTION / AVAILABILITY STATEMENT Approved for public release; distribution is unlimited		12b. DISTRIBUTION CODE	
13. ABSTRACT (maximum 200 words) In 1979, W. B. Colson and S. K. Ride proposed a new kind of electron accelerator using a uniform magnetic field in combination with a circularly-polarized laser field. A key concept is to couple the oscillating electric field to the electron's motion so that acceleration is sustained. This dissertation investigates the performance of the proposed laser accelerator using modern high powered lasers and magnetic fields that are significantly improved over the values in the original analysis. The relativistic equations of motion for the electron are solved analytically and for the first time numerically for more general results than previously reported. Realistic beam effects are investigated to determine the constraints on initial electron energy, injection angle, and phase to achieve optimal performance. This analysis indicates that the selection of an electron's initial conditions are not as stringent as previously thought. Simulations indicate a university scale system can achieve electron energy gain of over one GeV in a meter.			
14. SUBJECT TERMS laser, accelerator, doppler-shifted light, autoresonance, resonance, magnetic field, Lorentz force law, relativistic cyclotron frequency, laser gain		15. NUMBER OF PAGES 123	
		16. PRICE CODE	
17. SECURITY CLASSIFICATION OF REPORT Unclassified	18. SECURITY CLASSIFICATION OF THIS PAGE Unclassified	19. SECURITY CLASSIFICATION OF ABSTRACT Unclassified	20. LIMITATION OF ABSTRACT UU

NSN 7540-01-280-5500

Standard Form 298 (Rev. 2-89)
Prescribed by ANSI Std. Z39-18

THIS PAGE INTENTIONALLY LEFT BLANK

Approved for public release; distribution is unlimited

LASER ACCELERATOR

Ricardo Vigil
Commander, United States Navy
B.S., Rensselaer Polytechnic Institute, 1996
M.S., Naval Postgraduate School, 2006

Submitted in partial fulfillment of the
requirements for the degree of

DOCTOR OF PHILOSOPHY IN APPLIED PHYSICS

from the

NAVAL POSTGRADUATE SCHOOL
September 2014

Author: Ricardo Vigil

Approved by: William B. Colson Joe Blau
Professor of Physics Professor of Physics
Dissertation Supervisor

Keith Cohn Gamani Karunasiri
Professor of Physics Professor of Physics

James Luscombe James Newman
Professor of Physics Professor of Space Systems

Approved by: Andres Larraza
Chair, Department of Physics

Approved by: Douglas Moses
Vice Provost for Academic Affairs

THIS PAGE INTENTIONALLY LEFT BLANK

ABSTRACT

In 1979, W. B. Colson and S. K. Ride proposed a new kind of electron accelerator using a uniform magnetic field in combination with a circularly-polarized laser field. A key concept is to couple the oscillating electric field to the electron's motion so that acceleration is sustained. This dissertation investigates the performance of the proposed laser accelerator using modern high powered lasers and magnetic fields that are significantly improved over the values in the original analysis. The relativistic equations of motion for the electron are solved analytically and for the first time numerically for more general results than previously reported. Realistic beam effects are investigated to determine the constraints on initial electron energy, injection angle, and phase to achieve optimal performance. This analysis indicates that the selection of an electron's initial conditions are not as stringent as previously thought. Simulations indicate a university scale system can achieve electron energy gain of over one GeV in a meter.

THIS PAGE INTENTIONALLY LEFT BLANK

Table of Contents

1	Background	1
1.1	Motivation and Research Questions	1
1.2	History of Particle Accelerators	2
2	Laser Accelerator	9
2.1	Laser Accelerator System Overview	9
2.2	Laser Source	9
2.3	Electron Injector	14
2.4	External Magnetic Field	18
3	Equations of Motion	23
3.1	Relativistic Lorentz Force	23
3.2	Equations of Motion	25
3.3	Integral Representation	31
3.4	Curtate Cycloids	33
3.5	Resonance Condition.	37
3.6	Electron Phase	38
3.7	Maximum Energy Gain	39
4	Numerical Methodology	41
4.1	Finite-difference Method	41
4.2	Initial Conditions on Resonance ($\Delta\omega = 0$)	42
4.3	Electron Trajectory	44
4.4	Synchrotron Radiation	45
4.5	Numerical Integration	47
5	Numerical Analysis Results	49
5.1	On-resonance with $\theta_o = \pi$	49
5.2	Electron Phase Performance	53

5.3	Off-resonance Performance	60
5.4	Magnetic Field Effects	66
5.5	Diffraction Effects	67
6	Conclusions	73
Appendix: Simulation Codes		75
A.1	Laser Accelerator Simulation Core	75
A.2	Laser Accelerator Matlab Graphics Script	92
List of References		99
Initial Distribution List		103

List of Figures

Figure 1.1	Cockcroft-Walton Cascade Generator	3
Figure 1.2	Van de Graaff Accelerator	4
Figure 1.3	Linear Accelerator	5
Figure 1.4	Cyclotron Accelerator	6
Figure 1.5	Livingston Chart	7
Figure 2.1	Chirped Gaussian Pulse	11
Figure 2.2	Diagram Illustrating Chirped Pulse Amplification	12
Figure 2.3	Texas Petawatt Laser System Layout	14
Figure 2.4	Cross-section of a Triple Spoke Cavity	16
Figure 2.5	Naval Postgraduate School SCRF Gun	17
Figure 2.6	Cutaway Diagram of Hybrid Magnet at the National High Magnetic Field Laboratory	19
Figure 2.7	Cutaway Diagram of a Pulsed Magnet System at the National High Magnetic Field Laboratory	21
Figure 3.1	Schematic of Laser Accelerator	27
Figure 3.2	Standard, Curtate, and Prolate Cyloids	34
Figure 3.3	Diagram of Initial Electron Distribution in the Longitudinal Direction	38
Figure 4.1	Injection Angle Required for Resonance	43
Figure 4.2	Allowed Values of Injection Angles	44
Figure 5.1	Comparison of Analytic Solution to Numerical Simulation Results of an Electron in the Laser Accelerator	50

Figure 5.2	Numerical Simulation Results For Two Different Electrons in the Laser Accelerator for 45 T and 100 T External Magnetic Fields	51
Figure 5.3	Electron Trajectories in the Laser Accelerator for Two Different External Magnetic Field Cases	53
Figure 5.4	Numerical Simulation of Laser Accelerator for Various Initial θ_o and $\gamma_o = 130$	55
Figure 5.5	Numerical Simulation of Laser Accelerator for Various Initial θ_o and $\gamma_o = 125$	56
Figure 5.6	Numerical Simulation of Laser Accelerator for Various Initial θ_o and $\gamma_o = 120$	57
Figure 5.7	Numerical Simulation of Laser Accelerator for Various Initial θ_o and $\gamma_o = 119$	58
Figure 5.8	Numerical Simulation of Laser Accelerator for Minimum Energy Injection for Resonance	59
Figure 5.9	Numerical Simulation of Laser Accelerator Over All θ_o and Small Range of Injection Angles	61
Figure 5.10	Numerical Simulation of Laser Accelerator Over All θ_o and Small Range of Injection Angles	62
Figure 5.11	Numerical Simulation of Laser Accelerator Over All θ_o and Small Range of Injection Angles	63
Figure 5.12	Numerical Simulation of Laser Accelerator Over All θ_o and Small Range of Injection Angles	64
Figure 5.13	Numerical Simulation of Laser Accelerator Over B_u and Initial Energy γ_o	65
Figure 5.14	Magnetic Field Variation Along z with Maximum Field at $z_w = 0.5$ m	67
Figure 5.15	Magnetic Field Variation Diagram Defines θ_1 and θ_2 for Calculating the Magnetic Field Along the Longitudinal Axis of a Solenoid	67
Figure 5.16	Numerical Simulation Results of a Single Electron in the Laser Accelerator System with Magnetic Field Variation	68

THIS PAGE INTENTIONALLY LEFT BLANK

List of Tables

Table 2.1	Petawatt Laser System Specifications, after [2]	10
Table 2.2	Available Magnets at the National High Magnetic Field Laboratory, after [18]	18
Table 2.3	Available Pulsed Magnets at PFF LANL. SP = Short Pulse. MP = Mid-Pulse, after [19]	20
Table 2.4	Magnet Specification Summary, after [19].	20
Table 3.1	Equations and Constants of the Motion	31
Table 5.1	Input Parameters for Resonance Laser Accelerator Simulation . .	50
Table 5.2	Results for Single Electron Simulation of Laser Accelerator at 45 T and 100 T	53

THIS PAGE INTENTIONALLY LEFT BLANK

List of Acronyms and Abbreviations

- α injection angle
A ampere
a third constant of the motion
b fourth constant of the motion
B_u external magnetic field strength
 β electron velocity relative to the speed of light
 β_x x component of electron velocity relative to the speed of light
 β_y y component of electron velocity relative to the speed of light
 β_z z component of electron velocity relative to the speed of light
 β_{\perp} perpendicular component of electron velocity relative to the speed of light
c speed of light
CPA chirped pulse amplification
C coulomb
DC direct current
 ε normalized emittance
 ε first constant of the motion
 E_r laser electric field amplitude
 k_e electron wavenumber
 k_r laser radiation wavenumber
 E_o electric field amplitude
eV electron volt
fs femtosecond
 a_p Gaussian pulse length
Hz Hertz
 ω_i instantaneous angular frequency
J joule
K Kelvin
kA kiloampere
keV kilo-electronvolt
 λ_r laser wavelength

b_p linear chirp parameter
 γ Lorentz factor
m meter
NHMFL National High Magnetic Field Laboratory
 η second constant of the motion
Nd neodymium
NCRF normal conducting radio-frequency
OPCPA optical parametric chirped pulse amplification
 p^μ momentum four-vector
 ϕ azimuthal angle between x -axis and β_\perp
PW petawatt
R radius of curvature of wavefronts
 θ angle between perpendicular velocity and laser electric field vector
TPL Texas Petawatt Laser
w optical mode waist
 $\Delta\omega$ resonance parameter
 ω_c relativistic cyclotron frequency
 ω_E electric field analogue to relativistic cyclotron frequency
 ω_o central Gaussian wavelength
 ω_p pump laser angular frequency
 ω_s signal laser angular frequency
 ω_{rs} residual signal angular frequency
 ω_r laser radiation angular frequency
 ζ electron phase
 Z_r Rayleigh range

Acknowledgments

I would like to express my deepest and utmost gratitude to my advisor, Prof. Bill Colson. I am grateful for his mentorship, patience, and friendship over the past ten years. I look forward to continued collaboration and discussion in my next tour of duty and beyond.

I would like to thank Prof. Cohn and Prof. Blau for their guidance especially in helping me reduce my long-winded sentences to something clear and concise. I would like to thank Prof. Newman, Prof. Karunasiri, and Prof. Luscombe for their support. I will miss Prof. Luscombe's classroom discussions the Grateful Dead, Monty Python, and random movie quotes.

I would also like to thank Prof. Giraldo, Prof. Frenzen, and my cousin Prof. Dan Gefroh for their valuable discussions about this dissertation.

THIS PAGE INTENTIONALLY LEFT BLANK

CHAPTER 1:

Background

In 1979, W. B. Colson and S. K. Ride [1] proposed a new kind of accelerator using a uniform, magnetic field in combination with a circularly-polarized laser field. Lasers can have strong electric fields with frequencies high enough to avoid corona formation and breakdown. The key is to couple the electric field to the electron such that it always “sees” a relatively steady field so that acceleration is sustained. Colson and Ride [1] suggested that if the external magnetic field is aligned along the light-propagation axis and the magnetic field strength, laser frequency, and initial electron velocity are selected judiciously, the composite field forces are resonant indefinitely, so that the electron continues to be accelerated over the interaction length. For laboratory magnetic fields of 45 T and a petawatt laser, it will be shown through numerical simulations, electrons could be accelerated from about 100 million-electron-volts to about 1 giga-electron-volts (GeV) in about a meter. This is significantly better than considered in the original research paper [1].

1.1 Motivation and Research Questions

In today’s high powered lasers, electric fields on the order of 10^{11} V/m are possible [2]. Electric fields are transverse to propagation and oscillating at high frequencies on the order of 10^{15} seconds [2], [3]. This high frequency conspires to make the coupling of the electrons to the light difficult. Electromagnetic forces would average to zero due to the rapidly oscillating light field. Using an external uniform, static magnetic field on the order of 45 T, would help provide sustained coupling between the electron and the alternating fields of the laser. This motivates a several questions that this dissertation will attempt to answer.

1. Can modern lasers and magnetic fields provide increased coupling compared to Colson’s and Ride’s original results?
2. What are the engineering considerations for this laser accelerator system?
3. How is success measured?
4. What are the constraints, if any, for optimal performance?

5. How would real beam effects, such as emittance, affect performance?

1.2 History of Particle Accelerators

Particle accelerators have been used since the early 1900s to study the structure of matter. Since then, particle accelerators have also been used in applied research for industrial, medical, and military applications. Particle accelerators are broadly classified into two types: electrostatic or direct current (DC) accelerators and oscillating field or radio-frequency (RF) accelerators.

An important discovery in the development of particle accelerators can be traced back to the work of E. Rutherford [4]. In 1906, Rutherford developed the theory of atomic scattering through his experiments with α -particles and atomic disintegration [4]. His subsequent gold-foil experiments with H. Geiger and E. Marsden put to rest the “plum-pudding” model of the atom in favor of the nucleus model. The Geiger-Marsden experiments proved that unaccelerated α -particles, produced by the spontaneous decay of radium atoms, could be scattered by over 90 degrees when fired at a gold foil. Scattering angles of this magnitude could only occur if a dense nucleus existed at each gold atom site [4].

By 1919, Rutherford believed he required on the order of a few million electron-volt (MeV) α -particles to split the lithium nucleus. This value exceeded the electrostatic accelerator technology at that time so research in this effort stalled [5]. In 1928, G. Gamov predicted, through quantum tunneling effects, that approximately 450 keV α -particles would suffice in splitting the lithium nucleus. Encouraged by Rutherford, Cockcroft and Walton developed a DC accelerator, shown in Fig. 1.1, to achieve this energy requirement. The Cockcroft-Walton accelerator is a type of accelerator whereby static electric fields are used to accelerate charged particles [6]. Their design uses a voltage multiplier comprised of capacitors and diodes to achieve high DC voltage from a low DC or AC voltage source. By 1932, their accelerator reached 400 keV and was able to split the lithium nucleus. They were awarded the Nobel Prize in Physics in 1951 for this work. In DC or electrostatic accelerators, voltages of several MV can be reached today [5].

Another type of electrostatic accelerator is the Van de Graaff generator developed by R. J. Van De Graaff in the early 1930s, see Fig. 1.2. In this design, a moving belt is used to

transfer charge to a hollow metal sphere. Voltages of over 10 MV can be reached if used with an insulating gas. Corona discharge limits all electrostatic accelerators to voltages of several tens of MV due to the formation of ions in the device. The stripped electrons then collide and cause an avalanche of more electrons leading to a spark discharge in the accelerator and thus a breakdown of the electrostatic field [6], [7].

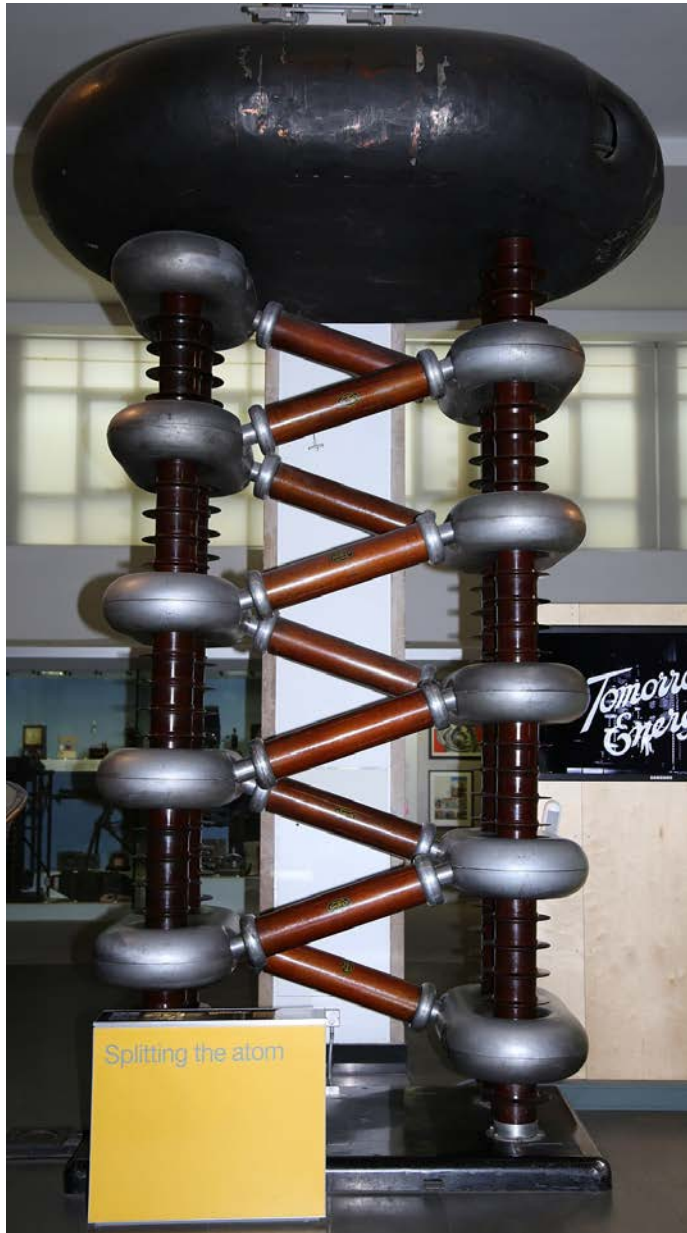


Figure 1.1: Cockcroft-Walton cascade generator used to split lithium atom, from [7].

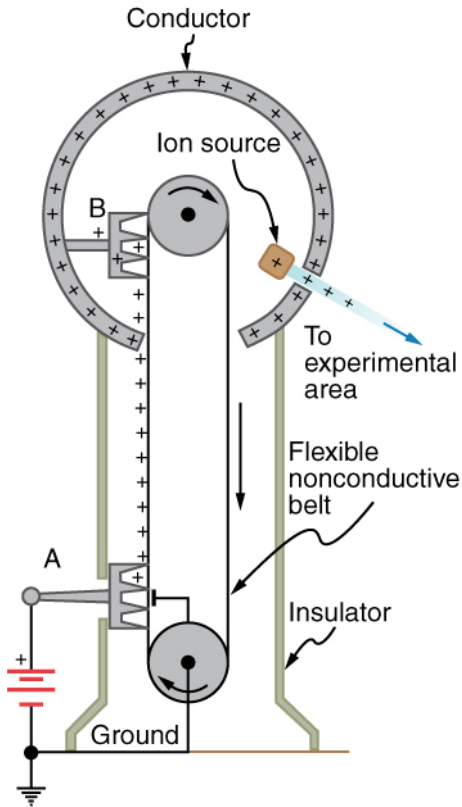


Figure 1.2: Schematic of a Van de Graaff accelerator, from [7].

To overcome corona formation, G. Ising proposed in 1924 the use of radio-frequency (RF) fields [4]. Corona formation is avoided since the alternating voltage seen by molecules is of a high enough frequency that the electromagnetic force time averages to zero. In 1928, R. Wilderöe demonstrated this principle with 50 keV potassium ions [4]. Wilderöe's device is a linear RF accelerator using drift tubes, as shown in Fig. 1.3. The RF source is connected to each drift tube so that an electron only feels the accelerating force of the electric field at each drift tube gap. Then, while the electron is traveling at constant velocity in the drift tube, the fields oscillate such that the electron is again accelerated in the next gap. Drift tubes have been replaced by metal cavities since the mid-1930s and by superconducting RF cavities since the 1960s [4]. Superconducting RF cavities minimize the heat losses in the cavity relative to the energy stored in the resonator achieving a very high Q-factor, and therefore high fields [4].

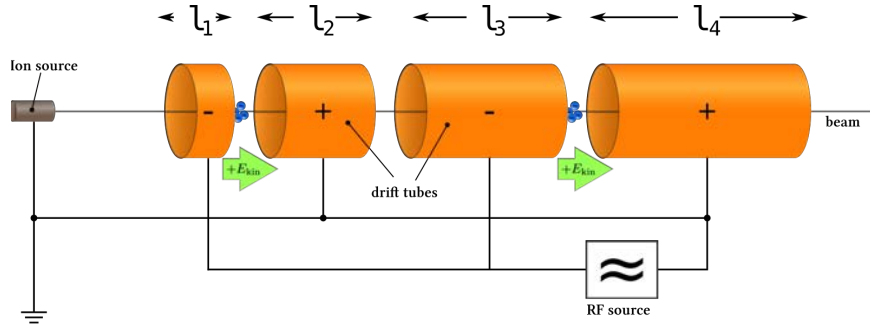


Figure 1.3: Schematic of a linear accelerator, from [7].

The cyclotron, developed in the 1930s by E. O. Lawrence, makes use of a similar accelerating structure, but is more compact due its design as shown in Fig. 1.4. Particles orbit in a plane between two poles of an external magnet at a frequency known as the cyclotron frequency. The external magnet provides a static magnetic field that holds the particles in the plane while the varying RF fields on each of the D-shaped electrodes, called “dees,” provide the accelerating force. The charged particles accelerate outward from the center of device in a spiral fashion. Due to the electron’s small mass, the cyclotron was limited in energy by relativistic effects [4] and was better suited for heavier particles or nuclei.

A special type of cyclotron, called the “synrocyclotron,” was developed by E. McMillian in the 1940s. In this design, the RF fields are varied to compensate for the relativistic effects. Wilderöe suggested a new design such that charged particles form the secondary loop of a transformer [4]. In this new device, called a “betatron,” the magnetic field is increased as the particles accelerate. The particle trajectories remain circular and with a constant radius [8]. Independently, D. Kerst built the first betatron in 1940 that produced 2.2 MeV electrons. By 1950, betatron achieved energies of 300 MeV.

To achieve higher energies and to maintain a constant radius, the magnetic field had to be synchronously adjusted with energy of the particle [7]. While a classical cyclotron uses both a constant guiding magnetic field and a constant-frequency electromagnetic field, its successor, the “isochronous cyclotron,” works by local variations of the guiding magnetic field, compensating for the increasing relativistic effects of the particles during acceleration. In a synchrotron, this adaptation is done by variation of the magnetic field strength

in time, rather than in space [6]. In proton synchrotrons, energies of over 1 TeV can be reached. Some energy is lost through synchrotron radiation that is emitted when charged particles are accelerated radially.

During the latter half of the last century, particle accelerator energies nearly doubled every seven years. Since most exotic particles of interest do not exist freely, through consequence of Einstein's famous equation relating energy and matter, exotic particles must be created through collisions at high-energies. The quest for higher energies to unlock new exotic particles has pushed accelerator technology over the last century. The exponential growth in accelerator energy can be summarized in a Livingston chart (see Fig. 1.5). Since the 1980s, the pace of accelerator energies has fallen off. Today, the Large Hadron Collider is the most powerful accelerator in the world. Powered by a proton synchrotron beam line, it can reach energies of seven TeV.

New types of devices using plasma waves to accelerate electrons are being developed. These include the laser wakefield accelerator, plasma wakefield accelerator, plasma beat-wave accelerator, and self-modulated laser wakefield accelerator. These technologies may have the potential to accelerate electrons to a few GeV in about a meter [9].

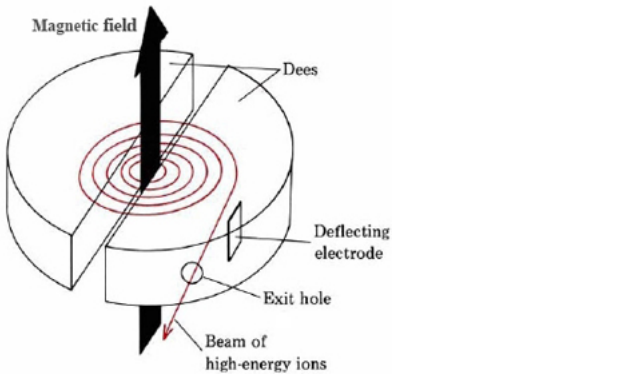


Figure 1.4: Schematic of a cyclotron accelerator, from [7].

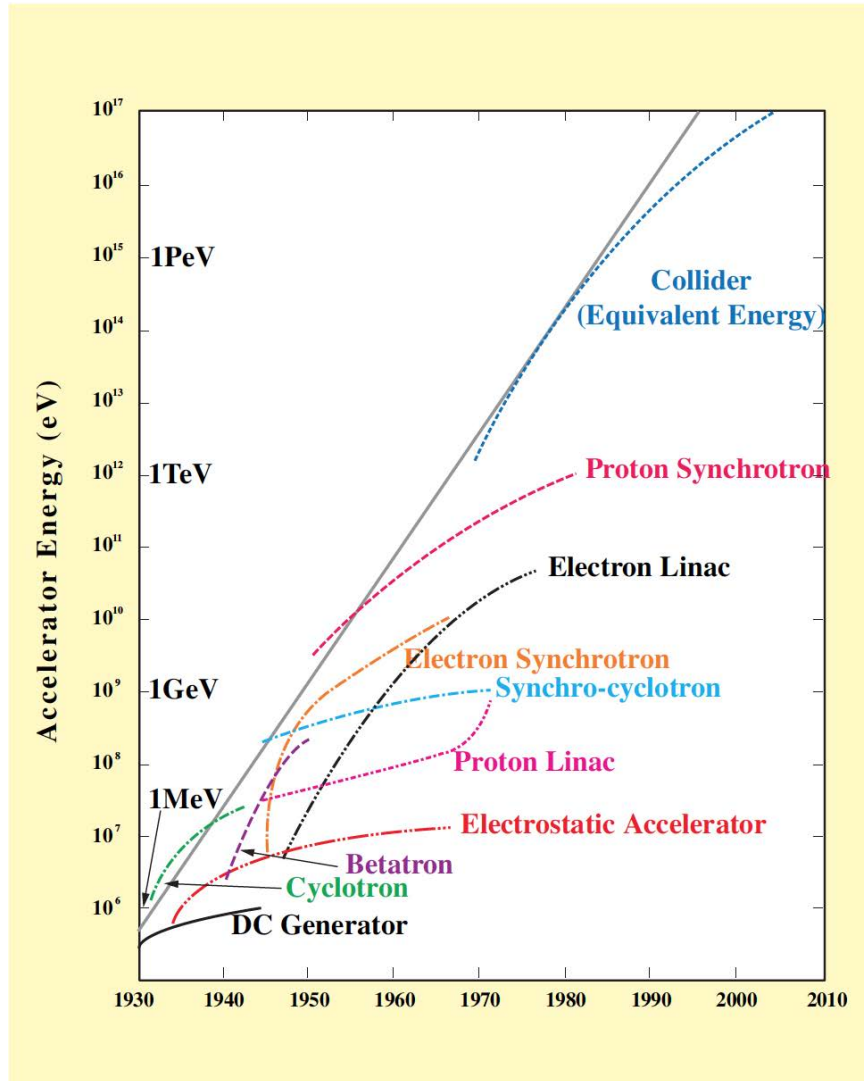


Figure 1.5: Exponential growth of accelerator beam energy, from [5]

THIS PAGE INTENTIONALLY LEFT BLANK

CHAPTER 2:

Laser Accelerator

This chapter will discuss the proposed components for a laser accelerator system using real world examples to frame an engineering estimate for power, size, and cost estimates.

2.1 Laser Accelerator System Overview

This laser accelerator system has three major components:

1. Laser source - provides the high electric field used in accelerating the electrons
2. Electron injector - produces a beam of electrons and directs into the interaction region at an initial angle and energy
3. External magnet - provides the magnetic field component of the Lorentz force that enables coupling between the electrons and laser light

2.2 Laser Source

High peak power lasers with large electric fields can be laboratory scale and provide the force for significant particle acceleration. As an example of high peak power laser technology, the Texas Petawatt Laser (TPL) at the University of Texas at Austin's Center for High Energy Density Science can reach energies of 200 J in 170 femto-seconds, or over 1.1 petawatts (PW) peak power [2], [10], [11]. The laser system provides two beam lines directed into three different target chambers for scientific experiments. The main beam line is based on optical parametric chirped pulse amplification (OPCPA) followed by power amplification in two types of neodymium-doped glass [2]. Several experiments planned for the Texas Petawatt Laser (TPL) include: production of fusion neutrons, study of laser heated matter, dynamics of shocked materials, radiative hydrodynamics, bright x-ray research, and particle acceleration [10].

TPL produces 170 fs pulses at 1057 nm central wavelength [11]. Users can select several energy levels from 60-200 J per pulse at a rate of one shot per hour, or 7 J per pulse at four shots per hour [11]. Table 2.1 summarizes the laser system specifications [2].

Table 2.1: Petawatt Laser System Specifications, after [2]

	Short Pulse	Long Pulse
Pulse Energy	200 J	500 J
Pulse Duration	170 fs	2-20 ns
Wavelength	1057 nm	527 nm
Repetition rate	1 shot/hour	1 shot/hour
Focused intensity	$> 10^{21} \text{ W/cm}^2$	10^{17} W/cm^2

At the heart of the petawatt laser system are three OPCPA stages that are used to amplify the seed oscillator energy from mJ to nearly 200 J per shot. OPCPA techniques are the latest generation of chirp pulse amplification (CPA) technology. CPA has enabled scientists to push the envelope of peak power systems from gigawatts to petawatts in the past 30 years. CPA was first demonstrated by D. Strickland and G. Mourou in 1985 [3]. We will briefly describe how CPA and OPCPA work.

Consider a Gaussian pulse written in the following form [3]:

$$E(t) = E_o e^{-a_p t^2} e^{i(\omega_o t + b_p t^2)} \quad (2.1)$$

where E_o is the peak electric field strength, a_p is a measure of the Gaussian pulse length, b_p is the linear chirp parameter, and ω_o is the light's central angular frequency. The first exponential factor describes the Gaussian envelope and the second term describes the phase. The total instantaneous phase is given by [3]:

$$\phi_{\text{total}} = \omega_o t + b_p t^2. \quad (2.2)$$

The instantaneous frequency is defined as [3]

$$\omega_i(t) \equiv \frac{d\phi_{\text{total}}}{dt}. \quad (2.3)$$

Therefore, the instantaneous frequency for the pulse given by Eq. (2.1) is [3]

$$\omega_i(t) = \omega_o + 2b_p t. \quad (2.4)$$

As can be seen from Eq. (2.4), the instantaneous signal frequency increases with time that is called an up-chirp for $b_p > 0$. Down-chirp pulses have their signal frequency decreasing with time with $b_p < 0$. Exponential chirps are also possible. The pulse can acquire a chirp during transmission through a dispersive or nonlinear medium. Fig. 2.1 shows a chirped Gaussian pulse.

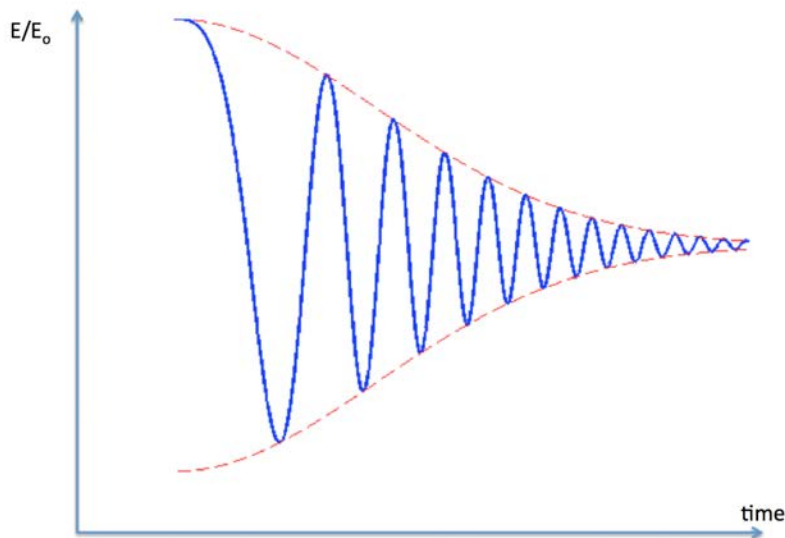


Figure 2.1: Diagram illustrating chirped Gaussian laser pulse. The blue curve represents the highly chirped signal. The red curve represents the Gaussian envelope.

Fig. 2.2 illustrates basic the concept of chirped pulse amplification [12]. An oscillator produces a short pulse (1), which is then fed into gratings that stretch the pulse temporally out by 10^3 - 10^5 times (2). The gratings cause the low-frequency components to travel a shorter path than the high-frequency components, thereby giving it an up-chirp. The result is a temporally stretched pulse with a low enough peak power to safely pass through the main laser gain medium usually Nd:glass or Ti:sapphire (3). The amplified pulse is then recompressed with gratings giving it a down-chirp resulting in a very short and high energy pulse (4).

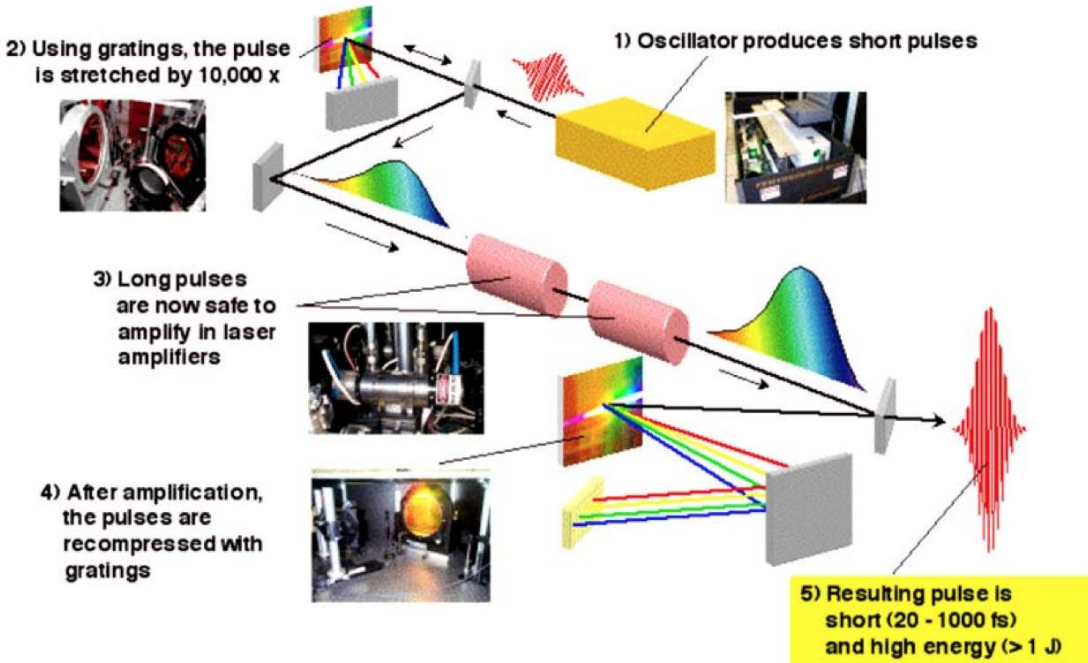


Figure 2.2: Diagram illustrating chirped pulse amplification, from [12].

Parametric amplification is an effect where the dielectric polarization responds nonlinearly to the electric field of input light. A higher frequency laser, known as the pump, is shined onto the parametric crystal resulting in a splitting of the pump photon into a pair of lower frequency photons. The input consists of a pump and signal photons while the output consists of residual pump, signal, and idler photons respectively such that $\omega_i = \omega_{rp} - \omega_s$. The phase relationship between signal and pump determines the direction of energy flow whether there is amplification or deamplification of the signal [13]. Several benefits of parametric amplification include: a much wider range of acceptance wavelengths compared to laser amplifiers, higher gain per unit length of gain material in pulsed mode, good thermal properties since there is very little absorption in the nonlinear crystal. Disadvantages of parametric amplification include no pump energy accumulation in the gain medium, precise pump and signal synchronization, and losses introduced by idler photons [14].

OPCPA combines the techniques of CPA and parametric amplification to achieve very high peak power in ultrashort pulses. The main thrust of OPCPA is to amplify a short laser

pulse while mitigating some deleterious nonlinear effects, such as self-focusing and phase modulation. TPL makes extensive use of OPCPA technology and begins with a 100 fs tunable oscillator [2]. The pulse is stretched to 2 ns as described by the CPA techniques above. There are three stages of parametric amplification using nonlinear crystals. Stage one consists of three beta barium-borate (BBO) crystals and a Nd:YAG pump laser. Stage two uses a pair of BBO crystals also pumped by a Nd:YAG laser. Stage three uses a 532 nm, 4 J, custom laser pump and two potassium deuterium phosphate (KDP) crystals. The final preamplifier stage is a Ti:sapphire crystal. The light source for pumping is residual light from the YAG in the 2nd or 3rd stage. This then feeds the main amplifier comprised of two Nd:glass amplifiers. Pulse energy is increased to about 300 J. Finally, light is passed to the compressor where it is housed in a 7x11 foot vacuum vessel. A multilayer dielectric diffraction grating brings the pulse energy down to approximately 200 J, 150 fs and is directed to the target bay for experiments [2].

OPCPA enables high gain, small thermal management issues (due to pulse stretching), flexible peak gain, and spectral gain [10].

TPL is electrically powered with a large capacitor bank next to the laser/target bay rooms. Total stored energy is approximately 2 MJ. Fig. 2.3 illustrates the layout and size of system with the laser bay and target area comprising of approximately 1500 square meters [10].

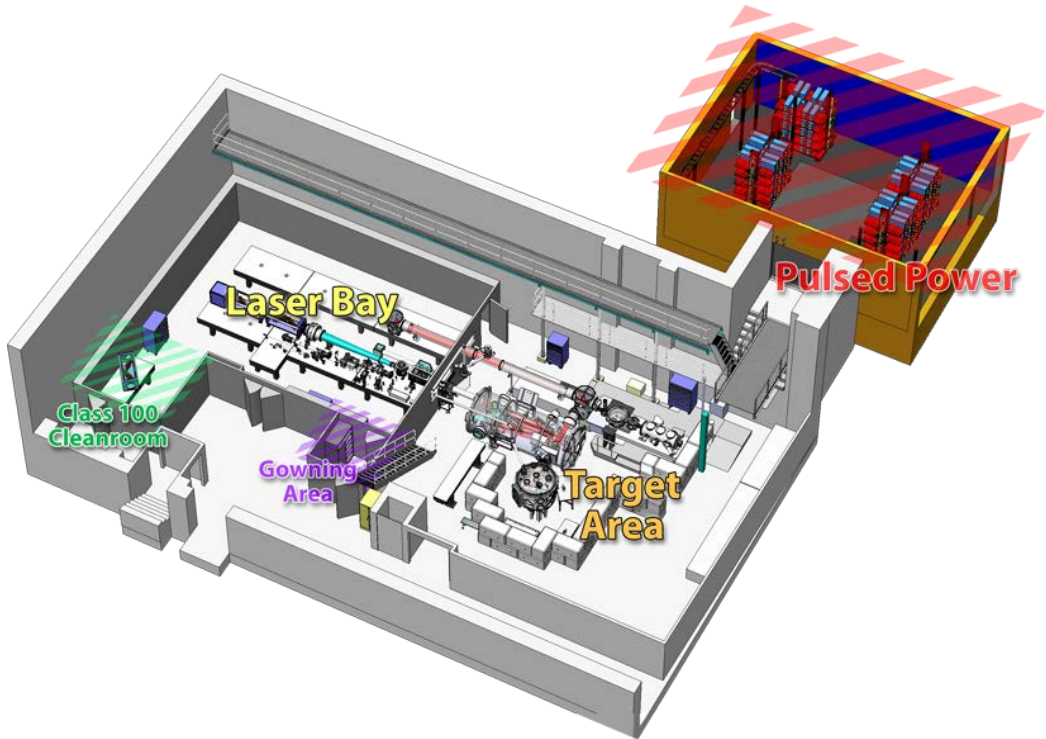


Figure 2.3: A schematic diagram that illustrates laser bay, target bay, and capacitor bank rooms, from [10]

2.3 Electron Injector

Electron injectors, or electron guns, come in many different varieties and configurations. The basic components of all electron injectors are the cathode for emitting electrons into free space, a beam focusing structure usually comprised of electromagnets, and the subsequent accelerating cavities. Injectors can be classified by their:

1. Emission mechanism: thermionic, photocathode, or field emission cathode.
2. Electric field generation: static field or direct current (DC) guns, radio-frequency (RF) guns, normal conducting RF (NCRF) guns, or superconducting RF (SCRF) guns.

Other performance properties that are important include: average beam current, peak beam current, electron pulse length, emittance, physical size, cooling, reliability, and cost.

Thermionic emission of electrons uses the heat-induced ejection of electrons from a metal or non-metal surfaces. A common example of this is a vacuum tube where a hot filament is used to impart sufficient kinetic energy to electrons so they can overcome the metal's work function at the surface. A positive anode is placed some distance away from the surface so that the resulting electrostatic force will pull the electrons into vacuum away from the cathode where they can be further accelerated.

Photocathode emitters eject electrons from the cathode by the photoelectric effect. A drive laser source shines light energy onto a metal or semiconductor surface [15]. The quantum efficiency (QE) of a cathode is the ratio of the number of electrons generated to the number of incident photons. Metals, such as copper, tend to have a low QE and require a UV drive laser but have a fast response time. Semiconductors, such as gallium arsenide or cesium telluride, have higher QE, and only require a visible drive laser, but have a slower response time. The UV drive laser results in a fast response time while the visible drive laser gives a slower response time.

Field emission cathodes eject electrons from a surface due to a nearby high electric field gradient that lowers the work function so that electrons can tunnel through the barrier and escape. Field emission cathodes are also considered cold cathodes since a heating element is not present. Field emitters structures tend to have spikes or sharp tips that greatly enhance the electric field at the tip near the surface. Recent papers have shown that carbon nanotubes may be excellent field emitters [16].

Following the cathode emission section of the electron gun, DC or RF fields provide the initial stage of acceleration. RF cavity shapes can vary from pillbox, elliptical, quarter-wave, or spoked. Spoke cavities, see Fig. 2.4, are a coaxial half-wave length cavity with an outer conductor turned ninety degrees so that its axes is directed along the beam path [17].

Electron guns with a photocathode can be combined with a DC, NCRF, or SCRF accelerating cavity section. NCRF gun operations span a broad range of RF frequencies ranging from a few MHz to several GHz. The RF field and the drive laser pulses must be carefully synchronized so that the electrons ejected via the photoelectric effect are properly accelerated.

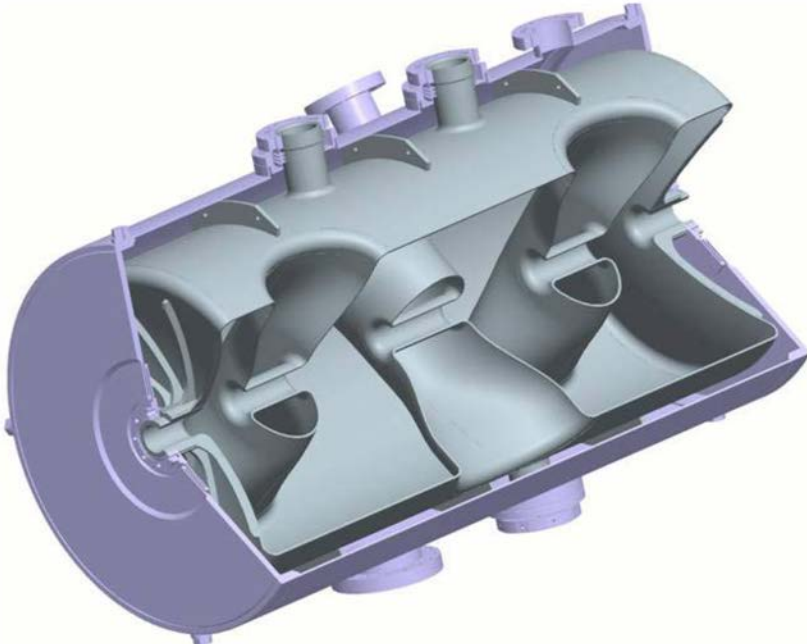


Figure 2.4: Cross-section of a triple spoke cavity, from [17]

In NCRF, resistive losses cause the cavity walls to heat up and require cooling systems based on a water heat-exchanger. Heating is greatly reduced through use of a superconducting cavity but system complexity and cost is increased. The liquid-He requirement for some super-conducting cavities may be somewhat mitigated by choosing a lower RF band. For RF of less than about 500 MHz, a liquid-He system of only 4K is sufficient. A 2K liquid-He system is required for RF greater than about 500 MHz.

Electron guns can be continuous wave or pulsed. A particle synchronized with the RF field is called a synchronous particle. Particles bunched near the synchronous particle in the oscillation of the RF field is called a bucket. Electrons can be present in each RF bucket, or in pulsed guns where certain RF buckets are filled. Typical frequencies are a few MHz to several gigahertz with bucket charges from pC to nC per bunch.

As mentioned earlier, electron beam emittance is an important quality to consider. It is a measure of particle spread in position and angle and is typically measured in units of

mm-mrad. Normalized emittance, ϵ_n is defined as

$$\epsilon_n = \gamma_0 \langle r \rangle \langle \theta \rangle \quad (2.5)$$

where γ_0 is the beam Lorentz factor, $\langle r \rangle$ is the average spread in particle position and $\langle \theta \rangle$ is the average spread in particle angle. As we will see later, the electron beam positions must be well inside the optical mode of the laser to be accelerated. For a relatively good beam emittance of 10 mm-mrad and $\gamma_0 = 130$, the spread in position and angles must be less than 0.08 mm-mrad. We shall see later that this is a sufficiently small spread in angles in order to achieve optimal energy gain.

The Naval Postgraduate School and Niowave, Inc have designed and developed the Mark I SCRF injector (see Fig. 2.5). This design uses a quarter wave structure, which are known to achieve a high accelerating efficiency. Furthermore, operating at a low RF band of 350 MHz allows use of a 4 K helium refrigeration system thereby greatly minimizing the complexity of total system. The Mark I uses an RF-coupler with a nominal electron beam energy of a few MeV.



Figure 2.5: Naval Postgraduate School SCRF Gun

2.4 External Magnetic Field

The external magnetic field in the laser accelerator system serves to provide coupling between the electron beam trajectory and the laser's transverse electric field. It will be shown that magnetic field strengths on the order of 30 T to 60 T provide for sufficient electron coupling. We will find that higher magnetic fields allow the initial electron energy and electron injection angle to be much lower.

An example of high magnetic field technology, consider the National High Magnetic Field Laboratory (NHMFL). NHMFL currently holds the record for the strongest continuous static field in the world at 45 T. NHMFL is a federal-state research facility in partnership with Florida State University, the University of Florida, and Los Alamos National Laboratory under a National Science Foundation grant. Its mission: "To provide the highest magnetic fields and necessary services for scientific research conducted by users from a wide range of disciplines, including physics, chemistry, materials science, engineering, biology and geology" [20]. There are several magnet types available for scientists to conduct basic research. Table 2.2 summarizes some of NHMFL's magnets that are available [18].

Table 2.2: Available Magnets at the National High Magnetic Field Laboratory, after [18]

Field [T]	Bore [mm]	Power [MW]
Resistive and Hybrid Magnets		
20	195	20
24.5	32	14
25	52	19
27	32	14
30	32	16
33	32	16
45	32	15
Superconducting Magnets		
Temperature		
15	45	10 mK - 1 K
17.5/19.5	52	0.4 - 300 K
18/20	52	20 mK - 2 K

The Hybrid Magnet at the NHMFL is the world record holder for continuous magnetic field (see Fig. 2.6). It consists of a room temperature magnet (31 T) surrounded by a superconducting magnet (14 T) to produce a continuous, static, 45 T field in its 32 mm

bore over one m length. The power supply is rated for 40 MW [20]. The cooling system is buffered by a 3800 m³ cold water storage tank that is maintained at 7°C by a 28 MW chiller [20], [21].

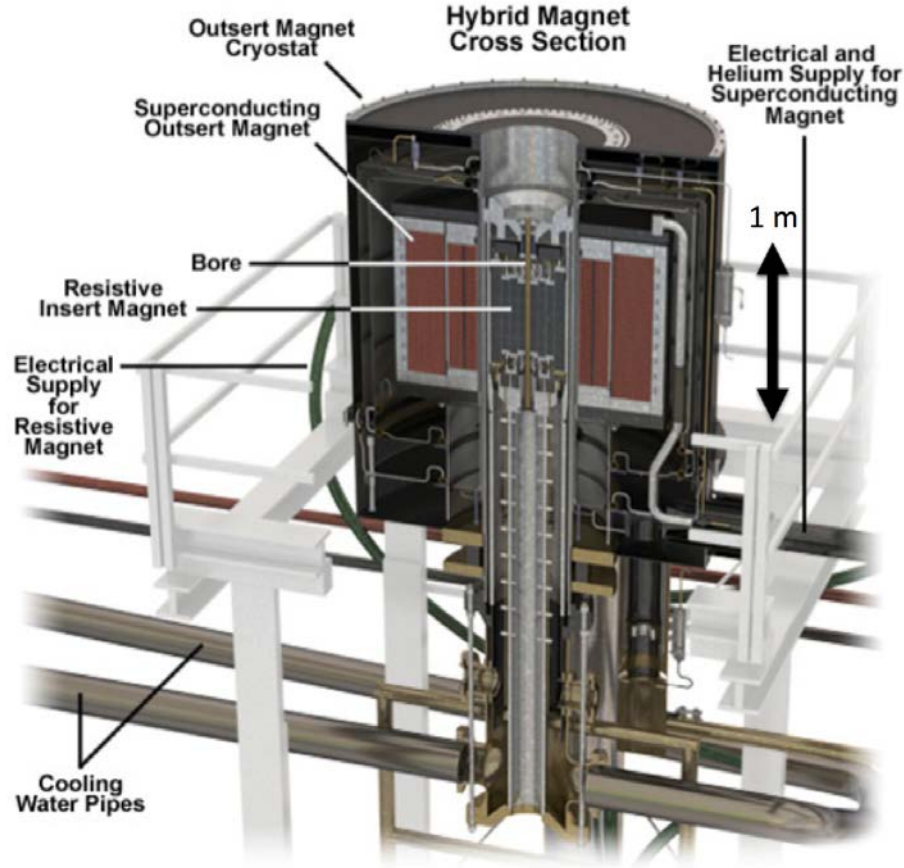


Figure 2.6: Cutaway diagram of NHMFL 45T Hybrid magnet, from [21].

The superconducting “outsert” magnet wraps around the room temperature magnet. It is comprised of three connected subcoils in series with a design current of 10 kA. Each subcoil is made with of a niobium-tin alloy with a combined stored energy of nearly 100 MJ. Many of the supported research areas for the hybrid magnet include: condensed matter physics, quantum hall effects, high temperature superconductivity, geochemistry, optical microscopy, resonant ultrasound spectroscopy and NMR studies, for example. The system was design for maximum user-friendliness, easy access to bore experiment area, and a

10-year life with 2000 charge/discharge cycles for the “insert” or inner restive magnet [22].

For use within the laser accelerator system, static and continuous magnetic fields may not be needed because the time-scales of interaction are very short, typically < 10 ns. Pulsed-field systems are able to provide long duration pulses compared to the time-scales of interaction for the laser accelerator are in effect “static.” NHMFL Pulsed-Field Facility (PFF) at Los Alamos National Laboratory (LANL) offers researchers access to various capacitor driven magnets up to fields of 100 T (see Table 2.3) [19]. The fields can be maintained over a length of about one meter.

The PFF system (see cutaway Fig. 2.7) combines a 40T outer magnet with a 60T field created by a capacitor-bank insert. The power system consists of a 1.43 GW generator combined with seven 64 MW power supply modules [23] driving each of the magnet’s seven coils.

NHMFL Pulsed Field Facility is currently designing the next generation of non-destructive pulsed field magnets. The 100T magnet is a joint project between the National Science Foundation and the Department of Energy. Pulses up to 100T for periods of milliseconds will be available for users. Table 2.4 recaps the systems we have used in our examples.

Table 2.3: Available Pulsed Magnets at PFF LANL. SP = Short Pulse. MP = Mid-Pulse, after [19]

Cell No.	Magnet	Pulse Duration (ms)	Bore (mm)
1	50 T SP	25	24
2	40 T MP	400	24
2	50 T MP	400	15
3	60 T SP	25	15
4	65 T SP	25	15
5	60 T SP	25	15

Table 2.4: Magnet Specification Summary, after [19].

System	Power	Cooling Power	Volume
45T Hybrid Pulsed	25 MW (continuous) 1.43 GW @ 85 ms	9 MW 5 MW	175 m ³ 35 m ³

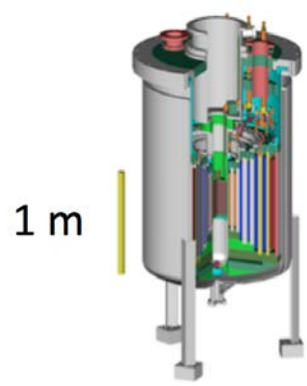


Figure 2.7: Cutaway diagram of NHMFL 100T pulsed magnet system, after [19]

THIS PAGE INTENTIONALLY LEFT BLANK

CHAPTER 3:

Equations of Motion

3.1 Relativistic Lorentz Force

We begin the laser accelerator analysis by considering whether a classical or quantum mechanical treatment is required. The injector gives the electrons an energy of about 120 MeV with a one per-cent energy spread as input to the laser accelerator. This corresponds to a spread in electron wavenumbers of

$$\Delta k_e = \frac{\Delta \mathcal{E}}{\hbar c} \approx 6 \cdot 10^{12} \text{ m}^{-1}. \quad (3.1)$$

So the corresponding uncertainty in position is

$$\Delta x_e \geq \frac{1}{2\Delta k} \approx 8 \cdot 10^{-14} \text{ m}. \quad (3.2)$$

The uncertainty in position is much smaller than the laser wavelength of 1 μm . The laser accelerator is clearly in a classical regime per Ehrenfest's theorem [24].

Continuing the analysis with the relativistic Lorentz force law in the general case, an electron moving through a magnetic field will spiral around the field lines. Without an applied electric field, the electron will not gain energy. The strong electric fields found in today's high powered lasers can provide huge accelerating gradients. If a laser's electric field can be coupled to an electron's spiral motion, it can lead to significant energy gain. In compact covariant notation, the relativistic Lorentz force law [25] in SI units is

$$\frac{dp^\mu}{d\tau} = m \frac{dU^\mu}{d\tau} = -eF^{\mu\nu}U_\nu \quad (3.3)$$

where $p^\mu = (\gamma mc, \mathbf{p})$ is the four-momentum, $\gamma = 1/\sqrt{1-(v/c)^2}$ is the Lorentz factor, m is the mass of the electron, $U^\mu = \gamma(c, \mathbf{v})$ is the covariant form of the electron's four-velocity, τ is proper time, e is the magnitude of the electron's charge, and $F^{\mu\nu}$ is the field-strength

tensor,

$$F^{\mu\nu} = \begin{pmatrix} 0 & -E_x/c & -E_y/c & -E_z/c \\ E_x/c & 0 & -B_z & B_y \\ E_y/c & B_z & 0 & -B_x \\ E_z/c & -B_y & B_x & 0 \end{pmatrix}. \quad (3.4)$$

We can transform between covariant and contravariant forms of 4-vectors in the usual way using the metric tensor

$$g_{\mu\nu} = \begin{pmatrix} 1 & 0 & 0 & 0 \\ 0 & -1 & 0 & 0 \\ 0 & 0 & -1 & 0 \\ 0 & 0 & 0 & -1 \end{pmatrix}. \quad (3.5)$$

The left-hand side of Eq. (3.3) is a proper time derivative. In order to transform this into a lab-frame time derivative, we make use of the invariance of the spacetime interval. For some inertial frame K , the spacetime differential interval is given by

$$ds^2 = c^2 dt^2 - d\mathbf{x}^2. \quad (3.6)$$

For another inertial frame K' , the interval is

$$ds'^2 = c^2 dt'^2 - d\mathbf{x}'^2. \quad (3.7)$$

For sufficiently small spatial intervals,

$$d\mathbf{x} = \mathbf{v}(t)dt. \quad (3.8)$$

Substituting Eq. (3.8) into (3.6) yields

$$ds^2 = c^2 dt^2 (1 - \beta^2) \quad (3.9)$$

where $\boldsymbol{\beta} = (\beta_x, \beta_y, \beta_z)$ and $\beta^2 = v^2/c^2$. Since $v < c$ in all situations, ds^2 is always greater than zero in Eq. (3.9). For the given metric in Eq. (3.5), positive spacetime intervals are called *timelike*. Timelike intervals are ones where there exists a proper time frame K' such

that the spatial interval, $d\mathbf{x}'$, is zero. So we have from Eq. (3.7),

$$ds'^2 = c^2 dt'^2 = c^2 d\tau^2. \quad (3.10)$$

The spacetime interval is an invariant. Therefore, Eqs. (3.6) and (3.10) are equivalent. Combining the right hand sides of Eqs. (3.9) and (3.10) we now have,

$$c^2 d\tau^2 = c^2 dt^2(1 - \beta^2). \quad (3.11)$$

We can now perform a change of variables in Eq. (3.3) using $dt/d\tau = \gamma$ from Eq. (3.11),

$$\frac{d}{d\tau} = \frac{dt}{d\tau} \frac{d}{dt} = \gamma \frac{d}{dt}. \quad (3.12)$$

Therefore, Eq. (3.3) becomes

$$\frac{dp^\mu}{d\tau} = \gamma \frac{dp^\mu}{dt} = -eF^{\mu\nu}U_\nu. \quad (3.13)$$

We will solve Eq. (3.13) subject to the laser field and an external uniform magnetic field where the appropriate forms for the electric and magnetic fields will be added.

3.2 Equations of Motion

Consider a circularly-polarized plane wave given by the following expressions for the laser electric and magnetic fields, \mathbf{E}_r and \mathbf{B}_r , with an external uniform magnetic field, \mathbf{B}_u , aligned along laser propagation axis, z ,

$$\mathbf{E}_r = E_o(\cos \zeta, -\sin \zeta, 0), \quad (3.14)$$

$$\mathbf{B}_r = \frac{E_o}{c}(\sin \zeta, \cos \zeta, 0), \quad (3.15)$$

$$\mathbf{B}_u = (0, 0, B_u), \quad (3.16)$$

with

$$\zeta = k_r z - \omega_r t. \quad (3.17)$$

The plane-wave phase is given by ζ , the angular frequency of the laser light is given by ω_r , and the laser light wavenumber is given by k_r . Substituting Eqs. (3.15) into (3.4) yields

$$F^{\mu\nu} = \begin{pmatrix} 0 & -\frac{E_o}{c} \cos \zeta & \frac{E_o}{c} \sin \zeta & 0 \\ \frac{E_o}{c} \cos \zeta & 0 & -B_u & \frac{E_o}{c} \cos \zeta \\ -\frac{E_o}{c} \sin \zeta & B_u & 0 & -\frac{E_o}{c} \sin \zeta \\ 0 & -\frac{E_o}{c} \cos \zeta & \frac{E_o}{c} \sin \zeta & 0 \end{pmatrix}, \quad (3.18)$$

for the field-stress tensor. Substituting Eq. (3.18) into (3.3) and running through components $\mu = 0, 1, 2, 3$ results in the following equations:

$$\frac{d\gamma}{dt} = -\frac{eE_o}{mc} [\beta_x \cos \zeta - \beta_y \sin \zeta] \quad (3.19)$$

$$\frac{d}{dt}(\gamma\beta_x) = -\frac{eE_o}{mc}(1 - \beta_z) \cos \zeta - \frac{eB_u}{m}\beta_y \quad (3.20)$$

$$\frac{d}{dt}(\gamma\beta_y) = \frac{eE_o}{mc}(1 - \beta_z) \sin \zeta + \frac{eB_u}{m}\beta_x \quad (3.21)$$

$$\frac{d}{dt}(\gamma\beta_z) = -\frac{eE_o}{mc} [\beta_x \cos \zeta - \beta_y \sin \zeta] \quad (3.22)$$

where $\beta_x = v_x/c$, $\beta_y = v_y/c$, and $\beta_z = v_z/c$. Let us describe the geometry carefully (see Fig. 3.1). Given initial electron energy γ_o we have the following definitions:

$$\beta_o = \frac{1}{\gamma_o} \sqrt{\gamma_o^2 - 1}, \quad (3.23)$$

$$\beta_{zo} = \beta_o \cos \alpha = \frac{1}{\gamma_o} \sqrt{\gamma_o^2 - 1} \cos \alpha, \quad (3.24)$$

$$\beta_{xo} = \beta_{\perp o} \cos \phi_o = \beta_o \sin \alpha \cos \phi_o = \frac{1}{\gamma_o} \sqrt{\gamma_o^2 - 1} \sin \alpha \cos \phi_o, \text{ and} \quad (3.25)$$

$$\beta_{yo} = \beta_{\perp o} \sin \phi_o = \beta_o \sin \alpha \sin \phi_o = \frac{1}{\gamma_o} \sqrt{\gamma_o^2 - 1} \sin \alpha \sin \phi_o \quad (3.26)$$

where α is injection angle of the electron measured from the z axis (optical and magnetic field axis), β_o is the initial electron speed relative to the speed of light, β_{xo} is the x compo-

ment of the initial electron speed relative to the speed of light (similarly for β_{yo} and β_{zo}), $\beta_{\perp o}$ is the perpendicular component of the initial electron velocity relative to the speed of light, and ϕ_o is the initial angle between $\beta_{\perp o}$ and β_{xo} .

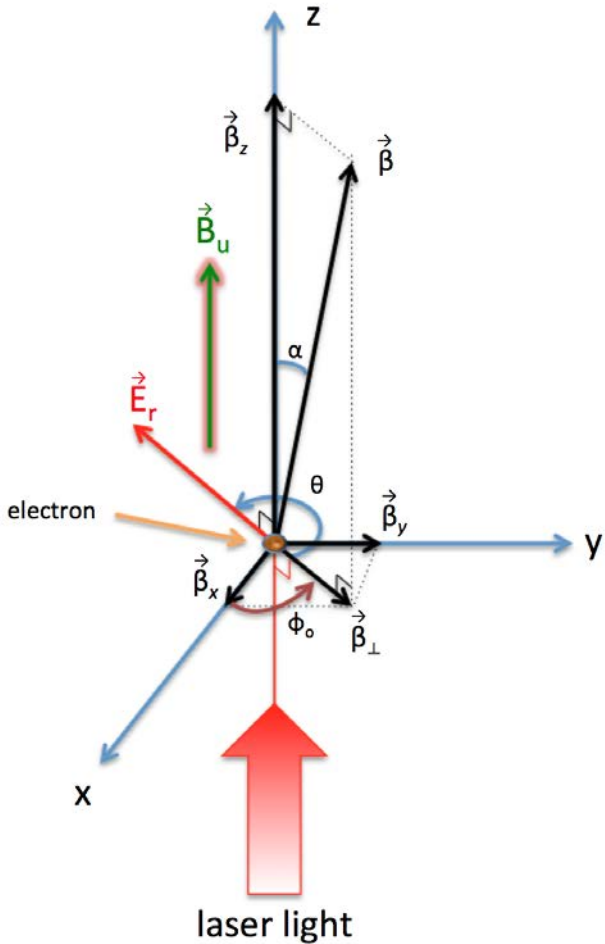


Figure 3.1: Components of the laser accelerator interaction. The electric field vector is given by \mathbf{E}_r . Velocity vector (in units of c) is described by $\boldsymbol{\beta}$ with components β_x , β_y , and β_z . Transverse velocity is given by $\boldsymbol{\beta}_{\perp}$. The injection angle is given by α . The angle between the rotating electric field and $\boldsymbol{\beta}_{\perp}$ is defined as θ . The initial azimuthal angle, ϕ_o , is defined as the angle between the x axis and $\boldsymbol{\beta}_{\perp}$ at $t = 0$. The external external magnetic field is given by \mathbf{B}_u .

Notice that the right-hand side of Eqs. (3.19) and (3.22) are equivalent. Equating the

left-hand sides to each other and integrating gives a constant of motion,

$$\frac{d\gamma}{dt} = \frac{d}{dt}(\gamma\beta_z) \longrightarrow \gamma(1 - \beta_z) = \varepsilon \quad (3.27)$$

where ε is a constant for all time [1]. Both γ and β_z are dynamical variables. As γ increases, the factor $1 - \beta_z$ must decrease to keep ε constant. We can express $\beta_{\perp}^2 = \beta_x^2 + \beta_y^2$ in terms of ε as follows. From the definition of the Lorentz factor we have,

$$\gamma = \frac{1}{\sqrt{1 - \beta^2}} = \frac{1}{\sqrt{1 - \beta_{\perp}^2 - \beta_z^2}} \longrightarrow \beta_{\perp}^2 = \frac{1}{\gamma^2} [\gamma^2 - 1 - \gamma^2 \beta_z^2]. \quad (3.28)$$

Using Eq. (3.27) for β_z^2 results in

$$\beta_{\perp}^2 = \frac{1}{\gamma^2} [2\gamma\varepsilon - \varepsilon^2 - 1]. \quad (3.29)$$

From Eqs. (3.27) and (3.29), as the electron gains energy from the laser accelerator, γ increases. Therefore, β_z will increase while β_{\perp} decreases. The coupling to electric field is governed by β_{\perp} .

Now we will attempt to uncover other constants of the motion by extracting a full time derivative. Consider the following relations,

$$\begin{aligned} \frac{d}{dt} \sin \zeta &= \frac{d}{dt} \sin(k_r z - \omega_r t) \\ &= \cos(k_r z - \omega_r t) \frac{d}{dt} (k_r z - \omega_r t) \\ &= \cos(k_r z - \omega_r t) (k_r \dot{z} - \omega_r) \\ &= -\omega_r (1 - \beta_z) \cos(k_r z - \omega_r t) \\ &= -\omega_r (1 - \beta_z) \cos \zeta \end{aligned} \quad (3.30)$$

and similarly,

$$\frac{d}{dt} \cos \zeta = \omega_r (1 - \beta_z) \sin \zeta. \quad (3.31)$$

Furthermore, applying the chain rule on $d/dt(\gamma\beta_x \sin \zeta)$ and substituting Eq. (3.30) yields

$$\begin{aligned}\frac{d}{dt}(\gamma\beta_x \sin \zeta) &= \sin \zeta \frac{d}{dt}(\gamma\beta_x) + \gamma\beta_x \frac{d}{dt}(\sin \zeta) \\ &= \sin \zeta \frac{d}{dt}(\gamma\beta_x) - \gamma\beta_x \omega_r(1 - \beta_z) \cos \zeta,\end{aligned}\quad (3.32)$$

and also using Eq. (3.31),

$$\frac{d}{dt}(\gamma\beta_y \cos \zeta) = \cos \zeta \frac{d}{dt}(\gamma\beta_y) + \gamma\beta_y \omega_r(1 - \beta_z) \sin \zeta. \quad (3.33)$$

A second constant of motion can be determined by solving Eqs. (3.20) and (3.21) for β_x and β_y :

$$\beta_x = \frac{m}{eB_u} \frac{d}{dt}(\gamma\beta_y) - \frac{E_o}{cB_u}(1 - \beta_z) \sin \zeta \quad (3.34)$$

$$\beta_y = -\frac{m}{eB_u} \frac{d}{dt}(\gamma\beta_x) - \frac{E_o}{cB_u}(1 - \beta_z) \cos \zeta. \quad (3.35)$$

Substituting these equations into Eq. (3.19) and making use of the relations in Eqs. (3.30-3.33) results in

$$\frac{d\gamma}{dt} = -\frac{E_o}{cB_u} \frac{d}{dt}(\gamma\beta_y \cos \zeta) - \frac{E_o}{cB_u} \frac{d}{dt}(\gamma\beta_x \sin \zeta) + \frac{E_o}{cB_u} \gamma(1 - \beta_z) \omega_r(\beta_y \sin \zeta - \beta_x \cos \zeta). \quad (3.36)$$

Using Eq. (3.19) to solve for $(\beta_y \sin \zeta - \beta_x \cos \zeta)$ in terms of $d\gamma/dt$, Eq. (3.36) becomes

$$\frac{d\gamma}{dt} + \frac{E_o}{cB_u} \frac{d}{dt}(\gamma\beta_y \cos \zeta) + \frac{E_o}{cB_u} \frac{d}{dt}(\gamma\beta_x \sin \zeta) - \frac{m}{eB_u} \underbrace{\gamma(1 - \beta_z)}_{\varepsilon} \omega_r \frac{d\gamma}{dt} = 0. \quad (3.37)$$

Extracting an overall time derivative gives

$$\frac{d}{dt} \left[\gamma + \frac{E_o}{cB_u} \gamma \beta_y \cos \zeta + \frac{E_o}{cB_u} \gamma \beta_x \sin \zeta - \frac{m}{eB_u} \varepsilon \omega_r \gamma \right] = 0. \quad (3.38)$$

Factoring γ and making use of the constant ε , defined in Eq. (3.27), yields

$$\frac{d}{dt} \left[\gamma \left(1 + \frac{E_o}{cB_u} \beta_y \cos \zeta + \frac{E_o}{cB_u} \beta_x \sin \zeta - \frac{m}{eB_u} \gamma_o(1 - \beta_{zo}) \omega_r \right) \right] = 0 \quad (3.39)$$

where γ_0 is electron's initial Lorentz factor value at $t = 0$, and ε 's value can be set from initial conditions such that $\varepsilon = \gamma_0(1 - \beta_{zo})$. Multiplying both sides by $eB_u/m\gamma_0$, we can integrate exactly,

$$\gamma \left[\frac{eB_u}{\gamma_0 m} - \omega_r(1 - \beta_{zo}) + \frac{eE_o}{\gamma_0 mc}(\beta_x \sin \zeta + \beta_y \cos \zeta) \right] = \text{constant} \quad (3.40)$$

In Eq. (3.40) we can define the following constants,

$$\omega_c = \frac{eB_u}{\gamma_0 m} \quad (3.41)$$

$$\omega_E = \frac{eE_o}{\gamma_0 mc} \quad (3.42)$$

$$\Delta\omega = \omega_c - \omega_r(1 - \beta_{zo}) \quad (3.43)$$

where ω_c is the relativistic cyclotron frequency, $\Delta\omega$ represents the difference between the relativistic cyclotron frequency and the Doppler shifted light frequency [1], and ω_E is electric field analogue to the relativistic cyclotron frequency. With these substitutions, Eq. (3.40) becomes

$$\gamma[\Delta\omega + \omega_E(\beta_x \sin \zeta + \beta_y \cos \zeta)] = \text{constant} = \eta. \quad (3.44)$$

Two other constants of the motion can be developed from the transverse equations of motion, Eqs. (3.20) and (3.21). The same procedure of eliminating $(1 - \beta_z) \cos \zeta$ in favor of a time derivative can be applied on Eqs. (3.20) and (3.21). For example, substituting Eq. (3.30) into (3.20) yields,

$$\frac{d}{dt}(\gamma\beta_x) = -\frac{eE_o}{mc} \left(-\frac{1}{\omega_r} \frac{d}{dt} \sin \zeta \right) - \frac{eB_u}{m} \beta_y. \quad (3.45)$$

We can factor out a time derivative and integrate the expression exactly giving us

$$\gamma\beta_x - \frac{eE_o}{mc\omega_r} \sin \zeta + \frac{eB_u}{mc} y = \text{constant} = a. \quad (3.46)$$

Similarly, using Eq. (3.31) in (3.21), we arrive at

$$\gamma\beta_y - \frac{eE_o}{mc\omega_r} \cos \zeta - \frac{eB_u}{mc} x = \text{constant} = b. \quad (3.47)$$

Table 3.1 summarizes the equations of motion and constants of motion where the electron phase is $\zeta = k_r z - \omega_r t$. Our goal is to solve these equations for the electron's position and

Table 3.1: Equations and Constants of the Motion

Eq. No.	Differential Equation	Eq. No.	Constant of the Motion
3.19	$\frac{d\gamma}{dt} = -\frac{eE_o}{mc} [\beta_x \cos \zeta - \beta_y \sin \zeta]$	3.27	$\epsilon = \gamma(1 - \beta_z)$
3.20	$\frac{d}{dt}(\gamma\beta_x) = -\frac{eE_o}{mc} \cos \zeta (1 - \beta_z) - \frac{eB_u}{m} \beta_y$	3.44	$\eta = \gamma[\Delta\omega + \omega_E(\beta_x \sin \zeta + \beta_y \cos \zeta)]$
3.21	$\frac{d}{dt}(\gamma\beta_y) = \frac{eE_o}{mc} \sin \zeta (1 - \beta_z) + \frac{eB_u}{m} \beta_x$	3.46	$a = \gamma\beta_x - \frac{eE_o}{mc\omega_r} \sin \zeta + \frac{eB_u}{mc} y$
3.22	$\frac{d}{dt}(\gamma\beta_z) = -\frac{eE_o}{mc} [\beta_x \cos \zeta - \beta_y \sin \zeta]$	3.47	$b = \gamma\beta_y - \frac{eE_o}{mc\omega_r} \cos \zeta - \frac{eB_u}{mc} x$

energy and to determine the optimal conditions for significant energy gain.

3.3 Integral Representation

In order to solve Eqs. (3.19) through (3.22) and arrive at an expression that relates distance traveled in the interaction region to energy gained, it will be beneficial to recast some of the equations in Table 3.1. Consider,

$$\begin{aligned} \boldsymbol{\beta}_\perp \cdot \mathbf{E}_r &= (\beta_x, \beta_y, 0) \cdot E_o(\cos \zeta, -\sin \zeta, 0) \\ &= E_o[\beta_x \cos \zeta - \beta_y \sin \zeta] \\ &= \beta_\perp E_o \cos \theta, \end{aligned}$$

where $\beta_{\perp} = \sqrt{\beta_x^2 + \beta_y^2}$ and $\theta(t)$ is the angle between the electric field vector, \mathbf{E}_r and $\boldsymbol{\beta}_{\perp}$ such that $0 < \theta(t) < \pi$. Therefore,

$$[\beta_x \cos \zeta - \beta_y \sin \zeta] = \beta_{\perp} \cos \theta. \quad (3.48)$$

Also consider the following cross-product,

$$\begin{aligned} \boldsymbol{\beta}_{\perp} \times \mathbf{E}_r &= (\beta_x, \beta_y, 0) \times E_o(\cos \zeta, -\sin \zeta, 0) \\ &= -E_o[\beta_x \sin \zeta + \beta_y \cos \zeta] \hat{\mathbf{z}}. \end{aligned} \quad (3.49)$$

Squaring both sides we have and using the magnitude definition of the cross-product we have,

$$(\boldsymbol{\beta}_{\perp} \times \mathbf{E}_r) \cdot (\boldsymbol{\beta}_{\perp} \times \mathbf{E}_r) = E_o^2 [\beta_x \cos \zeta + \beta_y \sin \zeta]^2 = \beta_{\perp}^2 E_o^2 \sin^2 \theta. \quad (3.50)$$

Therefore,

$$[\beta_x \sin \zeta + \beta_y \cos \zeta] = \beta_{\perp} \sin \theta. \quad (3.51)$$

With Eqs. (3.48) and (3.51) in mind, let's return to Eqs. (3.19) and (3.44). We now have

$$\frac{d\gamma}{dt} = -\frac{eE_o}{mc} \beta_{\perp} \cos \theta \quad (3.52)$$

$$\eta = \gamma(\Delta\omega + \omega_E \beta_{\perp} \sin \theta). \quad (3.53)$$

Note that $dt = \gamma dz/c(\gamma - \varepsilon)$ from Eq. (3.27). Substituting Eqs. (3.29) and (3.42) into Eq. (3.52), we now have,

$$d\gamma = -\frac{\gamma_0 \omega_E}{c} \frac{[2\gamma\varepsilon - \varepsilon^2 - 1]^{1/2}}{(\gamma - \varepsilon)} \cos \theta dz. \quad (3.54)$$

We can eliminate the $\cos \theta$ factor by solving Eq. (3.53) for $\sin \theta$ and noting that $\sin^2 \theta + \cos^2 \theta = 1$, we then have,

$$\cos \theta = \pm \left[\frac{\omega_E^2 (2\gamma\varepsilon - \varepsilon^2 - 1) - (\gamma\Delta\omega - \eta)^2}{\omega_E^2 (2\gamma\varepsilon - \varepsilon^2 - 1)} \right]^{1/2}. \quad (3.55)$$

Substituting the above equation in Eq. (3.54) we arrive at

$$d\gamma = \pm \gamma_o \frac{1}{c(\gamma - \varepsilon)} [\omega_E^2(2\gamma\varepsilon - \varepsilon^2 - 1) - (\gamma\Delta\omega - \eta)^2]^{1/2} dz. \quad (3.56)$$

In utilizing the constants of the motion ε and η , we have arrived at an equation that does not explicitly depend on the angle θ between β_\perp and \mathbf{E}_r . Integrating both sides of Eq. (3.56) gives us

$$\int_{\gamma_o}^{\gamma} \frac{\gamma' - \varepsilon}{[\omega_E^2(2\gamma'\varepsilon - \varepsilon^2 - 1) - (\gamma'\Delta\omega - \eta)^2]^{1/2}} d\gamma' = \int_0^z \frac{\gamma_o}{c} dz' = \frac{\gamma_o z}{c} \quad (3.57)$$

where the negative solution was dropped since we are interested in energy gain. The left-hand side is a family of curves known as curtate cycloids [1], while the right-hand side yields the distance traveled along interaction region.

3.4 Curtate Cycloids

We can motivate a geometric understanding of Eq. (3.57) by considering the mathematics of cycloids. A cycloid is the curve formed by tracing a point either inside, outside, or on the rim of a circle of radius ξ rolling along a straight line [26]. The general equation characterizing the curve is written in parametric form:

$$\begin{aligned} \bar{X} &= \xi \psi - \kappa \sin \psi \\ \bar{Y} &= \xi - \kappa \cos \psi \end{aligned} \quad (3.58)$$

where ξ is the radius of the circle, κ is the distance from the center of the circle from where the curve is traced, ψ is the parametric angle. There are three types of cycloids, as shown in Fig. 3.2. Standard cycloids have $\kappa = \xi$, curtate cycloids have $\kappa < \xi$, and prolate cycloids have $\kappa > \xi$.

Consider a curtate cycloid with $\kappa < \xi$. If we take differentials of Eq. (3.58) then

$$\begin{aligned} d\bar{X} &= (\xi - \kappa \cos \psi) d\psi \\ d\bar{Y} &= \kappa \sin \psi d\psi \end{aligned} \quad (3.59)$$

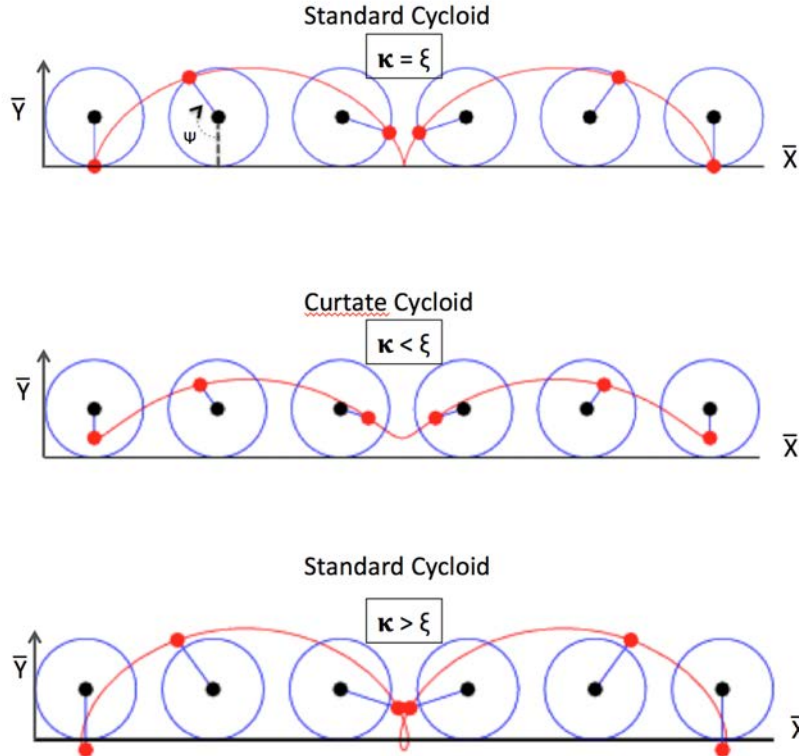


Figure 3.2: Diagram describing different types of cycloids: standard cycloid, curtate, and prolate. The radius of the wheel is ξ . The distance along the radius where curve is drawn is given by κ , from [26].

Now consider the product $\bar{Y} d\bar{Y}$,

$$\bar{Y} d\bar{Y} = (\xi - \kappa \cos \psi)(\kappa \sin \psi d\psi) = \kappa \sin \psi d\bar{X}. \quad (3.60)$$

Therefore,

$$d\bar{X} = \frac{\bar{Y} d\bar{Y}}{\kappa \sin \psi}. \quad (3.61)$$

We can eliminate the $\sin \psi$ term in Eq. (3.61) with the standard Pythagorean trigonometric identity and Eq. 3.58 resulting in

$$d\bar{X} = \pm \frac{\bar{Y} d\bar{Y}}{\sqrt{-\bar{Y}^2 + 2\xi \bar{Y} + (\kappa^2 - \xi^2)}}. \quad (3.62)$$

Notice this expression matches the form of Eq. (3.57). Integrating both sides of Eq. (3.62) in order to get an explicit expression for x as a function of y , we have

$$\bar{X} = \left\{ -\sqrt{-\bar{Y}'^2 + 2\xi\bar{Y}' + \kappa^2 - \xi^2} - \xi \sin^{-1} \left[\frac{\xi - \bar{Y}'}{\kappa} \right] \right\}_{\bar{Y}_o}^{\bar{Y}}. \quad (3.63)$$

We have to be careful when employing the limits of integration since the square-root term must be real and arcsine function is valid only when the argument is less than or equal to $|1|$. The arcsine requirement provides the following constraint on Eq. (3.63):

$$\left| \frac{\xi - \bar{Y}}{\kappa} \right| \leq 1. \quad (3.64)$$

Squaring both sides of Eq. (3.64), we have

$$-\bar{Y}^2 + 2\xi\bar{Y} + \kappa^2 - \xi^2 \geq 0. \quad (3.65)$$

The radicand of the square-root term in Eq. (3.63) matches Eq. (3.65). Therefore, only one constraint on the value of \bar{Y} exists. Solving the inequality gives the following constraint on \bar{Y} :

$$\xi - \kappa \leq \bar{Y} \leq \xi + \kappa. \quad (3.66)$$

Let us consider a simple example where $\xi = 3$ and $\kappa = 1$ in Eq. (3.58). Therefore, the minimum and maximum values for \bar{Y} are 2 and 4, respectively per Eq. (3.66). The explicit function for \bar{X} using Eq. (3.63) is

$$\bar{X}(\bar{Y}) = -\sqrt{-\bar{Y}^2 + 6\bar{Y} - 8} - 3 \sin^{-1}(3 - \bar{Y}) + \frac{3\pi}{2} \quad (3.67)$$

for $2 \leq \bar{Y} \leq 4$. In order to find $\bar{Y}(\bar{X})$ we would need to invert Eq. (3.67) numerically and

use periodic boundary conditions such that minima and maxima of \bar{Y} occur at

$$\begin{aligned}\bar{X}_{\max} &= (2m+1)\pi\xi \\ \bar{Y}_{\max} &= \xi + \kappa \\ \bar{X}_{\min} &= 2m\pi\xi \\ \bar{Y}_{\min} &= \xi - \kappa\end{aligned}\tag{3.68}$$

for $m = 0, 1, 2, 3, \dots$ [26].

In order to make the appropriate comparison to Eq (3.62) we must manipulate Eq. (3.57) a bit. Let $y = \gamma - \varepsilon$ and factor $\Delta\omega$ from the radicand. Therefore, Eq. (3.57) becomes

$$\int_{y_o}^y \frac{y'dy}{\sqrt{-y'^2 + 2\frac{\omega_E^2\varepsilon + 2\eta\Delta\omega - 2\Delta\omega^2\varepsilon}{\Delta\omega^2}y' + \frac{\omega_E^2\varepsilon^2 - \omega_E^2 - \eta^2 + 2\eta\Delta\omega\varepsilon - \varepsilon^2\Delta\omega^2}{\Delta\omega^2}}} = \Delta\omega \frac{\gamma_o}{c} z.\tag{3.69}$$

We can now make the following identifications. The y axis is proportional to the energy of electron and the abscissa is proportional to the z distance traveled by the electron. Relating this to the curtate cycloid, the “radius” of the wheel is related to the amplitude of energy oscillations as the electron moves down the laser accelerator. The radius is given by

$$\xi = \frac{\omega_E^2\varepsilon + 2\eta\Delta\omega - 2\Delta\omega^2\varepsilon}{\Delta\omega^2}\tag{3.70}$$

and the point from the center of the wheel where the curtate cycloid curve is drawn is given by

$$\begin{aligned}\kappa &= \sqrt{\frac{\omega_E^2\varepsilon^2 - \omega_E^2 - \eta^2 + 2\eta\Delta\omega\varepsilon - \varepsilon^2\Delta\omega^2}{\Delta\omega^2}} \\ &\quad + \frac{\omega_E^4\varepsilon^2 + 4\eta^2\Delta\omega^2 + 4\Delta\omega^4\varepsilon^2 + 4\omega_E^2\varepsilon\eta\Delta\omega - 4\omega^2\Delta\omega^2\varepsilon^2 - 8\eta\Delta\omega^3\varepsilon}{\Delta\omega^4}.\end{aligned}\tag{3.71}$$

An explicit equation for distance as a function of energy gained can be immediately identified through Eq. (3.63) with appropriate substitutions for ξ and κ given by Eqs. (3.70) and

(3.71) with the constraints on γ such that $\xi - \kappa \leq \gamma - \varepsilon \leq \xi + \kappa$ with the form

$$z \propto \left\{ -\sqrt{-\gamma'^2 + 2\xi\gamma' + \kappa^2 - \xi^2} - \xi \sin^{-1} \left[\frac{\xi - \gamma'}{\kappa} \right] \right\}_{\gamma_0}^{\gamma}. \quad (3.72)$$

3.5 Resonance Condition

The resonance condition is defined as

$$\begin{aligned} \Delta\omega &= 0 \\ \Delta\omega &= \frac{eBu}{\gamma_0 m} - \omega_r(1 - \beta_z o) = 0 \end{aligned} \quad (3.73)$$

This is the case where the electron's relativistic cyclotron frequency is equal to the Doppler shifted light frequency. When these two frequencies are balanced, the electron experiences a sustained acceleration. Depending on initial conditions, the electron may initially gain or lose energy. Furthermore, if resonance condition satisfied, then it is maintained throughout the interaction. Since ε is a constant of the motion, we can rewrite Eq. (3.73) as

$$\frac{eBu}{\gamma m} - \omega_r \frac{\varepsilon}{\gamma} = 0. \quad (3.74)$$

Multiplying by γ on both sides of Eq. (3.74), we have

$$\frac{eBu}{m} - \omega_r \varepsilon = 0. \quad (3.75)$$

Everything on the left-hand-side of Eq. (3.75) is a constant, therefore $\Delta\omega$ is zero for all time.

There are infinitely many combinations of γ_0 , B_u , λ_r , and β_{zo} in Eq. (3.43) that would drive $\Delta\omega$ to be zero. We can use the resonance condition as a constraint to help us sample the parameter space.

3.6 Electron Phase

Energy gained or lost by electrons in the laser accelerator is given by Eq. (3.52). Recall that θ , a dynamical variable, is the angle between β_{\perp} and \mathbf{E}_r as shown in Fig. 3.1. If $\theta = \pi$, then the right-hand side of Eq. (3.52) is positive since $\cos(\pi) = -1$. Therefore, γ will grow with time. If $\theta = \pi/2$, the right-hand side is zero, γ will be at an extremum. The seemingly worst case for a laser accelerator system is when $\theta = 0$, then the right-hand side of Eq. (3.52) will have the greatest negative value resulting in electrons losing energy. The initial angle between β_{\perp} and \mathbf{E}_r at the start of the interaction is defined to be θ_o .

The phase for each electron given by $\zeta = k_r z - \omega_r t$ will have a value an initial value of $\zeta_o = k_r z_o$ at the start of the interaction since $t = 0$. Experimentally, the laser accelerator would be accepting relativistic electrons from an injector system. There will be a distribution of electrons spread along z as shown in Fig. 3.3. This spread in ζ_o is equivalent to $0 \leq \theta_o \leq 2\pi$ over a wavelength of light. So we expect some electrons to gain energy; some electrons to lose energy. But as we will see in Chapter 5, having an unfavorable θ_o may not be so detrimental for achieving good electron energy gain over the interaction length.

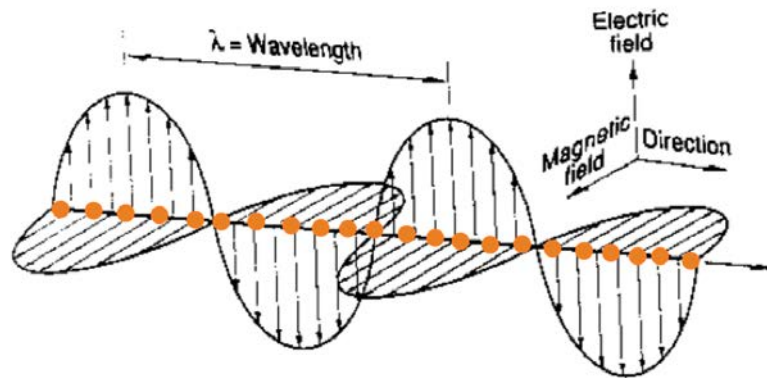


Figure 3.3: Diagram of initial electron distribution in the longitudinal direction over two wavelengths of light. In reality there would be millions of electrons in the distribution, after [27].

3.7 Maximum Energy Gain

The ideal case for maximum electron acceleration and energy gain is when the resonance condition is met or when $\Delta\omega = 0$ and with $\theta_o = \pi$. With this substitution, Eq. (3.57) becomes,

$$\int_{\gamma_o}^{\gamma} \frac{\gamma' - \varepsilon}{\sqrt{\omega_E^2(2\gamma'\varepsilon - \varepsilon^2 - 1) - \eta^2}} d\gamma' = \frac{\gamma_o z}{c}. \quad (3.76)$$

Integrating both sides and solving for z we have,

$$z = \frac{c}{\gamma_o} \frac{1}{3\omega_E^4\varepsilon^2} \left[\sqrt{2\omega_E^2\varepsilon\gamma' - \omega_E^2\varepsilon^2 - \omega_E^2 - \eta^2} \left(\omega_E^2\varepsilon\gamma' + \omega_E^2\varepsilon^2 + \omega_E^2 + \eta^2 - 3\omega_E^2\varepsilon^2 \right) \right]_{\gamma_o}^{\gamma}. \quad (3.77)$$

For large values of γ , $z \propto \gamma^{3/2}$ [1].

As mentioned before, there are infinitely many combinations of γ_o , B_u , λ_r , and β_{zo} for resonance to be met. Practically, an experiment can be setup by choosing the laser and an external magnetic field leaving γ_o and β_{zo} as free variables in order to find resonance. At resonance using Eq. (3.41) we have,

$$\Delta\omega = \frac{eB_u}{m\gamma_o} - \omega_r(1 - \beta_{zo}) = 0$$

so,

$$\frac{eB_u}{m\gamma_o} = \omega_r(1 - \beta_{zo})$$

Using Eq. (3.27) we have

$$\varepsilon = \frac{eB_u}{\omega_r m}. \quad (3.78)$$

With Eqs. (3.24) and (3.78), noting that $\beta_{zo} = (\gamma_o - \varepsilon)/\gamma_o$ again from Eq. (3.27), we can solve for the injection angle

$$\alpha = \cos^{-1} \left\{ \frac{\gamma_o - \varepsilon}{\sqrt{\gamma_o^2 - 1}} \right\} = \cos^{-1} \left\{ \left[\frac{\gamma_o - \frac{eB_u}{\omega_r m}}{\sqrt{\gamma_o^2 - 1}} \right] \right\}. \quad (3.79)$$

In order for α to be a real-valued angle, there's a requirement on the inverse-cosine function

of Eq. (3.79) such that the argument must be less than or equal to one,

$$\left| \frac{\gamma_o - \epsilon}{\sqrt{\gamma_o^2 - 1}} \right| \leq 1. \quad (3.80)$$

Squaring both sides and completing the inequality for γ_o gives us a minimum to achieve resonance,

$$\gamma_{\min} = \frac{\epsilon^2 + 1}{2\epsilon} = \frac{(\frac{eB_u}{\omega_r m})^2 + 1}{2(\frac{eB_u}{\omega_r m})}. \quad (3.81)$$

CHAPTER 4:

Numerical Methodology

4.1 Finite-difference Method

Both Eqs. (3.72) and (3.77) represent analytical solutions for the off-resonance and resonance cases, of distance along z as a function of γ respectively; but they are quite unwieldy. Finite difference numerical integration methods provide a much cleaner solution.

We can rewrite Eqs. (3.19) through (3.22) in terms of four-momentum components. Recalling that $p^\mu = m\gamma(c, v_x, v_y, v_z)$ we have,

$$\frac{dp^0}{dt} = -\frac{eE_o}{\gamma mc} [p^1 \cos \zeta - p^2 \sin \zeta] \quad (4.1)$$

$$\frac{dp^1}{dt} = -eE_o \left(1 - \frac{p^3}{\gamma mc} \right) \cos \zeta - \frac{eB_u}{\gamma m} p^2 \quad (4.2)$$

$$\frac{dp^2}{dt} = eE_o \left(1 - \frac{p^3}{\gamma mc} \right) \sin \zeta + \frac{eB_u}{\gamma m} p^1 \quad (4.3)$$

$$\frac{dp^3}{dt} = -\frac{eE_o}{\gamma mc} [p^1 \cos \zeta - p^2 \sin \zeta] \quad (4.4)$$

where $\zeta = k_r z - \omega_r t$, $p^0 = \gamma mc$, $p^1 = \gamma m\beta_x c$, $p^2 = \gamma m\beta_y c$, and $p^3 = \gamma m\beta_z c$. Turning the first equation into a finite-difference equation, we have

$$p_{\text{new}}^0 \approx p_{\text{old}}^0 + \left[-\frac{eE_o}{\gamma mc} [p_x \cos \zeta - p_y \sin \zeta] \right]_{\text{old}} \Delta t \quad (4.5)$$

The “old” and “new” labels corresponds to previous time step values and updated time step values, respectively, of the variable in question. We can then determine the value of γ_{new} through

$$\gamma_{\text{new}} = \frac{p_{\text{new}}^0}{mc}. \quad (4.6)$$

Then using Eq. (3.27)

$$\beta_z^{\text{new}} = \frac{\gamma_{\text{new}} - \varepsilon}{\gamma_{\text{new}}} \quad (4.7)$$

since $\varepsilon = \gamma(1 - \beta_z)$ is a constant of the motion. The position in z is then

$$z_{\text{new}} \approx z_{\text{old}} + \beta_z^{\text{new}} c \Delta t. \quad (4.8)$$

Similarly for the x component,

$$p_x^1_{\text{new}} = p_x^1_{\text{old}} + \left[-eE_o \left(1 - \frac{p^3}{\gamma m c} \right) \cos \zeta - \frac{eBu}{\gamma m} p^2 \right]_{\text{old}} \Delta t \quad (4.9)$$

Then

$$\beta_x^{\text{new}} = \frac{p_x^1_{\text{new}}}{\gamma_{\text{new}} m c}. \quad (4.10)$$

Therefore the x -position is

$$x_{\text{new}} \approx x_{\text{old}} + \beta_x^{\text{new}} c \Delta t, \quad (4.11)$$

and similarly for the y component. Since we are updating the new positions on the updated velocities, this is known as Euler-Cromer method [28].

Numerical integration using a 4th order Runga-Kutta (RK4) method was also performed. The percent difference in electron energy gain between RK4 and Euler-Cromer methods is only 0.03 percent. Since the percent difference is negligible, Euler-Cromer methods were employed in the dissertation due to their speed and simplicity.

4.2 Initial Conditions on Resonance ($\Delta\omega = 0$)

The task in this section is to numerically solve the equations in Table 3.1 subject to the electrons entering the interaction region with the resonance condition satisfied such that $\Delta\omega = 0$. We ultimately want to know the energy gained by the electron and its trajectory.

Assume that the initial electron energy and external magnetic field are independently chosen parameters. From Eq. (3.79), we have an equation for the injection angle, $\alpha = \alpha(\gamma_o, B_u)$, as a function of two free variables. The following result shown in Fig. 4.1 is a surface of required injection angles for resonance.

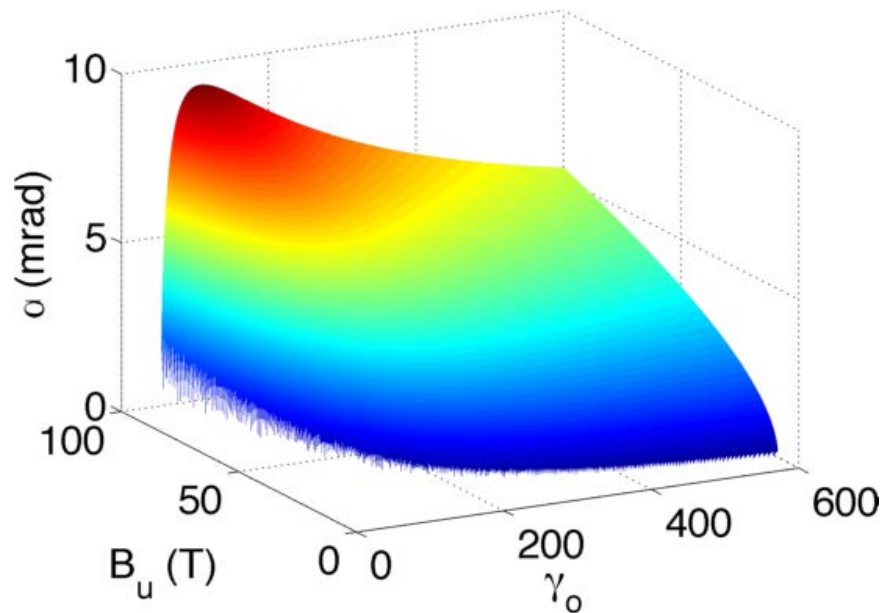


Figure 4.1: Shown is the required injection angle for resonance as a function of initial electron energy, γ_o , and external magnetic field, B_u , for a given ω_r .

If we select a magnetic field strength of 45 T, then we can slice through a constant external magnetic field in Fig. 4.1 resulting in Fig. 4.2. We now have an optimal injection angle for various initial electron energy values where the minimum value of γ_o in Fig. (4.2) is consistent with Eq. (3.81).

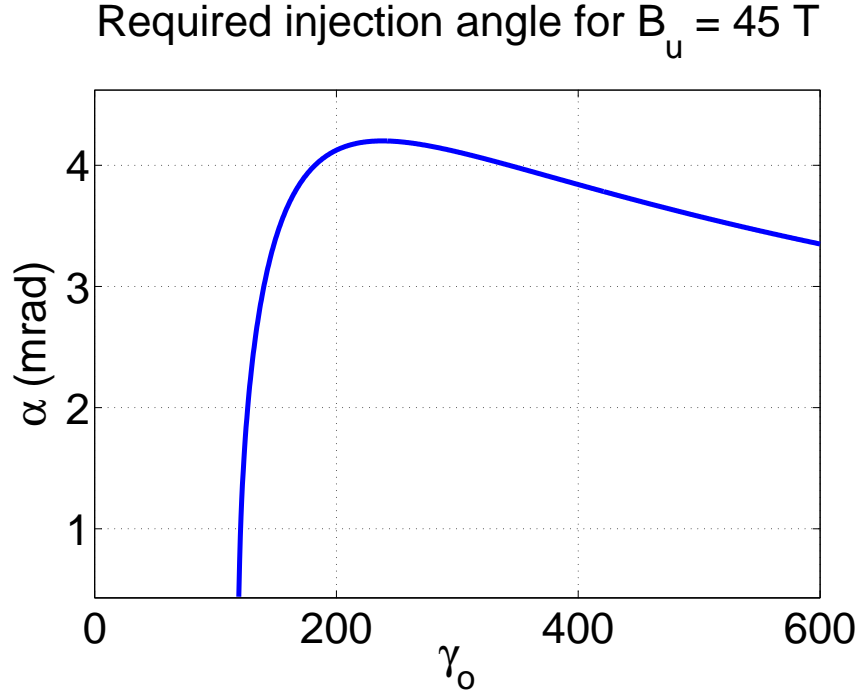


Figure 4.2: Shown is the allowed ordered pair combination of initial electron energy, γ_o and initial injection angle, α for a given magnetic field to guarantee resonance for a given ω_r .

Consider the electron at the start of the laser accelerator system at time, $t = 0$. Using Eqs. (3.15) and (3.17), the electric field, \mathbf{E}_r , is then oriented along the x axis or $\mathbf{E}_r = E_o \hat{\mathbf{x}}$ since $\zeta(t = 0) = k_r z - \omega_r t = 0$. From Eq. (3.52) it would seem that the greatest energy gain would require an anti-alignment between \mathbf{E}_r and $\boldsymbol{\beta}_\perp$ such that $\theta = \pi$ initially. The other spherical coordinate angle, ϕ_o , which is the angle between $\boldsymbol{\beta}_\perp$ and $\boldsymbol{\beta}_{xo}$, is then also equal to π . In general, ϕ_o may take on any value between 0 and π . So, with α and ϕ_o established, the initial conditions for position and velocity can be calculated using Eqs. (3.23) through (3.26).

4.3 Electron Trajectory

For plane-wave propagation (no diffraction) with $\theta = \pi$ for maximum acceleration, both Eqs. (3.52) and (3.56) are equivalent with $\Delta\omega = \eta = 0$. It is straightforward to numerically integrate and update γ . Then for each timestep using the constant of the motion ϵ , β_z can be updated and the position z calculated. The values for β_x and β_y can also be evaluated by

making use of constants a and b where their values are given by initial conditions. From, Eqs. (3.46) and (3.47), β_x and β_y are

$$\beta_x = \frac{1}{\gamma} \left[a + \frac{eE_o}{mc\omega_r} \sin \zeta - \frac{eB_u}{mc} y \right] \quad (4.12)$$

$$\beta_y = \frac{1}{\gamma} \left[b + \frac{eE_o}{mc\omega_r} \cos \zeta + \frac{eB_u}{mc} x \right]. \quad (4.13)$$

We can determine the number of times an electron will spiral around the external magnet's field lines by integrating Eq. (3.41) (and making the substitution of $\gamma(t)$ for γ_o) over the time it takes the electron to clear the interaction region. Stronger magnetic fields results in tighter and more rotations. Trajectories from numerical integration will be shown in Chapter 5.

4.4 Synchrotron Radiation

An estimate of power loss through synchrotron radiation can be made if we consider the simplified case with the laser source switched off. With only the external magnetic field and no laser field present, $E_o = 0$, Eqs. (3.19) through (3.22) reduces to

$$\gamma(t) = \gamma(0) = \gamma_o, \text{ constant} \quad (4.14)$$

$$\frac{dv_x}{dt} = -\frac{eB_u}{m\gamma} v_y \quad (4.15)$$

$$\frac{dv_y}{dt} = \frac{eB_u}{m\gamma} v_x \quad (4.16)$$

$$v_z(t) = v_z(0) = v_{zo}, \text{ constant} \quad (4.17)$$

Eqs. (4.15) and (4.16) can be solved by letting $\rho = v_x + iv_y$ and $\omega_c = eB_u/m\gamma$. Therefore, $\dot{\rho} = i\omega_c\rho$. Solving this with initial conditions yields $\rho(t) = v_{\perp o}e^{i(\omega_ct+\delta)}$ where $v_{\perp o} =$

$\sqrt{v_{xo}^2 + v_{yo}^2}$ and $\delta = \tan^{-1}(v_{yo}/v_{xo})$. Integrating once more yields the following

$$\begin{aligned} x(t) &= \frac{v_{\perp o}}{\omega_c} \sin(\omega_c t + \delta) + x_o - \frac{v_{\perp o}}{\omega_c} \sin(\delta) \\ y(t) &= -\frac{v_{\perp o}}{\omega_c} \cos(\omega_c t + \delta) + y_o + \frac{v_{\perp o}}{\omega_c} \cos(\delta) \\ z(t) &= z_o + v_{zo}t. \end{aligned} \quad (4.18)$$

The radius of the orbit is then given by the cyclotron radius for an electron in a static magnetic field,

$$\begin{aligned} r &= \sqrt{(x(t) - x_o)^2 + (y(t) - y_o)^2} \\ &= \frac{\gamma m v_{\perp o}}{e B_u}. \end{aligned} \quad (4.19)$$

We can calculate the synchrotron power loss using the relativistic Larmor formula given by [29],

$$P = \frac{\mu_o e^2 \gamma^6 c}{6\pi} \left(\dot{\beta}^2 - |\boldsymbol{\beta} \times \dot{\boldsymbol{\beta}}|^2 \right). \quad (4.20)$$

Taking one and two time derivatives of Eqs. (4.18) and substituting into Eq. (4.20) yields,

$$\begin{aligned} P &= \frac{\mu_o e^2 \gamma^6 c}{6\pi} \left(\omega_c^2 \beta_{\perp o}^2 - \omega_c^2 \beta_{\perp o}^2 (\beta_{zo}^2 + \beta_{\perp o}^2) \right) \\ P &= \frac{\mu_o e^2 \gamma^6 c}{6\pi} \omega_c^2 \beta_{\perp o}^2 (1 - \beta^2) \end{aligned}$$

We arrive at [29],

$$P = \frac{\mu_o e^2 \gamma^4 c}{6\pi} \omega_c^2 \beta_{\perp o}^2. \quad (4.21)$$

Plugging in nominal values for an external magnetic field of 45 T and 300 T, we can expect synchrotron energy losses to be on the order of several electron-volts (eV) to 5 keV, respectively. These figures represent an upper-bound estimate energy losses. Once the laser field is present, as will be shown later, γ increases however β_{\perp} is small and its value decreases. For energy gain of approximately one GeV, power loss through synchrotron radiation is negligible.

4.5 Numerical Integration

The numerical integration procedure for off-resonance or resonant analysis begins by selecting global constants such as laser wavelength, laser power, estimated spot size, external magnetic field strength, and time steps. If resonance analysis is required, the angle for resonance based on the global constants is calculated. We compute initial momentum values in preparation for numerical integration. Based on the initial values, we perform Euler-Cromer integration to determine “new” values for γ and the momenta. We use these new values to calculate position and the overall trajectory of the electron. We also calculate power loss through synchrotron radiation and perform diagnostic checks of the code for each time step. Finally, we keep track of the values by writing the data to a file for post-processing in MatLab.

THIS PAGE INTENTIONALLY LEFT BLANK

CHAPTER 5:

Numerical Analysis Results

In this chapter, we will use the numerical integration method previously described to obtain simulation results on the laser accelerator performance for a variety of initial conditions including: on resonance, different values of the initial phase θ_o , the angle between β_\perp and \mathbf{E}_r , off resonance, and real field effects.

5.1 On-resonance with $\theta_o = \pi$

Recall that resonance is defined as $\Delta\omega = 0$ and occurs when the electron “feels” the Doppler shifted circularly-polarized laser light oscillating at the same frequency as the electron’s spiraling motion in the uniform magnetic field. In the simulation, we assume that the external magnetic field B_u and laser source parameters (laser power and wavelength) are fixed. The resonance condition is then a function of the injection angle α and injection energy γ_o as shown in Fig. 4.2.

Let us assume the following for the simulation of a single electron . The laser source will be like the Texas Petawatt Laser (TPL) system. The laser Rayleigh length, Z_r , is assumed to be longer than interaction region of one meter in order to eliminate diffraction effects. Gaussian beam analysis will be considered later in the chapter. The optical mode waist is about 1 mm throughout the interaction region. The external magnetic field is assumed to be static, uniform field throughout the interaction region. Strong magnetic fields support electron to light coupling for energy gain. Let us also assume $\theta_o = \pi$ so that β_\perp is anti-parallel to the electric field of the light as shown in Fig. 3.1.

For the single electron simulation, Table 5.1 summarizes the input parameters.

Performing the numerical integration as described in the previous chapter, we obtain the results shown in Fig. 5.1. The results are compared to the analytic solution given in Eq. (3.77). The percent difference is about 0.2 percent for the final energy of the electron after a one meter long interaction. We compared multiple simulation results to the analytic prediction in regimes where the analytic formation remained valid. In all cases, the simulation

Table 5.1: Input Parameters for Resonance Laser Accelerator Simulation

Variable	Symbol	Value
Initial Electron Lorentz Factor	γ_0	119
Initial Electron Energy	\mathcal{E}_0	61 MeV
Laser Peak Power	P	1 PW
Laser Wavelength	λ_r	1 μm
External Magnetic Field	B_u	45 T
First Constant of Motion	ε	4.2×10^{-3}
Initial Azimuthal Angle	θ_0	π radians
Injection Angle	α	20.8μ radians
Time Step	Δt	50 fs

always closely matched the analytic prediction.

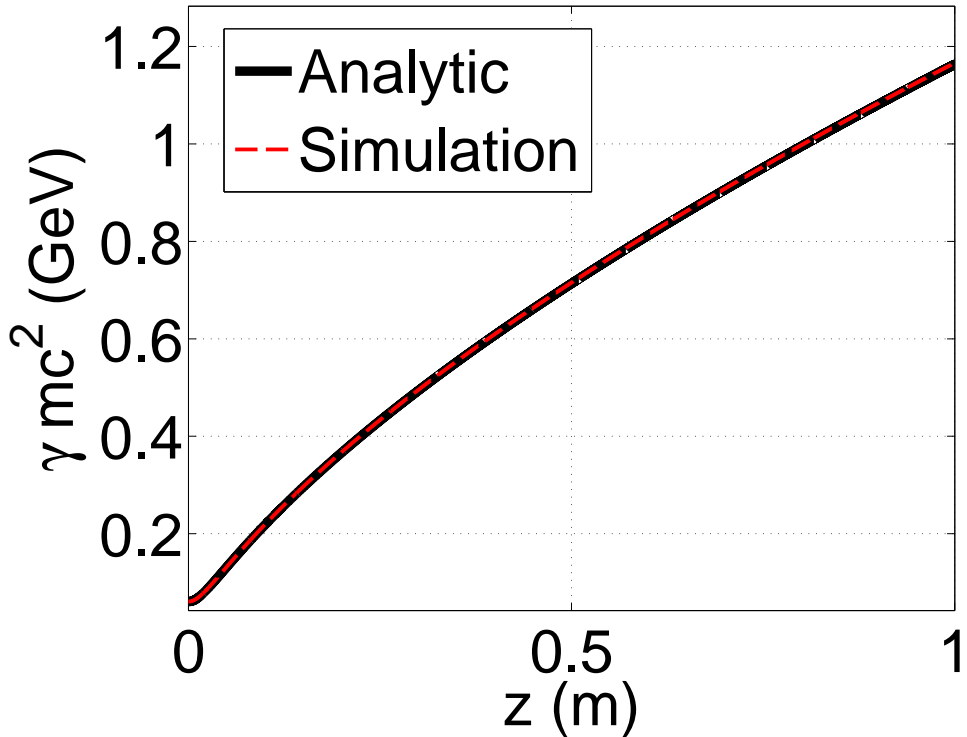


Figure 5.1: Comparison of analytic solution to numerical simulation results of an electron in the laser accelerator. Energy gain versus distance is plotted. The black curve describes the analytic solution and the red curve describes the numerical solution. The difference is about 0.2 percent for the final energy gain, which is approximately 1.17 GeV.

Now that we have established good agreement between analytic and numerical solutions we can now explore how other parameters such as electron radial position and velocity evolution over the interaction region. Fig. 5.2 shows simulation results for two electrons at two different external magnetic field values, 45 T (blue) and 100 T (red) with injection angles α of $20.8 \mu\text{rad}$ and 9.3 mrad respectively for resonance as per Eq. (3.79). The other parameters are the same as in Table ??.

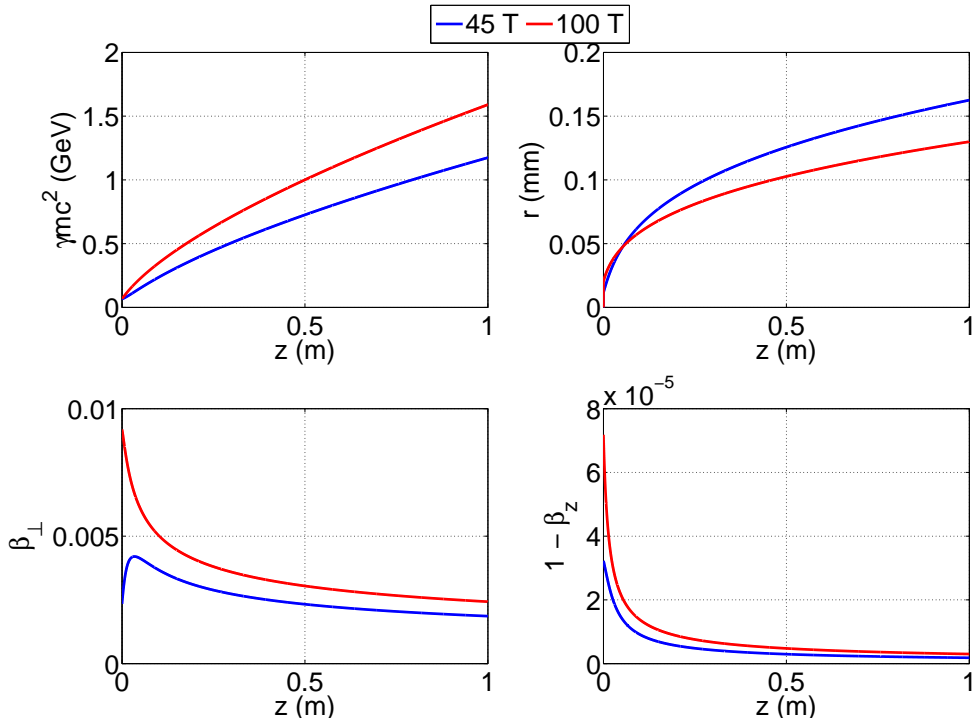


Figure 5.2: Electron simulation results for the parameters given in Table 5.1. The blue curve give results for $B_u = 45 \text{ T}$ while the red curve give results for $B_u = 100 \text{ T}$. The top left graph plots electron energy versus distance traveled. The top right graph plots the radial distance of the electron from the optical axis. The bottom left graph plots β_\perp versus distance traveled. The bottom right graph plots $1 - \beta_z$ versus distance traveled.

The top left curve shows that the electron's energy increases to nearly 1.2 GeV for 45 T and 1.6 GeV for 100 T in one meter. The electron's orbit spirals out to a radius of about 0.17 mm for 45 T and 0.15 mm for 100 T as shown in the top right graph. The value of $1 - \beta_z$ is plotted in the bottom right curve since β_z is nearly unity for the entire length of the interaction region. Note that β_z increases while β_\perp decreases during most of the interaction.

In the bottom left curve, we can see that β_{\perp} has a peak then slowly decreases for the 45 T case while the 100 T does not have a peak. Let us try to understand why β_{\perp} has a peak for the 45 T case while no peak exists for the 100 T case. It is not immediately clear from Eq. (3.29) alone that β_{\perp} should have a maximum. Calculating its derivative we have

$$\begin{aligned} \frac{d\beta_{\perp}}{dz} &= \frac{d}{dz} \left[\frac{1}{\gamma(z)} \sqrt{2\gamma(z)\epsilon - \epsilon^2 - 1} \right] \\ &= \left\{ \frac{\epsilon}{\gamma(z)} [2\gamma(z)\epsilon - \epsilon^2 - 1]^{-1/2} - \frac{1}{\gamma^2(z)} [2\gamma(z)\epsilon - \epsilon^2 - 1]^{1/2} \right\} \frac{d\gamma(z)}{dz} \end{aligned} \quad (5.1)$$

Setting Eq. (5.1) equal to zero we have an extremum when

$$\gamma^* = \frac{\epsilon^2 + 1}{\epsilon}. \quad (5.2)$$

Notice that $\gamma^* = 2\gamma_{\min}$ from Eq. 3.81. Calculating γ^* for 45 T and 100 T cases we have

$$\begin{aligned} \gamma^*(45 \text{ T}) &\approx 238 \\ \gamma^*(100 \text{ T}) &\approx 107 \end{aligned}$$

The value for $\gamma^*(100 \text{ T})$ explains why there is no peak for the 100 T case in Fig. 5.2 since the simulation began with an initial $\gamma_0 = 119$ T. Substituting Eq. (5.2) back into Eq. (3.29) yields

$$\beta_{\perp,\max} = \frac{\epsilon}{\sqrt{\epsilon^2 + 1}}, \quad (5.3)$$

which agrees with the simulation value for $\beta_{\perp,\max}$. In Fig. 5.3, we have again plotted the electron trajectories for two the cases: 45 T field in the blue curve and 100 T field in the red curve. Notice as γ increases along the z axis it causes the radius of spiraling motion around the magnetic field line to increase. There are more numerous spirals for the stronger field. The number of spirals gives an approximate number of wavelengths of light that pass over the electron near resonance. High powered lasers such as the Texas Petawatt Laser produces Gaussian pulses. The Fourier transform of these pulses would also have a spread of frequencies in the frequency domain. As shown in Fig. 5.3, only about ten wavelengths of light pass over the electron. To first order we do not need to be concerned with the effects to the frequency changes associated with the pulse shape.

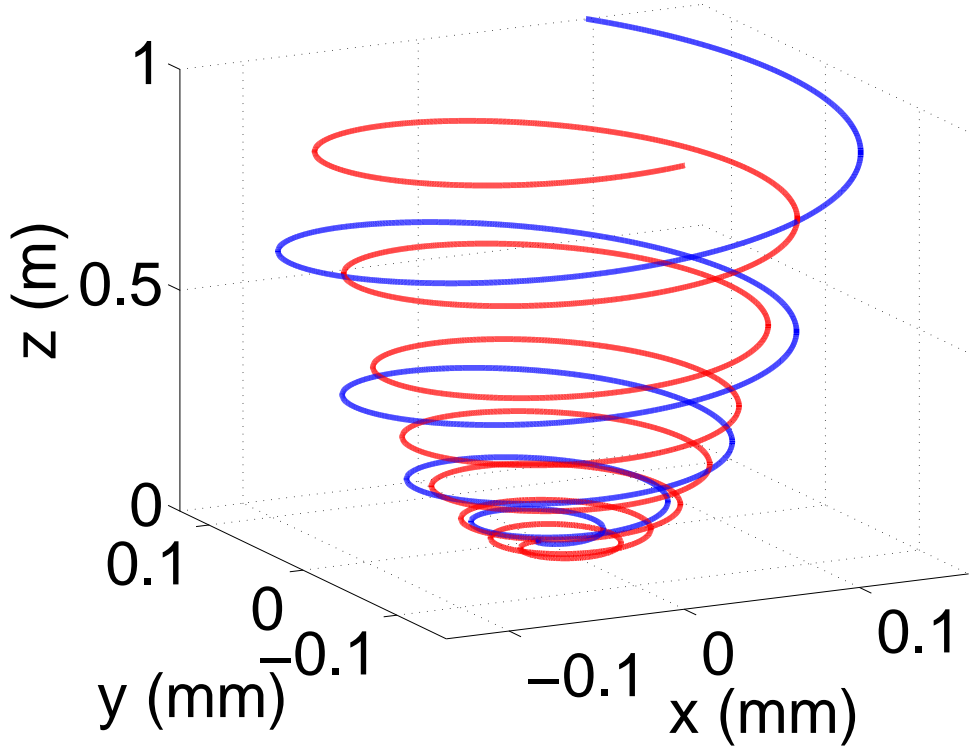


Figure 5.3: Electron trajectories in the laser accelerator for two different external magnetic Field Cases. Laser accelerator for the parameters given in Table 5.1 in the blue curve. The 100 T field trajectory is shown in the red curve for comparison.

Table 5.2 summarizes the simulation results for both cases.

Table 5.2: Results for Single Electron Simulation of Laser Accelerator at 45 T and 100 T

Variable	Symbol	Value at 45 T	Value at 100 T
Final Lorentz Factor	γ_f	2282	3109
Final Energy	\mathcal{E}_f	1.17 GeV	1.59 GeV
Final Electron radial position	r	0.16 mm	0.13 mm

5.2 Electron Phase Performance

A realistic electron bunch is thousands of times longer than a wavelength of light. As mentioned in § 3.6, there will be millions of electrons in each optical wavelength that are randomly distributed in the microscopic longitudinal direction. Recall that $\zeta = k_r z - \omega_r t$

and at time $t = 0$, $\zeta_o = k_r z_o = 2\pi z_o / \lambda_r$. Their initial ζ_o 's will therefore span a 2π range over a distance where z_o changes by a wavelength of light, λ_r . We expect some electrons to gain energy and some electrons to lose energy depending on ζ_o .

We select the coordinate system so that electron is initially at the origin and the laser electric field is initially along the x -axis. In order to sample different microscopic values of ζ_o , we consider three representative values of $\theta_o = 0, \pi/2, \pi$ in the simulations. Recall from Eq. (3.52), that these values are anticipated to cause the electron to initially lose or gain energy.

Consider the following simulation, shown in Fig. 5.4 with $\gamma_o = 130$ (above the minimum energy required for resonance), $B_u = 45$ T, and on resonance injection with $\alpha_{\text{res}} \approx 2.4$ mrad.

In Fig. 5.4, we examine the evolution of energy versus distance traveled for the first 15mm. The middle graph shows β_\perp versus distance. The bottom graph shows the evolution of θ . The colored curves show the evolution of the respective parameter for three different initial θ_o . The black curves show $\theta_o = \pi$, the green curves show $\theta_o = \pi/2$, red curves show $\theta_o = 0$.

In describing the energy plots we must recall Eq. (3.52)

$$\frac{d\gamma}{dt} = -\frac{eE_o}{mc}\beta_\perp \cos \theta.$$

Notice the factor of $\cos \theta$ on the right-hand side of the energy equation. For the $\theta_o = \pi$ case shown by the black curve, the energy initially increases since the right-hand side of Eq. (3.52) is positive. For the $\theta_o = \pi/2$ case shown by the green curve, the energy is initially constant since the right-hand side of Eq. (3.52) is zero. For the $\theta_o = 0$ case shown by the red curve, the energy initially decreases since the right-hand side of Eq. (3.52) is negative.

Let us now look at the perpendicular velocity graphs for β_\perp . For both the $\theta_o = \pi$ and $\theta_o = \pi/2$ cases, β_\perp goes up initially, as shown by the black and green curves, consistent with the electron's increasing energy from the top graph. For the $\theta_o = 0$ case shown by the red curve, β_\perp decreases in value until it reaches zero. When β_\perp goes to zero, the angle θ , shown in the bottom graph, changes from 0 to π quickly. Then β_\perp and the energy both begin to grow. This is a surprising result. It was not expected that an electron that starts out

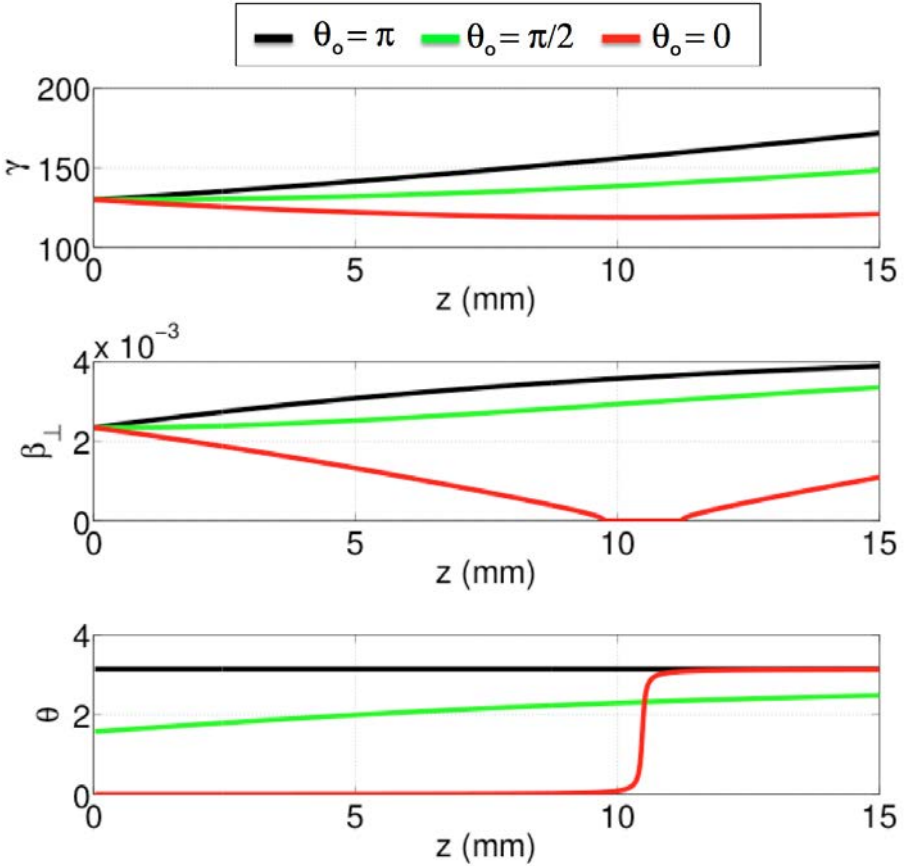


Figure 5.4: Simulation results for on-resonance but different initial θ_o for $\gamma_o = 130$, $B_u = 45$. The top graph shows energy versus distance traveled for the first 15mm. The middle graph shows β_\perp versus distance. The bottom graph shows the evolution of θ . The black curves show $\theta_o = \pi$. The green curves show $\theta_o = \pi/2$. Red curves show $\theta_o = 0$.

moving parallel to the light's electric field would eventually gain energy.

Let us consider a similar analysis of θ_o but with lower initial electron energy of $\gamma_o = 125$ and $\alpha_{\text{res}} \approx 1.8$ mrad. These results are shown in Fig. 5.5. The electron's perpendicular velocity β_\perp starts out with a smaller value than the $\gamma_o = 130$ case since the required injection angle is smaller. So for the $\theta_o = 0$ case, β_\perp goes to zero sooner along the z axis. This causes θ to change to π sooner than the $\gamma_o = 130$ case. We again see that an electron that starts the interaction with an unfavorable θ_o , eventually changes to a favorable θ . Thus they accelerate to high energies along with electrons that initially started with favorable

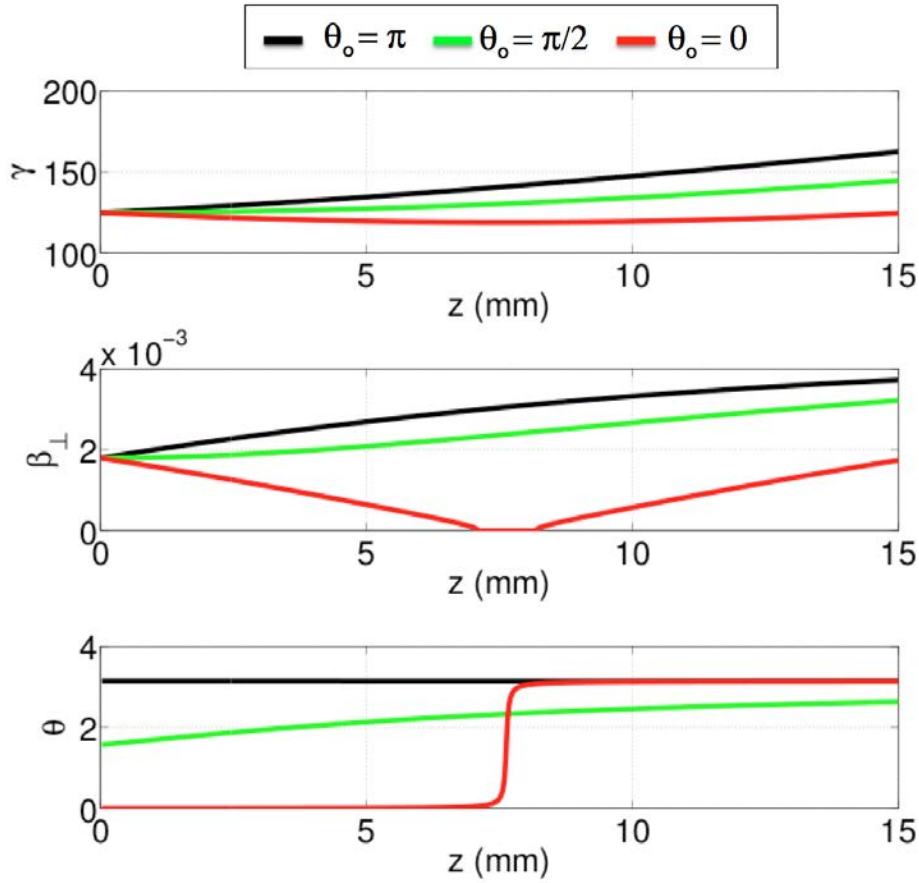


Figure 5.5: Simulation results for on-resonance but different initial θ_o for $\gamma_o = 125$, $B_u = 45$. The top graph shows energy versus distance traveled for the first 15mm. The middle graph shows β_\perp versus distance. The bottom graph shows the evolution of θ . The black curves show $\theta_o = \pi$. The green curves show $\theta_o = \pi/2$. Red curves show $\theta_o = 0$.

θ_o values. Again, this is a surprising and encouraging result. Initially, it was thought that electrons that did not have a favorable θ_o would not gain energy.

Let us again consider a similar analysis of initial θ_o but with an even lower initial electron energy of $\gamma_o = 120$ and $\alpha_{\text{res}} \approx 1\text{mrad}$. These results are shown in Fig. 5.6. With $\gamma_o = 120$ case, β_\perp starts out with an even smaller value than the previous two cases since the required injection angle is smaller. Therefore, β_\perp goes to zero sooner which causes θ_o to change quickly π sooner.

Let us again consider a similar analysis of initial θ_o but an initial electron energy of $\gamma_o = 119$

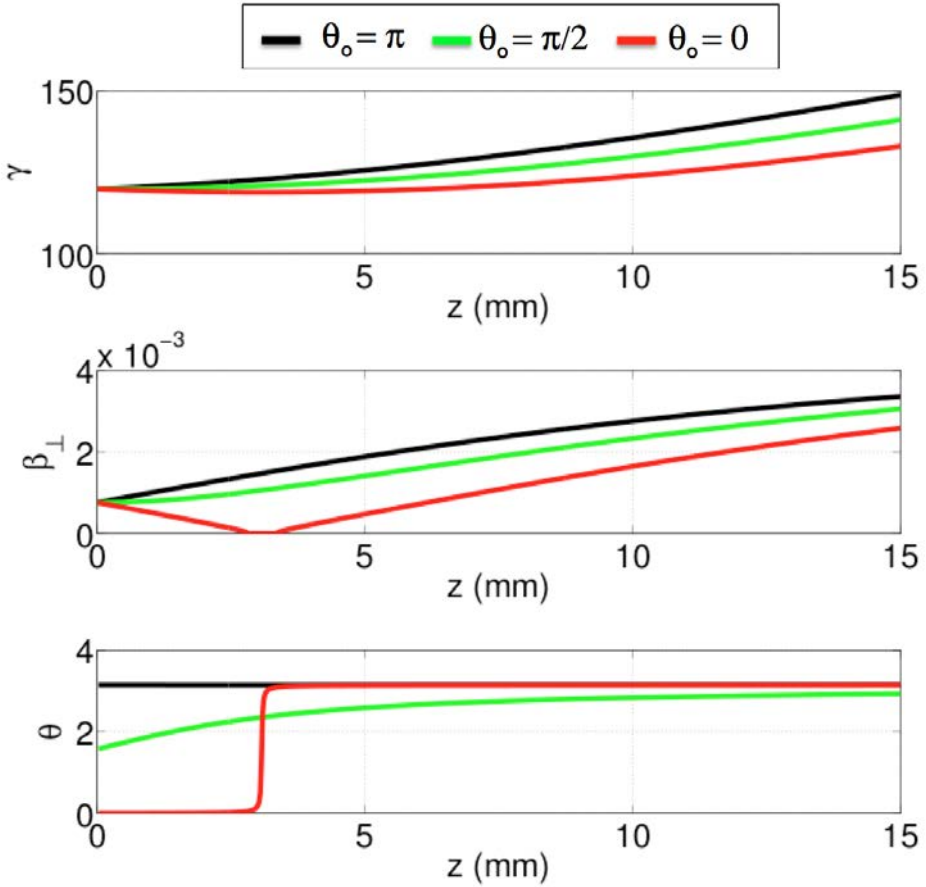


Figure 5.6: Simulation results for on-resonance but different initial θ_o for $\gamma_o = 120$, $B_u = 45$. The top graph shows energy versus distance traveled for the first 15mm. The middle graph shows β_\perp versus distance. The bottom graph shows the evolution of θ . The black curves show $\theta_o = \pi$. The green curves show $\theta_o = \pi/2$. Red curves show $\theta_o = 0$.

and $\alpha_{\text{res}} \approx 20 \mu\text{rad}$. These results are shown in Fig. 5.7. We are now quite familiar with the story. In the middle graphs, β_\perp starts with a much smaller value than the previous three initial energy cases. For the $\theta_o = 0$ case, β_\perp evolves to zero even sooner which quickly leads to $\theta = \pi$. This result encourages us to inject at the minimum energy possible where the resonance condition will remain satisfied, given in Eq. (3.81), if the desire is for all θ_o to be accelerated quickly.

Let us once more consider a similar analysis of different θ_o but with the lowest an initial electron energy that will satisfy the resonance condition. We have $\gamma_o = \gamma_{\min}$ and $\alpha_{\text{res}} = 0$

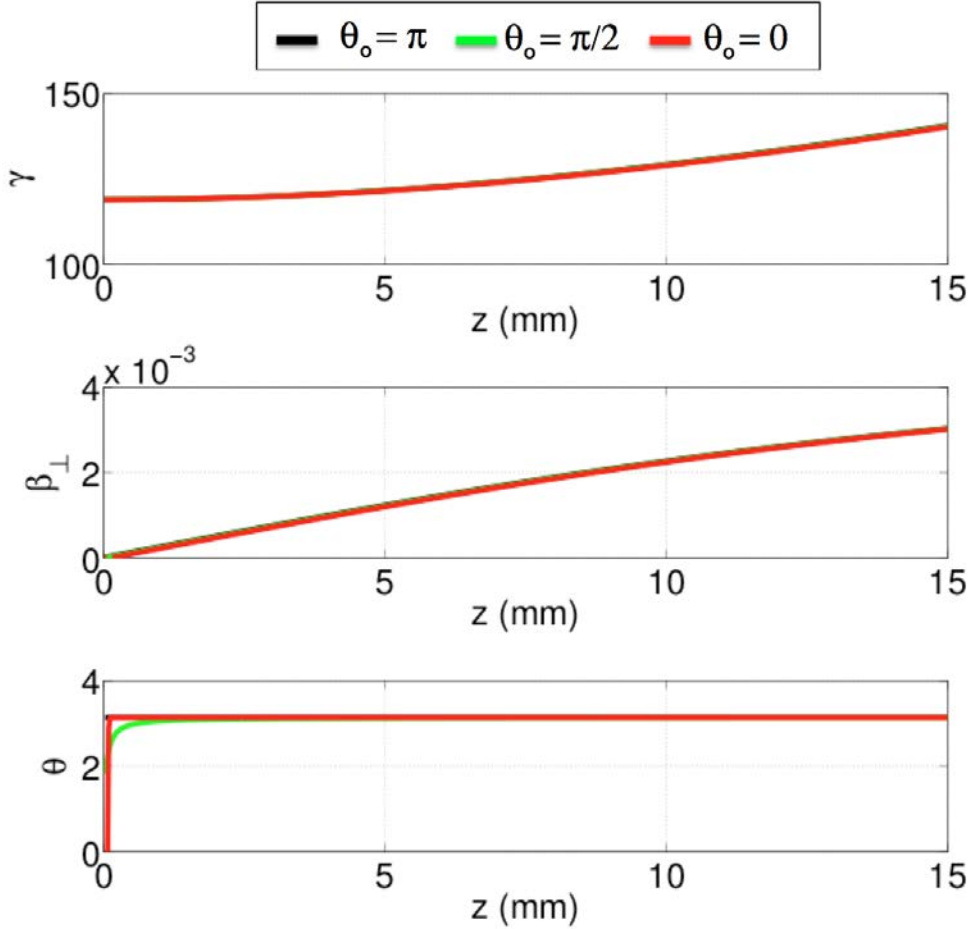


Figure 5.7: Simulation results for on-resonance but different initial θ_o for $\gamma_0 = 119$, $B_u = 45$. The top graph shows energy versus distance traveled for the first 15mm. The middle graph shows β_\perp versus distance. The bottom graph shows the evolution of θ . The black curves show $\theta_o = \pi$. The green curves show $\theta_o = \pi/2$. Red curves show $\theta_o = 0$.

rad. These results are shown in Fig. 5.8. Minimum energy injection results in $\beta_\perp = 0$. To prove this, substitute the analytic expression for minimum energy required for resonance, Eq. (3.81), into the expression for β_\perp in terms of γ and ε , Eq. (3.29). With $\beta_\perp = 0$, the vector $\boldsymbol{\beta}_\perp$ has no length. Therefore, θ is undefined. In fact, all electrons starting at the minimum energy, will have the same evolution for energy and β_\perp as shown in Fig. 5.8. The laser accelerator for energies close to the minimum required for resonance will accept all values of θ_o and resulting in energy gain.

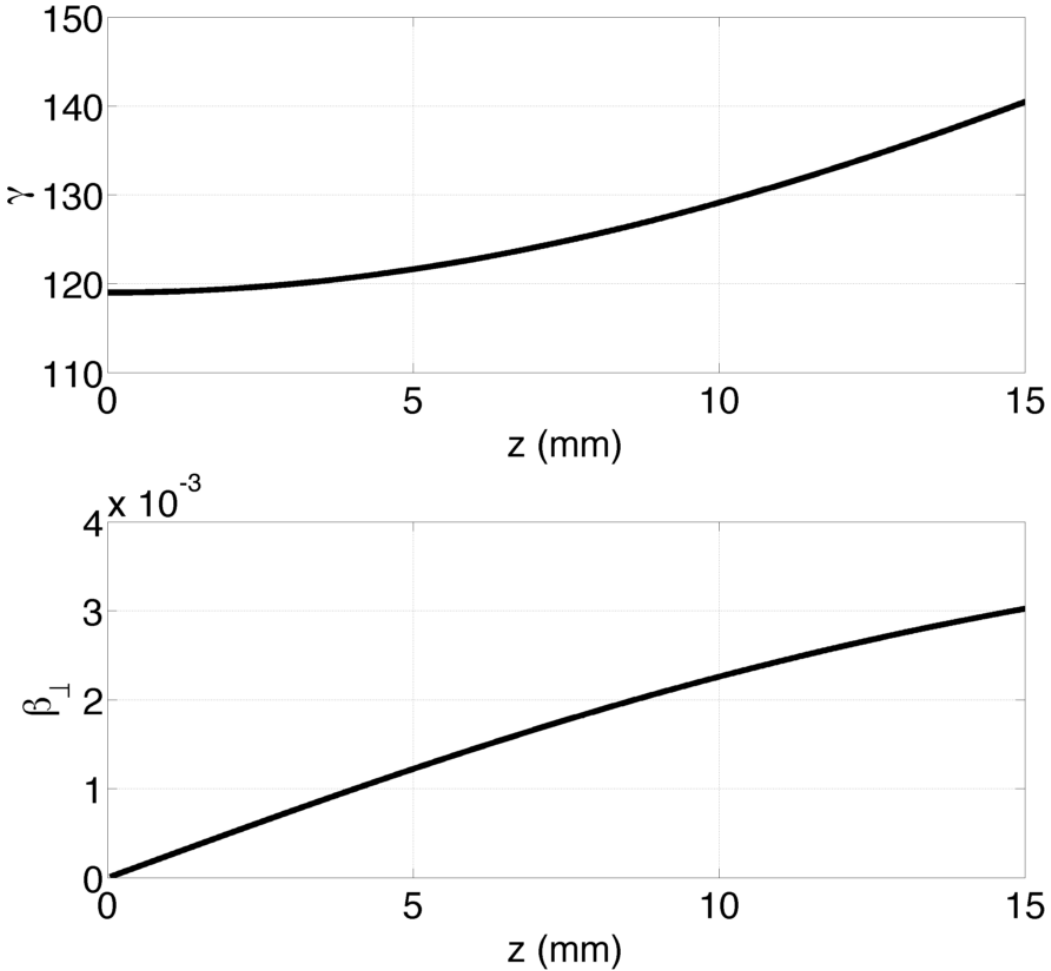


Figure 5.8: Simulation results for on-resonance with $\gamma_o = \gamma_{\min} \approx 118.99927$, $B_u = 45$. The top graph shows energy versus distance traveled for the first 15mm. The bottom graph shows β_{\perp} versus distance.

Let us now try to understand why this surprising result makes physical sense. Recall that this entire discussion has been on resonance or when $\Delta\omega = 0$. Recall Eq. (3.53) where $\eta = \gamma(\Delta\omega + \omega_E \beta_{\perp} \sin \theta)$. Since we know that β_{\perp} is zero at some point in the evolution for the $\theta_o = 0$ case, that pins the value of η to zero for all time since it is a constant of the motion. But later in the evolution, β_{\perp} and γ grow. The only way to ensure that η stays zero is for $\sin \theta$ to be zero or when $\theta = \pi$. The next line of reasoning eliminates the possibility that θ evolves to 0.

When β_{\perp} is zero, then β_x and β_y are also zero. Going back to the original equations of

motion, Eqs. (3.19) through (3.22), we now have

$$\frac{d\gamma}{dt} = 0 \quad (5.4)$$

$$\frac{d}{dt}(\gamma\beta_x) = -\frac{eE_o}{mc}(1-\beta_z)\cos\zeta \quad (5.5)$$

$$\frac{d}{dt}(\gamma\beta_y) = \frac{eE_o}{mc}(1-\beta_z)\sin\zeta \quad (5.6)$$

$$\frac{d}{dt}(\gamma\beta_z) = 0 \quad (5.7)$$

So the terms that deal with the magnetic field are completely turned off. They contribute nothing when the electrons move parallel to the field lines. Rewriting Eqs. (5.5) and (5.6) with the components of the electric field factored out we have

$$\frac{d}{dt}(\gamma\beta_x) = \frac{e\varepsilon}{\gamma mc}(-E_x) \quad (5.8)$$

$$\frac{d}{dt}(\gamma\beta_y) = \frac{e\varepsilon}{\gamma mc}(-E_y) \quad (5.9)$$

The right-hand side of Eqs. (5.8) and (5.9) are proportional to the force that the electron feels when it is moving in a direction that is opposite to the electric field or when $\theta = \pi$.

In this section we have considered the performance of the laser accelerator for only three θ_o cases. But we are encouraged that even with the most unfavorable initial θ_o , energy gain is possible if the initial energies are near the minimum required for resonance.

5.3 Off-resonance Performance

As already discussed, the electron bunch in an actual experiment is much longer than the optical wavelength and therefore spans over the entire θ_o range from 0 to 2π . Additionally, electrons will not be perfectly collimated and will consequently have a finite spread in injection angles α . This latter effect implies that the resonance condition, $\Delta\omega = 0$, will not be satisfied for all electrons in the bunch since for a given initial energy, magnetic field, and laser frequency, $\Delta\omega$ is a function of the injection angle α . Substituting Eqs. (3.24) and

(3.41) in (3.43) we have

$$\Delta\omega = \frac{eB_u}{m\gamma_0} - \omega_r \left(1 - \frac{1}{\gamma_0} \sqrt{\gamma_0^2 - 1} \cos \alpha \right). \quad (5.10)$$

The right-hand side of Eq. (5.10) equals zero when $\alpha = \alpha_{\text{res}}$ (which is calculated in Eq. (3.79)). We want to explore the behavior of the laser accelerator for off-resonance cases for a spread of α near α_{res} .

Let us begin with the case $\gamma_0 = 130$ with an external field $B_u = 45$ T. The results are shown in Fig. 5.9 where we have conducted many simulations of the laser accelerator over a meter long interaction and plotted the final energy values γ_f as a function of α and θ_o . Notice

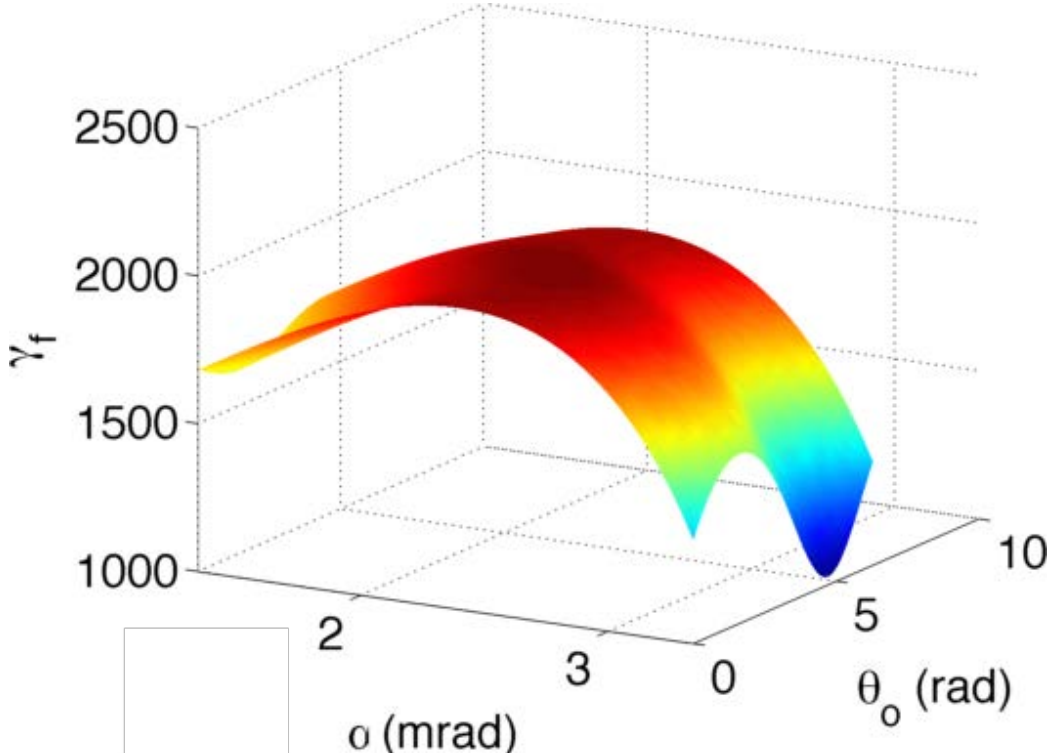


Figure 5.9: Surface graph of final electron energy γ_f versus initial θ_o and α for $\gamma_0 = 130$ and $B_u = 45$. There is a peak energy gain near $\alpha_{\text{res}} \approx 2.4$ mrad and $\theta_o = \pi$ as expected.

that there is a peak energy gain near $\alpha_{\text{res}} \approx 2.4$ mrad and $\theta_o = \pi$ as expected.

We can get a better perspective by considering the contour plot shown in Fig. 5.10. The results indicate that electrons with initial conditions inside the blue region achieve 99 per-

Maximum $\gamma_f = 2056$

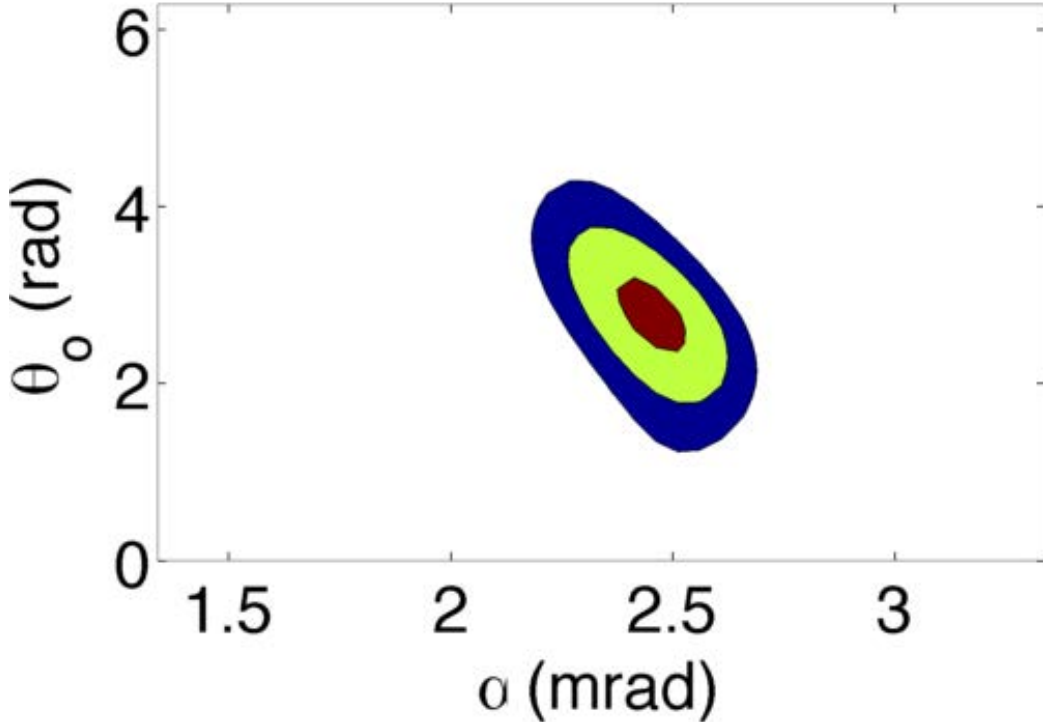


Figure 5.10: Contour graph of electron energy versus θ_o and injection angles α for $\gamma_0 = 130$ and $B_u = 45$. The peak occurs near $\alpha_{\text{res}} \approx 2.4$ mrad. Electrons with θ_o and α inside the blue region achieve 99 percent of maximum energy gain. Electrons with θ_o and α inside the green region achieve 99.1 percent of maximum energy gain. Electrons with θ_o and α inside the maroon region achieve 99.9 percent of maximum energy gain.

cent of maximum energy gain. Electrons with initial conditions inside the green region achieve 99.1 percent of maximum energy gain. Electrons with initial conditions inside the red region achieve 99.9 percent of maximum energy gain. These results give a sense of the energy spread of the laser accelerator output beam, depending on the alignment of the input beam from the electron injector and the spread in injection angles.

Let us consider a similar plot but now for the case of $\gamma_0 = 120$ with an external field of 45 T shown in Fig. 5.11. These results look similar to the previous contour plot but the parameter space area resulting in 99 percent energy gain has increased dramatically to include all initial θ_o values. From the discussion on phase from § 5.2, this makes sense.

Maximum $\gamma_f = 2044$

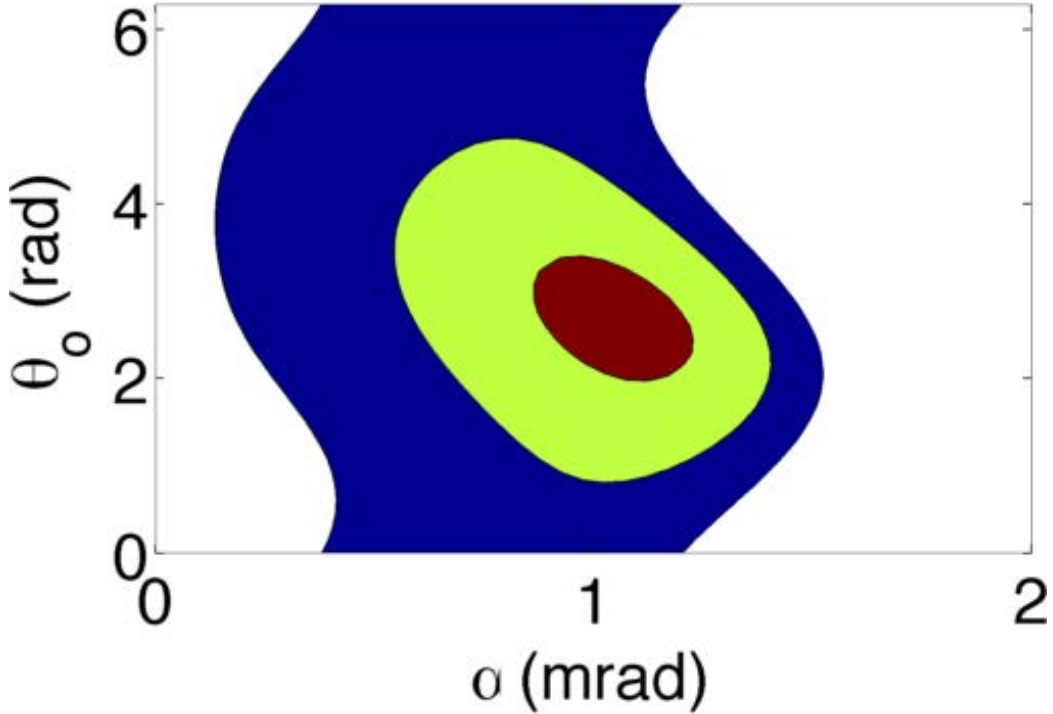


Figure 5.11: Contour graph of electron energy versus θ_o and injection angles α for $\gamma_o = 120$ and $B_u = 45$. The peak occurs near $\alpha_{\text{res}} \approx 1.8$ mrad. Electrons with θ_o and α inside the blue region achieve 99 percent of maximum energy gain. Electrons with θ_o and α inside the green region achieve 99.1 percent of maximum energy gain. Electrons with θ_o and α inside the maroon region achieve 99.9 percent of maximum energy gain.

Electrons with an unfavorable θ_o , lose β_\perp since β_\perp begins with a smaller value. After β_\perp goes to zero, The value of θ is no longer meaningful and can change to π for the reasons discussed previously. Now these electrons now are able to achieve energy gain.

Let us consider a similar plot but now for the case of $\gamma_o = 119$ with an external field of 45 T shown in Fig. 5.12. The parameter space area resulting in 99.1 percent energy gain has increased dramatically to include all initial θ_o . Notice that for Figs. 5.10, 5.11, and 5.12, we gained greater acceptance range in θ_o at the expense of the maximum energy γ_f since it went down from $\gamma_f = 2056$ to $\gamma_f = 2042$.

Maximum $\gamma_f = 2042$

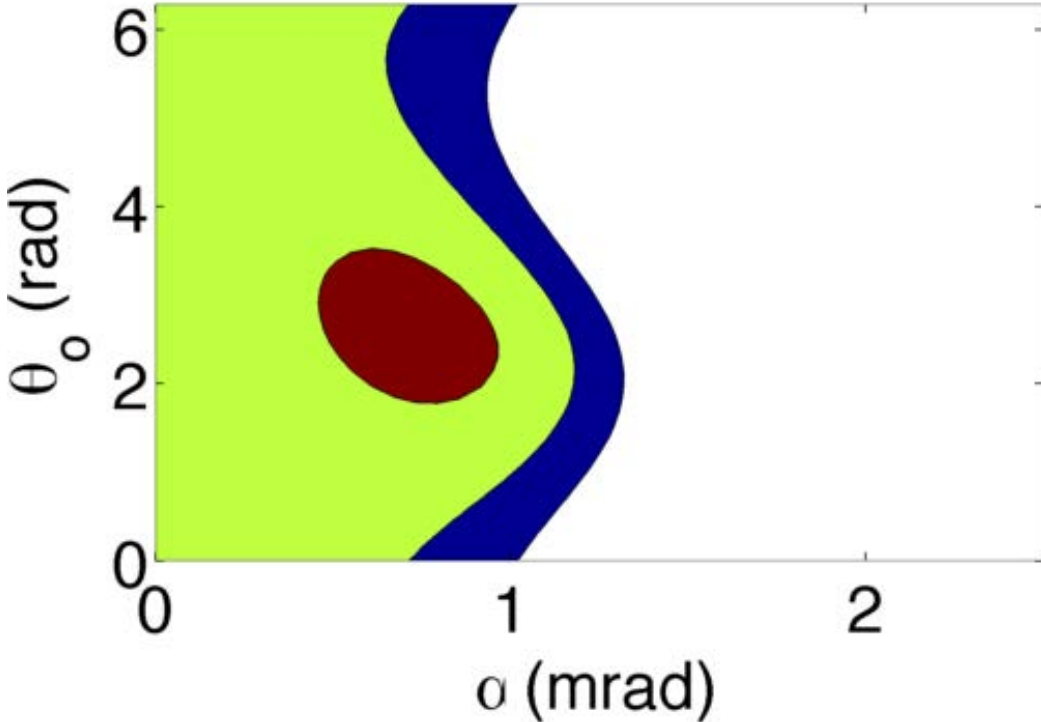


Figure 5.12: Contour graph of electron energy versus θ_o and injection angles α for $\gamma_o = 120$ and $B_u = 45$. The peak occurs near $\alpha_{\text{res}} \approx 20 \mu\text{rad}$. Electrons with θ_o and α inside the blue region achieve 99 percent of maximum energy gain. Electrons with θ_o and α inside the green region achieve 99.1 percent of maximum energy gain. Electrons with θ_o and α inside the maroon region achieve 99.9 percent of maximum energy gain.

Encouraged by the previous contour plots and the results of § 5.2, it seems that starting with a smaller β_\perp ensures more electrons receive similar accelerations and energy gains. So let us just start with a beam entering on-axis where $\alpha = \beta_\perp = 0$. Now $\Delta\omega$ is only a function of two independent variables, γ_o and B_u . We have for on-axis injection

$$\Delta\omega_{\text{OA}} = \frac{eB_u}{m\gamma_o} - \omega_r \left(1 - \frac{1}{\gamma_o} \sqrt{\gamma_o^2 - 1} \right). \quad (5.11)$$

By varying γ_o and B_u we expect the maximum energy to be in a band that follows the $\Delta\omega = 0$ contour seen in Fig. 5.13.

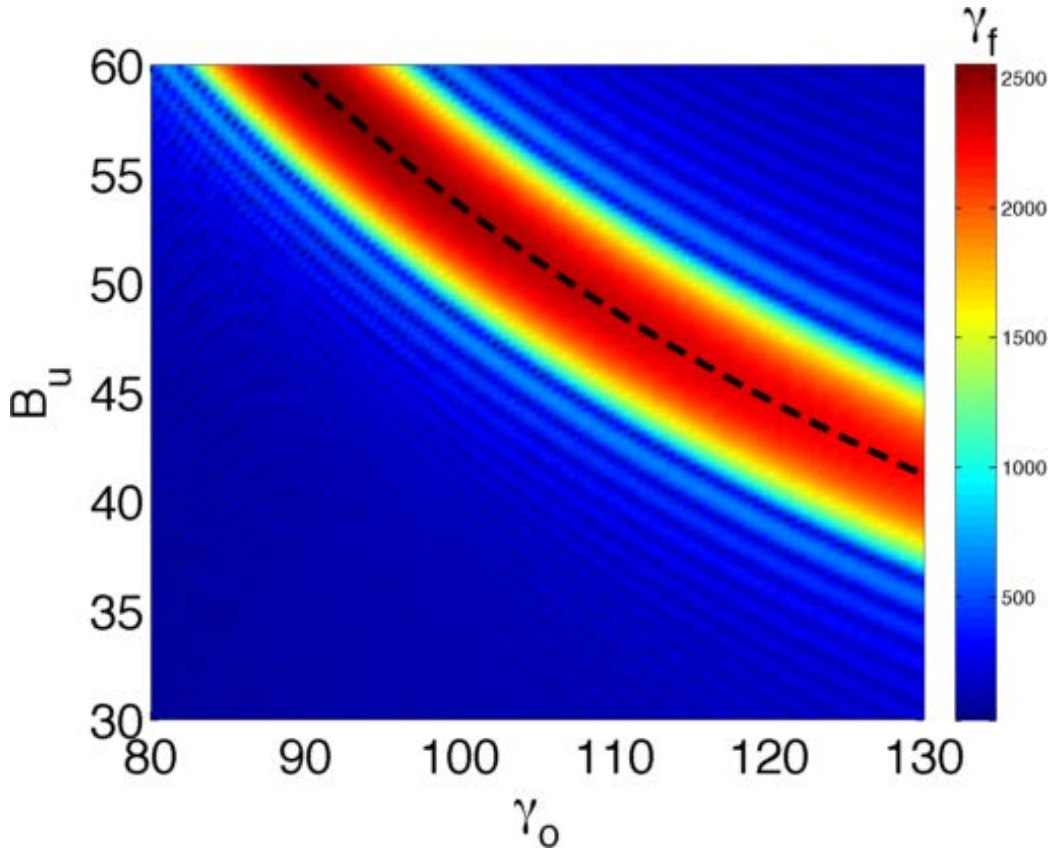


Figure 5.13: Simulation results showing an intensity plot of final electron energies with initial conditions that explore a range of external magnetic fields from $B_u = 30$ T to 60 T and $\gamma_0 = 80$ to 130. The dotted line indicates the $\Delta\omega_{OA} = 0$ contour.

In Fig. 5.13, we have an intensity plot that depicts the final electron energies of electrons with varying initial γ_0 and external magnetic field values but with on-axis injection where $\alpha = \beta_\perp = 0$. Therefore the angle between β_\perp and \mathbf{E}_r has no meaning. The optical force on the electron from the electric field acts on the electron such that θ quickly evolves to a value of π as discussed at the end of § 5.2. The electrons then proceed to gain energy. The resonance $\Delta\omega = 0$ level curve is overlaid on the intensity plot and shown as a black-dotted curve. Notice how the electrons with good energy gain follows that contour curve as expected. There exists a width about the contour line $\Delta\omega = 0$ for whereby the laser accelerator performs well with $\gamma_f \approx 2500$. This corresponds to electron energy gain of 1.2 GeV in one meter. Once the right combination of parameters for resonance are identified, the laser accelerator is quite forgiving in its acceptance margins in initial energy and external

magnetic field strength for on-axis injection.

We can now make an estimate on normalized emittance values that the laser accelerator would accept from an electron injector. Normalized emittance is given by

$$\epsilon_n = \gamma \langle r \rangle \langle \alpha \rangle \quad (5.12)$$

Let us consider an initial electron energy of $\gamma = 130$, $\langle r \rangle = 0.5$ mm since the optical waist is about 1 mm, and $\langle \alpha \rangle = 0.5$ mrad. The spread in injection angles α is a conservative estimate based on the simulations presented. We then have $\epsilon_n = 32.5$ mm-mrad, which is quite large. Electron injectors with good emittance values are about 10 mm-mrad.

5.4 Magnetic Field Effects

The external magnetic field source for the laser accelerator might be constructed of resistive or superconducting solenoids such as those at NHMFL. The magnetic field on the axis for a solenoid can be written as [25]:

$$B_z \propto B_u (\cos \theta_1 + \cos \theta_2) \quad (5.13)$$

where θ_1 and θ_2 are defined in Fig. (5.15).

For example, if we assume the maximum field $B_u^{\max} = 45$ T at $z_w = 0.5$ m, then by Eq. (5.13) the field profile is given by Fig. (5.14) assuming a bore diameter of 32 mm.

By including Eq. (5.13) in the simulation we have the following results shown in Fig. 5.16. Notice the results indicate a final energy of 1.15 GeV versus 1.2 GeV for a the static case. The top left graph plots electron energy gained versus distance traveled. The bottom left graph plots β_{\perp} versus distance traveled. The bottom right graph plots $1 - \beta_z$ versus distance traveled. The only major difference with Fig. 5.2 is that the electron's radial position flared out in the last few millimeters. Comparing this with Fig. 5.15, the magnetic field strength drops to nearly half its maximum value. Therefore, the electron spirals out more.

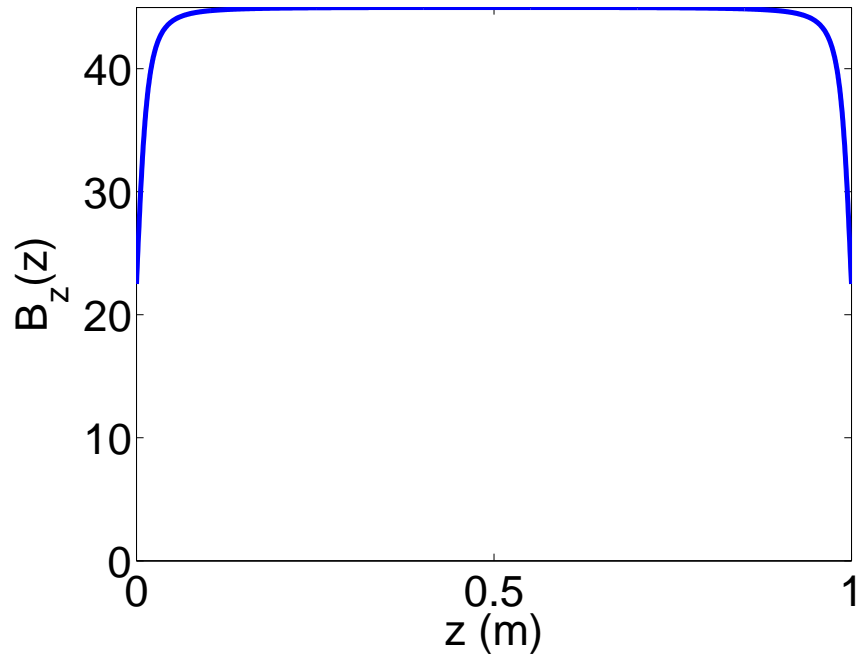


Figure 5.14: Magnetic field variation along z with maximum field at $z_w = 0.5$ m [25]

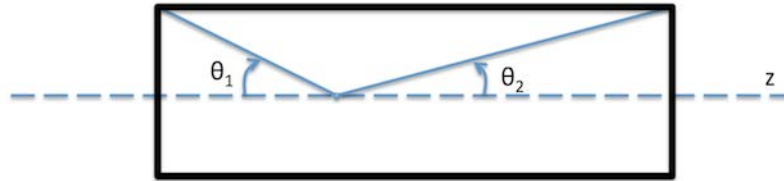


Figure 5.15: Diagram defines θ_1 and θ_2 for calculating the magnetic field along the longitudinal axis of a solenoid represented by the box.

5.5 Diffraction Effects

The numerical solutions presented in the previous sections have assumed plane-wave description for the laser source. In real lasers, the optical beam wavefronts are spherical with the fundamental mode taking on a Gaussian irradiance pattern transverse to the optical axis . fields for the electric field of the laser where the wavefronts ar. Real lasers have a Gaussian approximation to the laser However, let us consider the effects of Gaussian mode. Begin-

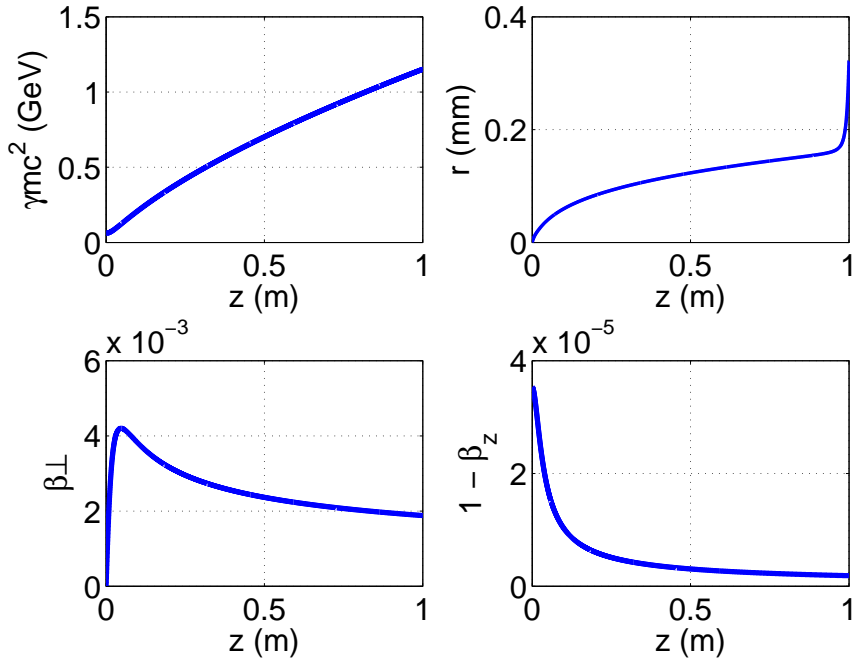


Figure 5.16: Real magnetic field effects included in simulation for $\gamma_o = 119$. The top left graph plots electron energy gained versus distance traveled. The top right graph plots the radial position of the electron from optical axis. The bottom left graph plots β_{\perp} versus distance traveled. The bottom right graph plots $1 - \beta_z$ versus distance traveled.

ning with a circularly-polarized Gaussian laser field in the fundamental mode, we have the following electric and magnetic field components:

$$\begin{aligned} \mathbf{E}_r &= E_o \frac{w_o}{w(z)} e^{-r^2/w^2(z)} e^{i(\phi+\zeta)} \begin{bmatrix} 1 \\ i \end{bmatrix}, \\ \mathbf{B}_r &= \frac{E_o}{c} \frac{w_o}{w(z)} e^{-r^2/w^2(z)} e^{i(\phi+\zeta)} \begin{bmatrix} -i \\ 1 \end{bmatrix} \end{aligned} \quad (5.14)$$

with

$$\phi_G = \frac{k_r r^2}{2R} - \tan^{-1} \left(\frac{z - z_w}{Z_r} \right) \quad (5.15)$$

$$w = w_o \sqrt{1 + \frac{(z - z_w)^2}{Z_r^2}} \quad (5.16)$$

$$Z_r = \frac{\pi w_o^2}{\lambda} \quad (5.17)$$

$$R = \frac{1}{z - z_w} [(z - z_w)^2 + Z_r^2] \quad (5.18)$$

where $\zeta = k_r z - \omega_r t$, ϕ_G is the Gaussian phase contribution, w is the beam radius radius, w_o is the beam waist, Z_r is the Rayleigh length, R is the phase front radius of curvature, and z_w is the position of the laser beam waist.

Substituting Eqs. (5.14) into (3.4) then substituting the real part into Eq. (3.3) yields the following:

$$\frac{d\gamma}{dt} = -\frac{eE_o}{mc} \frac{w_o}{w} e^{-r^2/w^2} [\beta_x \cos(\phi_G + \zeta) - \beta_y \sin(\phi_G + \zeta)] \quad (5.19)$$

$$\frac{d}{dt}(\gamma\beta_x) = -\frac{eE_o}{mc} \frac{w_o}{w} e^{-r^2/w^2} \cos(\phi_G + \zeta)(1 - \beta_z) - \frac{eB_u}{m} \beta_y \quad (5.20)$$

$$\frac{d}{dt}(\gamma\beta_y) = \frac{eE_o}{mc} \frac{w_o}{w} e^{-r^2/w^2} \sin(\phi_G + \zeta)(1 - \beta_z) + \frac{eB_u}{m} \beta_x \quad (5.21)$$

$$\frac{d}{dt}(\gamma\beta_z) = -\frac{eE_o}{mc} \frac{w_o}{w} e^{-r^2/w^2} [\beta_x \cos(\phi_G + \zeta) - \beta_y \sin(\phi_G + \zeta)] \quad (5.22)$$

Eqs. (5.19) through (5.22) are similar to Eqs. (3.19) through (3.22) in the previous section but they are now modified to include Gaussian beam effects in the amplitude and phase terms. To first order, let us assume the following: the electron's trajectory is well inside the optical mode and the Rayleigh length, Z_r , is two meters long (twice the interaction region distance). With these assumptions, the amplitude factor, $w_o e^{-r^2/w^2}/w$, does not significantly change since the electron radius is well inside the optical mode. The Guoy phase shift, ϕ_G , is

$$\phi_G = -\tan^{-1} \left(\frac{z - z_w}{Z_r} \right). \quad (5.23)$$

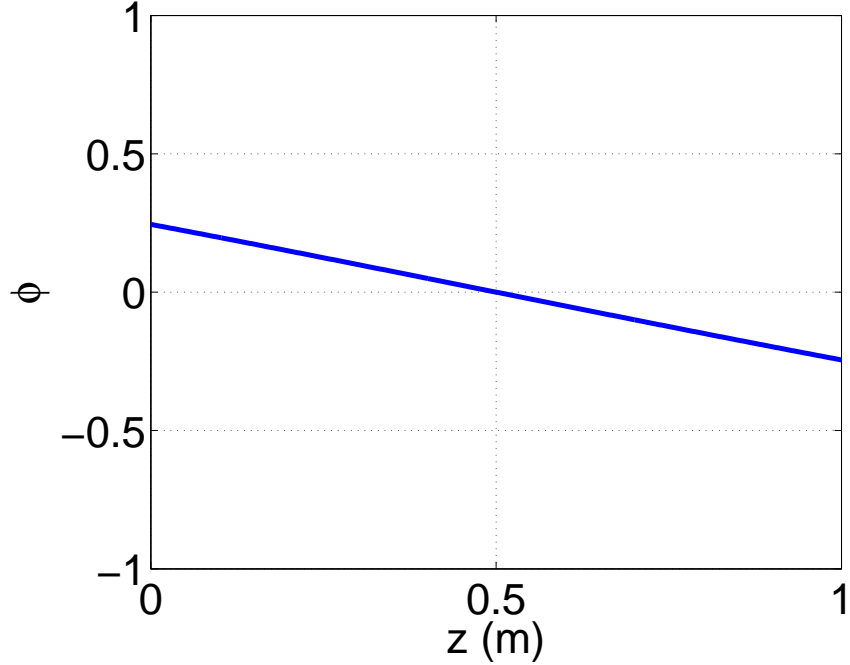


Figure 5.17: Guoy phase shift over the interaction region with $z_w = 0.5$.

and plotted in Fig. (5.17). As we expect, to first order, the $d\phi_G/dz \approx -1/Z_r$ about the waist.

Once again we can define the constant of the motion, $\varepsilon = \gamma(1 - \beta_z)$, based on Eqs. (5.19) and (5.22) by noting that the right-hand sides are identical. Now we must consider how ϕ_G affects the other constant of the motion, η .

Note the following:

$$\frac{d}{dt} \cos(\phi_G + \zeta) = -\sin(\phi_G + \zeta) \frac{d\phi_G}{dt} + \omega_r(1 - \beta_z) \sin(\phi_G + \zeta) \quad (5.24)$$

$$\frac{d}{dt} \sin(\phi_G + \zeta) = \cos(\phi_G + \zeta) \frac{d\phi_G}{dt} - \omega_r(1 - \beta_z) \cos(\phi_G + \zeta) \quad (5.25)$$

$$\sin(\phi_G + \zeta) \frac{d}{dt} (\gamma \beta_x) = \frac{d}{dt} (\gamma \beta_x \sin(\phi_G + \zeta)) - \gamma \beta_x \cos(\phi_G + \zeta) \frac{d\phi_G}{dt} + \gamma \beta_x \omega_r(1 - \beta_z) \cos(\phi_G + \zeta) \quad (5.26)$$

$$\cos(\phi_G + \zeta) \frac{d}{dt} (\gamma \beta_y) = \frac{d}{dt} (\gamma \beta_y \cos(\phi_G + \zeta)) + \gamma \beta_y \sin(\phi_G + \zeta) \frac{d\phi_G}{dt} - \gamma \beta_y \omega_r(1 - \beta_z) \sin(\phi_G + \zeta) \quad (5.27)$$

Solving for β_x and β_y in Eqs. (5.20) and (5.21) and substituting in Eq. (5.19) we have

$$\frac{d\gamma}{dt} = \frac{m}{e} \frac{1}{B_u} \gamma \omega_r (1 - \beta_z) \frac{d\gamma}{dt} - \gamma \frac{d\phi_G}{dt} \frac{m}{eB_u} \frac{d\gamma}{dt} - \frac{E_o}{cB_u} \frac{d}{dt} (\gamma \beta_y \cos(\phi_G + \zeta)) - \frac{E_o}{cB_u} \frac{d}{dt} (\gamma \beta_x \sin(\phi_G + \zeta)). \quad (5.28)$$

To first order, $d\phi_G/dt = (d\phi_G/dz) (dz/dt) \approx -c/Z_r$. Substituting this into Eq. (5.28) and extracting an overall time derivative we arrive at

$$\gamma \left[\frac{eB_u}{\gamma_0 m} - \omega_r (1 - \beta_{zo}) + \frac{eE_o}{\gamma_0 mc} (\beta_x \sin(\phi_G + \zeta) + \beta_y \cos(\phi_G + \zeta)) - \frac{c}{2Z_r} \frac{\gamma}{\gamma_0} \right] = \text{constant} \quad (5.29)$$

and as before $\Delta\omega = eB_u/\gamma_0 m - \omega_r (1 - \beta_{zo})$, $\gamma_0 = \gamma(0)$, $\epsilon = \gamma_0 (1 - \beta_{zo})$, and $\omega_E = eE_o/\gamma_0 mc$. Comparing Eq. (5.29) to Eq. (3.44) we see that the Gaussian beam description has added ϕ_G in the trigonometric functions and a new term, $-c\gamma/2Z_r\gamma_0$. The magnitude of this first order correction is on the order of 10^9 s^{-1} . This is approximately two-orders of magnitude smaller than other terms. The conclusion is that, to first order, a Gaussian beam will have similar solutions to the plane-wave solutions calculated in the previous sections.

THIS PAGE INTENTIONALLY LEFT BLANK

CHAPTER 6: Conclusions

The relativistic Lorentz force law for the laser accelerator has been solved numerically using Euler-Cromer integration methods for the first time. Simulation results indicate that electron energy can grow from about 60 MeV to over 1.2 GeV in one meter using today's high powered lasers and magnetic fields. The electron's perpendicular velocity is a key parameter in achieving good energy gain. For the first time, the complete evolution of the electron's perpendicular velocity over the interaction region is shown. The resonance condition was reexamined and a minimum energy requirement was determined for the first time. Laser accelerator performance was examined when at $\Delta\omega \neq 0$ and was determined to be more tolerant of off-resonance injection than previously thought.

The initial electron phase, or the angle between β_\perp and \mathbf{E}_r , was examined and surprisingly found to be tolerant of unfavorable initial phase orientation. If operating near the minimum energy and at resonance, it was found that there is significant energy gain for all initial electron phases. Electrons that were once thought to not gain energy due to unfavorable initial phase orientations may still contribute to a high energy beam if the initial energy is near the minimum energy. Therefore, a large parameter space in phase and injection angles exists for the laser accelerator.

Diffraction, magnetic field solenoid edge, and Guoy phase evolution effects were examined and differences from ideal plane wave results are provided. Magnetic field edge effects were examined and determined to not adversely affect electron energy gain.

A survey of existing high powered laser sources, magnetic field systems, and injectors was conducted to give a sense of what a university sized laser accelerator would have to be.

THIS PAGE INTENTIONALLY LEFT BLANK

APPENDIX: Simulation Codes

There were many individual programs that were created in C or Matlab for a specific task such as calculating resonance angle for a given magnetic field, laser wavelength, and initial electron injection energy. In this appendix a sample of the laser accelerator engine code is included for reference. The numerical integration was programmed in C with graphics exported for use in Matlab.

A.1 Laser Accelerator Simulation Core

```
//  
// main.c  
// LASim7  
//  
// Created by Ricardo Vigil on 3/4/14.  
// Copyright (c) 2014 Ricardo Vigil. All rights reserved.  
//  
  
#include <stdio.h>  
#include <stdlib.h>  
#include <math.h>  
#include <time.h>  
  
#define pi 3.1415926535897932  
  
//double pi=3.141592653589793238;  
  
double c = 2.99792458E8; // speed of light (m/s)  
double uo = 12.566370614E-7; // Permeability of vacuum (N A^-2)  
double eo = 8.854187817E-12; // permittivity constant (F/m)  
double q = 1.602176565E-19; // absolute value of electron  
charge (C)  
double m = 9.10938291E-31; // mass of electron (kg)
```

```

double mc2_ev = 0.510998928E6;           // electron rest mass (eV)
double Zr = 2.0;                         // Rayleigh length (m)
double lambda_r = 1E-6;                  // laser wavelength (m) Vulcan
laser
double k;                                // wave number (m^-1)
double P = 1E15;                          // laser peak power (W) source
is 10^15
double Ipk = 1.0E25;                     // peak intensity W m^-2 at
Vulcan Laser
double delta_z = 1E-5;                   // propagation length step
size (m)
double L = 1.0;                          // length of interest (m)
double wo;                               // laser beam waist radius in
m for
double xo = 0.0;                        // initial electron position
double yo = 0.0;                        // initial electron position
double dt = 7E-14;                      // time step
double tiempo;                         // time for light to travel
double Bu = 45.0;                       // External B field
double width;                           // pipe width (m)
double wr;
double epsilon;
double dw;
double gamma_min, gamma_o, ggamma;
double alpha;
double A, Eo, beta_o, we, bzo, bpo, wco, g_m, bpmax, rot_angle,
g_star;
double zeta, bp, bz, bx, by, bz, x, y, z, g_check_bp,
g_check_bxby;
double ax, ay, az, dx, dy, dz, t, r, a,b,p1,p2,bxo, byo;
double bxold, byold, bzold, LP;
double phi_e, phi_l, bx1, by1, Ex, Ey, brk, Bu, r_approx,

```

```

alpha_o, phi, eta;
double gamma_top, gamma_bot, dgamma, alpha_top, alpha_bot,
dalpha, epsilon_res,
alpha_res, kappa;
double p0, px, py, pz, ggammaload, Eng, eta, bp_bxby, bp_epsilon;
double p0old, pxold, pyold, pzold;
double ctheta, stheta, stheta2, brk, brk2;
double dI[1000001];
double delta_g, g, intG, epsilon_f;
double frac_a, frac_b, frac_ep, frac_eta;
double ao, bo, epsilon_o, eta_o, dwo;
double Ex, Ey;
double Eangle, bpangle;
double etap, etam;
double theta;
double etaprime, temp, wtf;
double b1, b2;
double ggammal, zI, test;
double aa, bb, cc, zz;
double zo;
double frac_dw, dw_anal, dw_te, alpha2, gp, gm;
double denom, denom_ul, denom_ul_explicit;
double factor1, factor2, factor12, denomFactor;
double factor3, factor3eta;
double factor4;
double expandedFactor3;
double expandedDenom;
double expandedDenom_dwwe;
double aa_u, bb_u, cc_u;
double d, f;
double dwwe_zero, dwwe_1, dwwe_2, LHS, RHS;
double delta, rho;

```

```

double deltaomega;
double z_anal;

int i,j;
int nalpha=150;
int ngamma=111;
int nt;
int count=1000001;

int flag = 4;    // case 1. resonance & consts
                  // case 2. resonance & no consts
                  // case 3. no resonance & consts
                  // case 4. no resonace & no consts
                  // case 5. explict use of cos(theta)

int main(void)
{
    clock_t begin, end;
    double time_spent;
    begin = clock();

    FILE *out10, *out11;
    FILE *out30, *out31;

```

```

//-----
// Initialize arrays
//-----
for(i=0;i<1000001;i++) dI[i] = 0.0;

//-----
// Calculate Global constants
//-----
nt = round(L/(c*dt)) + 1;
// number of time steps
width = 32.0 / 1000;
// width of pipe.
wo = sqrt(Zr*lambda_r/pi);
// mode radius at waist
A=pi*wo*wo;
// area of laser beam (m^2) at waist
Eo = sqrt( (P)/(c*eo*A));
// Electric Field (V/m)
wr = (2*pi*c/lambda_r);
// laser field angular freq
k = (2*pi)/lambda_r;
// laser wave number
deltaomega = 0.0;
printf("wr\t\t\t = %.16e\n",wr);
printf("deltaomega\t = %.16e\n",deltaomega);
wr = wr + deltaomega/2.0;
printf("wr (new)\t = %.16e\n",wr);

//-----

```

```

// Initial Conditions (Global)
//-----
printf("Eo = %.16e\n", Eo);

x = 0.0;
y = 0.0;
z = 0.0;
z_anal = 0.0;
r = x*x + y*y;
r_approx = 0.0;
t = 0.0;
LP = 0.0;
rot_angle = 0.0;
zeta = k*z - wr*t;

switch (flag) {

    case 4:
    {
        printf("case 4.\n\n");
        printf("wo\t\t = %.16e\n", wo);

        FILE *out40, *out41, *out42, *out43, *out44;

        Bu = 45.0;
        out40 = fopen("/Users/vigilr/Dropbox/FEL/
LASim7/lasim7_case4_Io.txt", "w");
        out41 = fopen("/Users/vigilr/Dropbox/FEL/
LASim7/lasim7_case4.out", "w");
        out42 = fopen("/Users/vigilr/Dropbox/FEL/
LASim7/lasim7_case4_int.out", "w");
        out43 = fopen("/Users/vigilr/Dropbox/FEL/

```

```

LAsim7/lasim7_case4_test.out", "w");
        out44 = fopen("/Users/vigilr/Dropbox/FEL/
LAsim7/lasim7_case4_fracDW.out", "w");

//-----
// Initial Conditions (specific to Case 4)
// No constraints on gamma_o, alpha,
and phi for a fixed Bu.
//-----

ggamma = 150.0;
ggammaold = ggamma;
gamma_o = ggamma;
phi = pi; //3.1292756331662902e-01;
alpha_res = acos((gamma_o - ((q*Bu) / (wr*m)) ) /
(sqrt(gamma_o*gamma_o - 1)) );
alpha = alpha_res;

bz = 1.0/gamma*sqrt(gamma*ggamma - 1.0)*cos(alpha);
printf("bzo\t\t= %.16e\n", bz);

bp = 1.0/gamma*sqrt(gamma*ggamma - 1.0)*sin(alpha);
printf("bpo\t\t= %.16e\n", bp);
bx = bp*cos(phi);                                // eq 4
by = bp*sin(phi);                                // eq 5

beta_o = 1.0/gamma*sqrt(gamma*ggamma - 1.0);
if (fabs(bp) < 1E-15) bp=0.0;

```

```

    if (fabs(bx) < 1E-15) bx=0.0;
    if (fabs(by) < 1E-15) by=0.0;
    zo = atan(bx/by)/k;

    epsilon = ggamma*(1-bz); // eq 6

    bp_bxby = sqrt(bx*bx + by*by);
    bp_epsilon = (1/gamma) *
sqrt(2*ggamma*epsilon - epsilon*epsilon - 1);
    bpo = bp_epsilon;
    bxold = bx;
    byold = by;
    bzold = bz;
    p0 = gamma*m*c; // eq 10
    px = gamma*m*c*bx; // eq 7
    py = gamma*m*c*by; // eq 8
    pz = gamma*m*c*bz; // eq 9
    p0old = p0;
    pxold = px;
    pyold = py;
    pzold = pz;
    g_check_bxby = 1/sqrt(1 - bx*bx - by*by - bz*bz);
    ax = c*bx/dt;
    ay = c*by/dt;
    az = c*bz/dt;
    dx = c*by*az - ay*c*bz;
    dy = ax*c*bz - c*bx*az;
    dz = c*bx*ay - ax*c*by;
    zeta = 0.0;//k*z - wr*t; //
    Ex = cos(zeta);
    Ey = -1.0*sin(zeta);
    fprintf(out43,"%16e\n", (pxold*cos(zeta) - pyold * sin(zeta))

```

```

//-----
//      initial angles
//-----

if (Ex > 0 && Ey > 0 ) Eangle = atan(Ey/Ex);
if (Ex < 0 && Ey > 0 ) Eangle = atan(Ey/Ex) + pi;
if (Ex < 0 && Ey < 0 ) Eangle = atan(Ey/Ex) + pi;
if (Ex > 0 && Ey < 0 ) Eangle = atan(Ey/Ex) + 2.0*pi;

if (bx > 0 && by > 0 ) bpangle = atan(by/bx);
if (bx < 0 && by > 0 ) bpangle = atan(by/bx) + pi;
if (bx < 0 && by < 0 ) bpangle = atan(by/bx) + pi;
if (bx > 0 && by < 0 ) bpangle = atan(by/bx) + 2.0*pi;

theta = Eangle - bpangle;
if (theta < 0 ) theta = theta + 2.0*pi;
if (theta > 0 && theta > pi) theta = 2.0*pi - theta;

if (phi>0 && phi<pi) theta = phi;

//-----
// Calculate derived paramaters
//-----

test = bx*cos(k*z-wr*t+k*zo) - by*sin(k*z-wr*t+k*zo);
we = (q*Eo)/(gamma_o*m*c);
wco = (q*Bu)/(m*ggamma);
g_star = (epsilon*epsilon+1)/epsilon;
gamma_min = (epsilon*epsilon+1)/(2*epsilon);
bpmax = (epsilon/sqrt(epsilon*epsilon+1))
dw = wco +
(wr/gamma)*sqrt(gamma*gamma - 1)*cos(alpha) - wr;           // eq 23

```

```

dw_anal = (q*Bu) / (ggamma*m) +
wr*bz - wr;
      a = ggamma*bx - ((q*Eo) / (m*c*wr)) *sin(zeta)
+ ((q*Bu) / (m*c)) *y;
      b = ggamma*by - ((q*Eo) / (m*c*wr)) *cos(zeta)
- ((q*Bu) / (m*c)) *x;
      temp = (bx*sin(zeta) + by*cos(zeta));
      eta = ggamma*dw + ggamma*we*(bx*sin(zeta)
+ by*cos(zeta)); // eq 24
      etap = ggamma*dw +
ggamma*we*bp_epsilon*sin(theta);
      etam = ggamma*dw -
ggamma*we*bp_epsilon*sin(theta);
      wtf = asin((wr - wco - wr*beta_o*cos(alpha))
/ (we*beta_o*sin(alpha)));
      stheta = (eta - ggamma*dw) /
(we*sqrt(2*ggamma*epsilon - epsilon*epsilon - 1));
      stheta2 = (bx*sin(zeta) + by*cos(zeta))/bp_bxby;
      ctheta = (bx*cos(zeta) - by*sin(zeta))/bp_epsilon;
      brk = bx*cos(zeta) - by*sin(zeta); // bp * cos(theta);
      brk2 = bx*sin(zeta) + by*cos(zeta); // bp * sin(theta);
      frac_a = 0.0;
      frac_b = 0.0;
      frac_ep = 0.0;
      frac_eta = 0.0;
      ao = a;
      bo = b;
      epsilon_o = epsilon;
      eta_o = eta;

//-----
// Inputs

```



```

//----
px = pxold + ((-q*Eo)*(epsilon/gammaold)*cos(zeta)
- (q*Bu*pyold)/(gammaold*m))*dt; // eq 15
bx = px/(gamma*m*c);
x = x + bx*c*dt;
//----
py = pyold + ((q*Eo)*(epsilon/gammaold)*sin(zeta)
+ (q*Bu*pxold)/(gammaold*m))*dt; // eq 18
by = py/(gamma*m*c);
y = y + by*c*dt;
//----
pxold = px;
pyold = py;
gammaold = gamma;
//----
t = t + dt;
zeta = k*z - wr*t;
//----
bp_bxby = sqrt(bx*bx + by*by);
bp_epsilon = (1/gamma)*sqrt(2*gamma*epsilon
- epsilon*epsilon-1);
if ((2*gamma*epsilon - epsilon*epsilon-1) < 0 ) {
    bp_epsilon = 0.0;
}

//----
stheta = (eta_o - gamma*dw) /
(we*sqrt(2*gamma*epsilon - epsilon*epsilon - 1));;
stheta2 = (bx*sin(zeta) + by*cos(zeta))/bp_bxby;
ctheta = (bx*cos(zeta) - by*sin(zeta))/bp_epsilon;
brk = bx*cos(zeta) - by*sin(zeta); //
```

```

brk2 = bx*sin(zeta) + by*cos(zeta);
epsilon_f = ggamma*(1-bz);

//-----
//      Angles
//-----

Ex = cos(zeta);
Ey = -sin(zeta);

if (Ex > 0 && Ey > 0 ) Eangle = atan(Ey/Ex);
if (Ex < 0 && Ey > 0 ) Eangle = atan(Ey/Ex) + pi;
if (Ex < 0 && Ey < 0 ) Eangle = atan(Ey/Ex) + pi;
if (Ex > 0 && Ey < 0 ) Eangle = atan(Ey/Ex) + 2.0*pi;

if (bx > 0 && by > 0 ) bpangle = atan(by/bx);
if (bx < 0 && by > 0 ) bpangle = atan(by/bx) + pi;
if (bx < 0 && by < 0 ) bpangle = atan(by/bx) + pi;
if (bx > 0 && by < 0 ) bpangle = atan(by/bx) + 2.0*pi;

theta = Eangle - bpangle;
if (theta < 0 ) theta = theta + 2.0*pi;
if (theta > 0 && theta > pi) theta = 2.0*pi - theta;

b1 = bp_epsilon*cos(theta);
b2 = bp_epsilon*sin(theta);

//---
a = ggamma*bx - ((q*Eo) / (m*c*wr))*sin(zeta)
+ ((q*Bu) / (m*c))*y;

```

```

      b = ggamma*by - ((q*Eo) / (m*c*wr)) *cos(zeta)
      - ((q*Bu) / (m*c)) *x;
      eta = ggamma*(dw + ((q*Eo) / (gamma_o*m*c)) *
      (bx*sin(zeta) + by*cos(zeta)));
      etap = ggamma*(dw + ((q*Eo) / (gamma_o*m*c)) *
      bp_epsilon*sin(theta));
      etam = ggamma*(dw - ((q*Eo) / (gamma_o*m*c)) *
      bp_epsilon*sin(theta));
      etaprime = ggamma + ggamma*(Eo/c*Bu)*
      (bx*sin(zeta) + by*cos(zeta)) - (m*epsilon*wr*ggamma) / (q*Bu);

      frac_a = (a - ao)/ao;
      frac_b = (b - bo)/bo;
      frac_eta = (eta - eta_o)/eta_o;
      frac_ep = (epsilon_f - epsilon)/epsilon;
      //---
      r = sqrt(x*x + y*y);
      r_approx = (m*ggamma*sqrt(bx*bx+by*by)*c) / (q*Bu);
      //---
      ax = c*(bx - bxold)/dt;
      ay = c*(by - byold)/dt;
      az = c*(bz - bzold)/dt;
      bxold = bx;
      byold = by;
      bzold = bz;
      dx = c*by*az - ay*c*bz;
      dy = ax*c*bz - c*bx*az;
      dz = c*bx*ay - ax*c*by;
      LP = ((uo*q*q*ggamma*ggamma*ggamma*ggamma*ggamma*
      ggamma*ggamma) / (6*pi*c)) *
      (ax*ax + ay*ay + az*az -
      (1/(c*c))*(dx*dx + dy*dy + dz*dz));

```

```

//----
rot_angle = rot_angle + (q*Bu) / (m*ggamma)*dt;
//----
g_check_bxby = 1/sqrt(1 - bx*bx - by*by - bz*bz);
//-----
dw_anal = (q*Bu) / (ggamma*m) - wr*(1-bz);
//-----
z_anal = (c/gamma_o) *
(1/(3*we*we*we*we*epsilon*epsilon)) *
sqrt(2*we*we*epsilon*ggamma -
we*we*epsilon*epsilon - we*we - eta*eta) *
(we*we*epsilon*ggamma -
we*we*epsilon*epsilon + we*we +
eta*eta - 3*we*we*epsilon*epsilon);

//-----
// Matlab output
//-----


fprintf(out41, "%.16e\t%.16e\t%.16e\t%.16e\t
%.16e\t%.16e\t%.16e\t%.16e\t
%.16e\t%.16e\t%.16e\t%.16e\t
%.16e\t%.16e\t%.16e\t%.16e\t
%.16e\t%.16e\t%.16e\t%.16e\t
%.16e\t%.16e\t%.16e\t%.16e\t
%.16e\t%.16e\t%.16e\t%.16e\t
%.16e\t%.16e\n",
t,x,y,z,r,r_approx,ggamma,

```

```

bx,by,bz,bp_bxby,
bp_epsilon,g_check_bxby,Lp,
zeta,sttheta,ctheta,brk,epsilon_f,
a,b,eta,frac_a,frac_b,frac_ep,frac_eta,
brk2,sttheta2,theta,etap,etam,etaprime,dw_anal,z_anal);
}

//-----
// Outputs
//-----

epsilon_f = ggamma*(1-bz);
a = ggamma*bx -
((q*Eo)/(m*c*wr))*sin(zeta) + ((q*Bu)/(m*c))*y;
b = ggamma*by -
((q*Eo)/(m*c*wr))*cos(zeta) - ((q*Bu)/(m*c))*x;
eta = ggamma*(dw +
((q*Eo)/(ggamma*m*c))*(bx*sin(zeta) + by*cos(zeta)));

```



```

fprintf(out40, "\n\t---Calculated Values---\n");
fprintf(out40, "?_max\t=
%.16e\n?pmax\t= %.16e\n", g_m,bpmax);
fprintf(out40,
"\n\t---Outputs---\n");
fprintf(out40, "?_F\t= %.16e\n
Eng_F\t= %.16e\n?z\t= %.16e\n
?p\t= %.16e\nRev\t= %.16e\n
r_F\t= %.16e\nnr_apprx\t= %.16e\n
L\t= %.16e\nTime\t= %.16e\n",
ggamma,mc2_ev*ggamma/1E9,bz,

```

```

        bp, rot_angle/(2*pi), r, r_approx, z, t);
        printf("?
_star\t= %.16e\n?
_min\t=%.16e\n
_o\t\t= %.16e\n?
_F\t\t= %.16e\n
Eng_F\t= %.16e\n?\t\t= %.16e\n
?\t\t= %.16e\nBu\t\t= %.16e\n
?\t\t= %.16e\nna\t\t= %.16e\n
b\t\t= %.16e\n?\t\t= %.16e\n
we\t\t= %.16e\nwc\t\t= %.16e\n
wr\t\t= %.16e\n?\t\t= %.16e\n
Revs\t= %g\nnnt\t\t= %d\nnz\t\t= %.16e\n",
g_star, gamma_min, gamma_o,
ggamma, mc2_ev*ggamma/1E9, alpha,
phi, Bu, epsilon, a, b, eta_o,
we, wco, wr, dw, rot_angle/(2*pi), nt, z);
        fclose(out40);
        fclose(out41);
        fclose(out42);
        fclose(out43);
        fclose(out44);
        break;

    }

default:
    printf("try again\n");
} // end switch

//-----
end = clock();
time_spent = (double)(end - begin) / CLOCKS_PER_SEC;
printf("\n\nElapsed: %.16g seconds\n", time_spent);

return 0;

```

}

A.2 Laser Accelerator Matlab Graphics Script

```
clear
close all
clc

load lasim7_case4.out;
load lasim7_case4_int.out;
load lasim7_case4_10m.out;

c = 2.99792458E8;           % speed of light (m/s)
uo = 12.566370614E-7;       % Permeability of vacuum (N A^-2)
eo = 8.854187817E-12;       % permittivity constant (F/m)
q = 1.602176565E-19;        % absolute value of electron charge (C)
m = 9.10938291E-31;         % mass of electron (kg)
mc2_ev = 0.510998928E6;     % electron rest mass (eV)
Eo = 4.3401054911612872e+11;
we = (q*Eo) / (119.0*m*c);    % 1/s

%z10 = lasim7_case4_10m(:,4);
%ggamma10 = lasim7_case4_10m(:,7);

t = lasim7_case4(:,1);
x = lasim7_case4(:,2);
y = lasim7_case4(:,3);
z = lasim7_case4(:,4);
r = lasim7_case4(:,5);
r_a= lasim7_case4(:,6);
```

```

ggamma = lasim7_case4(:,7);
bx = lasim7_case4(:,8);
by = lasim7_case4(:,9);
bz = lasim7_case4(:,10);
bp_bxby = lasim7_case4(:,11);
bp_epsilon = lasim7_case4(:,12);
g_check_bxby = lasim7_case4(:,13);
LP = lasim7_case4(:,14);
zeta = lasim7_case4(:,15);
stheta = lasim7_case4(:,16);
ctheta = lasim7_case4(:,17);
brk = lasim7_case4(:,18);
epsilon = lasim7_case4(:,19);
a = lasim7_case4(:,20);
b = lasim7_case4(:,21);
eta = lasim7_case4(:,22);
frac_a = lasim7_case4(:,23);
frac_b = lasim7_case4(:,24);
frac_ep = lasim7_case4(:,25);
frac_eta = lasim7_case4(:,26);
brk2 = lasim7_case4(:,27);
stheta2 = lasim7_case4(:,28);
theta = lasim7_case4(:,29);
etap = lasim7_case4(:,30);
etam = lasim7_case4(:,31);
etaprime = lasim7_case4(:,32);
dw_anal = lasim7_case4(:,33);
z_anal = lasim7_case4(:,34);

D = z_anal - (z_anal(2)-z_anal(1));

```

```

zI = lasim7_case4_int(:,1);
gI = lasim7_case4_int(:,2);

ao = a(1);
bo = b(1);

frac_a = (a - ao)/ao;
frac_b = (b - bo)/bo;

figure(1)
subplot(3,2,1)
set(gca,'FontSize',24)
plot(z,ggamma*mc2_ev/1E9,'LineWidth',3)
%hold on
%plot(z,g_check_bxby*mc2_ev/1E9,'r','LineWidth',2)
xlabel('z','FontSize',24)
ylabel('\gammamc^2 (GeV)')
xlim([0 max(z)])
grid
legend('gamma','gamma check')

subplot(3,2,2)
%plot(z,r,'LineWidth',3)
set(gca,'FontSize',24)
%hold on
plot(z,r_a,'r','LineWidth',2)
xlabel('z (m)')
ylabel('r (m)')
grid
xlim([0 max(z)])

```

```

legend('r','r approx')

subplot(3,2,3)
set(gca,'FontSize',24)
plot(z,bp_epsilon,'LineWidth',3)
%hold on
%plot(z,bp_bxby,'r','LineWidth',2)
%hold on
%plot(z,brk,'g')
xlabel('z')
ylabel('\beta\perp')
xlim([0 max(z)])
grid

subplot(3,2,4)
set(gca,'FontSize',24)
plot(z,1-bz,'LineWidth',3)
xlabel('z')
ylabel('1 - \beta_z')
grid
xlim([0 max(z)])
subplot(3,2,5:6)
plot(z,sttheta,'LineWidth',3)
hold on
plot(z,ctheta,'r','LineWidth',3)
set(gca,'FontSize',24)
xlabel('z')
ylabel('sin/cos')
xlim([0 1])
legend('sin(theta)', 'cos(theta)', 'brk')
title('does \theta = \theta_o')

```

```
figure(2)
set(gca,'FontSize',24)
plot3(x,y,z)
xlabel('x')
ylabel('y')
zlabel('z')
grid
```

```
figure(3)
subplot(2,2,1)
plot(z,frac_ep)
set(gca,'FontSize',24)
xlabel('z (m)')
ylabel('frac ep')
xlim([0 max(z)])
subplot(2,2,2)
plot(z,frac_a)
set(gca,'FontSize',24)
xlabel('z (m)')
ylabel('frac_a')
xlim([0 max(z)])
subplot(2,2,3)
plot(z,frac_b)
set(gca,'FontSize',24)
xlabel('z (m)')
ylabel('frac_b')
xlim([0 max(z)])
subplot(2,2,4)
plot(z,frac_eta)
set(gca,'FontSize',24)
```

```

xlabel('z (m)')
ylabel('frac eta')
xlim([0 max(z)])

figure(4)
plot(z,brk,z,brk2)
legend('brk','brk2')
xlim([0 max(z)])

figure(5)
plot(z,stheta,z,stheta2)
legend('stheta1','stheta2')
xlim([0 max(z)])

figure(6)
plot(z,theta)
xlim([0 0.1])
ylim([0 2*pi])

figure(7)
plot(z,eta,z,etap,z,etam)
legend('eta','etap','etam')
xlim([0 max(z)])

figure(8)
plot(z,ggamma,'LineWidth',3)
set(gca,'FontSize',26)
set(gcf,'color','w');
xlim([0 max(z)])
xlabel('z (m)')
ylabel('\gamma')
grid

```

```

figure(9)
set(gcf,'color','w');
set(gca,'FontSize',32);
plot(z_anal,ggamma*mc2_ev/1E9,'k','LineWidth',5)
hold on
plot(z,ggamma*mc2_ev/1E9,'--r','LineWidth',2)
hold on
%plot(z10,ggamma10*mc2_ev/1E9,'g','LineWidth',3)
xlabel('z (m)')
ylabel('\gamma mc^2 (GeV)')
legend('Analytic','Simulation')
xlim([0 max(z)])
ylim([min(gamma)*mc2_ev/1E9*0.7 1.1*max(gamma)*mc2_ev/1E9])
grid

```

List of References

- [1] W. Colson and S. Ride, “A laser accelerator,” *Applied Physics*, vol. 20, no. 1, pp. 61–65, 1979.
- [2] M. Martinez *et al.*, “The Texas Petawatt Laser,” in *Boulder Damage Symposium XXXVII: Annual Symposium on Optical Materials for High Power Lasers*. International Society for Optics and Photonics, 2005, pp. 59 911N–59 911N.
- [3] A. Siegman, *Lasers*. Sausalito, CA: University Science Books, 1986.
- [4] P. Bryant, “A brief history and review of accelerators,” *CERN European Organization for Nuclear Research*, vol. 1, pp. 1–1, 1994.
- [5] W. Panofsky, “The evolution of particle accelerators and colliders,” *SLAC Beam Line*, March 1997.
- [6] A. Chao and M. Tigner, *Handbook of Accelerator Physics and Engineering*. Hackensack, NJ: World Scientific Publishing Co., 1999.
- [7] K. Wille, *The Physics of Particle Accelerators: An Introduction*. Oxford: Oxford University Press, 2000.
- [8] D. Kerst, “Acceleration of electrons by magnetic induction,” *Physical Review*, vol. 58, pp. 841–841, Nov. 1940.
- [9] C. Joshi and T. Katsouleas, “Plasma accelerators at the energy frontier and on tabletops,” *Physics Today*, vol. 56, no. 6, pp. 47–53, 2003.
- [10] T. Ditmire *et al.*, “Conceptual design report for the Texas Petawatt Laser at the Texas Center for High Intensity Laser Science,” *Texas Center for High Intensity Laser Science Proceedings*, March 2004.
- [11] Texas petawatt laser. (2014, January). [Online]. Available: <http://texaspeta.watt.ph.utexas.edu>
- [12] T. Ditmire *et al.*, “Overview of future directions in high energy-density and high-field science using ultra-intense lasers,” *Radiation Physics and Chemistry*, vol. 70, no. 4, pp. 535–552, 2004.
- [13] R. Paschotta. (2014). Optical parametric amplifiers. [Online]. Available: http://www.rp-photonics.com/optical_parametric_amplifiers.html

- [14] A. Dubietis *et al.*, “Trends in chirped pulse optical parametric amplification,” *IEEE Journal of Selected Topics in Quantum Electronics*, vol. 12, no. 2, pp. 163–172, 2006.
- [15] T. Rao and D. H. Dowell, “An engineering guide to photoinjectors,” *arXiv preprint arXiv:1403.7539*, March 2014.
- [16] Y. Cheng *et al.*, “Electron field emission from carbon nanotubes,” *Comptes Rendus Physique*, vol. 4, no. 9, pp. 1021–1033, 2003.
- [17] K. Shepard *et al.*, “Superconducting triple-spoke cavity for $\beta=0.5$ ions,” *Proceedings of the Particle Accelerator Conference*, pp. 4344–4346, 2005.
- [18] Meet the magnets. (2014, January). [Online]. Available: <http://www.magnet.fsu.edu/mediacenter/features/meetthemagnets/index.html>
- [19] J. Singleton *et al.*, “The National High Magnetic Field Laboratory pulsed-field facility At Los Alamos National Laboratory,” *Physica B: Condensed Matter*, vol. 346, pp. 614–617, 2004.
- [20] B. Brandt *et al.*, “The national high magnetic field laboratory,” *Physica B: Condensed Matter*, vol. 294–295, no. 0, pp. 505 – 511, 2001.
- [21] J. Crow *et al.*, “The United States National High Magnetic Field Laboratory: Facilities, science and technology,” *Physica B: Condensed Matter*, vol. 216, no. 3, pp. 146–152, 1996.
- [22] J. Miller, “The NHMFL 45-T hybrid magnet system: past, present, and future,” *IEEE Transactions on Applied Superconductivity*, vol. 13, no. 2, pp. 1385–1390, 2003.
- [23] J. R. Sims *et al.*, “Assembly, commissioning and operation of the nhmfl 100 tesla multi-pulse magnet system,” *IEEE Transactions on Applied Superconductivity*, vol. 18, no. 2, pp. 587–591, 2008.
- [24] P. Ehrenfest, “Bemerkung über die angenäherte gültigkeit der klassischen mechanik innerhalb der quantenmechanik,” *Zeitschrift für Physik*, vol. 45, no. 7-8, pp. 455–457, 1927.
- [25] J. D. Jackson, *Classical Electrodynamics*, 3rd ed. New York: John Wiley and Sons, Inc., 1999.
- [26] E. Weisstein. (2014, July). Cycloids. From MathWorld—A Wolfram Web Resource. [Online]. Available: <http://mathworld.wolfram.com/Cycloid.html>

- [27] D. Halliday, R. Resnick, and J. Walker, *Fundamentals of Physics Extended*. Hoboken, NJ: John Wiley & Sons, 2010.
- [28] A. Cromer, “Stable solutions using the euler approximation,” *American Journal of Physics*, vol. 49, no. 5, pp. 455–459, 1981.
- [29] D. J. Griffiths, *Introduction to Electrodynamics*, 3rd ed. Upper Saddle River, NJ: Prentice Hall, 1999.

THIS PAGE INTENTIONALLY LEFT BLANK

Initial Distribution List

1. Defense Technical Information Center
Ft. Belvoir, Virginia
2. Dudley Knox Library
Naval Postgraduate School
Monterey, California